UNIVERSITY OF OKLAHOMA

GRADUATE COLLEGE

THE USE OF EEG-FMRI FEATURES FOR CHARACTERIZING MENTAL DISORDERS

A DISSERTATION

SUBMITTED TO THE GRADUATE FACULTY

in partial fulfillment of the requirements for the

Degree of

DOCTOR OF PHILOSOPHY

By

OBADA AL ZOUBI
Norman, Oklahoma
2019

Downloaded from SHAREOK. Persistent Handle URL: https://hdl.handle.net/11244/321134

THE USE OF EEG-FMRI FEATURES FOR CHARACTERIZING MENTAL DISORDERS

A DISSERTATION APPROVED FOR THE
SCHOOL OF ELECTRICAL AND COMPUTER ENGINEERING

BY

_____
Dr. Hazem Refai, Chair

_____
Dr. Jerzy Bodurka, Co-chair

_____
Dr. Thordur Runolfsson

_____
Dr. James Sluss

_____
Dr. Samuel Cheng

_____
Dr. Justin Feinstein

_____
Dr. Curt Adams

© Copyright by OBADA AL ZOUBI 2019
All Rights Reserved.

This is dedicated to my parents for their enormous support. Without them, this work would have never seen the light. Dad implanted in me the love of science and always encouraged me to pursue the highest degree. Mom put every effort I could have imagined into supporting my studies.

To all who have supported knowledge and empowered science.

Acknowledgments

Life brings all sort of challenges and struggles, but it is livable because of the support from many around us. If you are reading this work, this is because of many people who have believed in me. Most likely, I will miss someone in the acknowledgments, so at the beginning, I would like to thank everyone who has contributed to my work. Second, I would like to express my gratitude and deepest respect to Dr. Hazem Refai and Dr. Jerzy Bodurka for their enormous help, support, immense knowledge, and mentorship. Dr. Jerzy Bodurka has created for me an invaluable research space to develop myself and learn brain imaging. Dr. Hazem Refai helped me to pave my way and offered unconditional advice, support, and generosity through my Ph.D. I would also like to extend my deepest gratitude to Dr. Justin Feinstein for his training, guidance, generosity, tremendous encouragement, and his friendship, which I have enjoyed.

My gratitude must also go to my committee members for their comments, feedback, and guidance through this journey: Dr. James Sluss, Dr. Thordur Runolfsson, Dr. Samuel Cheng and Dr. Curt Adams.

Any achievement is a product of teamwork. I am grateful to Dr. Jerzy Bodurka's lab members whom I have had the pleasure to work with and from whom I have gained so much experience: Dr. Vadim Zotev, Dr. Masaya Misaki, Dr. Qingfei Luo, Dr. Aki Tsuchiyagaito, and Jared Smith. I would like to thank especially Ahmad Mayeli for his wonderful friendship and being such a support during my work.

To my institution and my other home—Laureate Institute for Brain Research, including all PIs and staff for offering funds, support, and training opportunities. Without the generous access to the advanced and high-quality Simultaneous EEG-fMRI dataset and facility, this work would have never seen the light. I would like especially to thank Dr. Martin Paulus for his guidance and support; Dr. Sahib Khalsa for the warm encouragement, advice, and kindness; Dr. Rayus Kuplicki for the unconditional help with many projects; and Dr. Jennifer Stewart for his enormous help and beautiful comments.

To all OU-Tulsa family and members for being such beautiful people working at an amazing place.

Having a supportive family flooded me with so much passion and love. I would like to express my deepest appreciation to my siblings: Kinda, Johainna, Arwa, and Moaz for their emotional and moral support.

I must acknowledge the person who has uplifted my life, filled my heart with so much love, and made every single moment possible: Iman Mousselli.

I'm grateful to have many good friends in my life, and I would like to thank all of them for their continuous support during my life.

Finally, I would like to thank agencies that funded my work: William K. Warren Foundation, National Institute of General Medical Sciences, National Institutes of Health, and U.S. Department of Defense.

Contents

Acknowledgments ..... **iv**

Contents ..... **vi**

List of Figures ..... **x**

List of Tables ..... **xviii**

Abstract ..... **xix**

Chapter 1 : Primer on EEG–fMRI Analysis **1**

1.1 Introduction *1*
1.2 fMRI Signal and Measurement *2*
1.3 EEG Signal and Recording *5*
1.4 Combining EEG-fMRI *6*
1.5 Methods of Integrating EEG-fMRI Data *7*
1.5.1 Asymmetrical EEG-fMRI Integration 8
1.5.2 Multimodal Fusion 11
1.6 EEG and fMRI for Discovery of Mental Disorders Biomarkers *12*
1.7 Dataset of Simultaneous EEG-fMRI Recording *13*
1.8 Data Acquisition of Simultaneous EEG-fMRI *14*
1.9 Summary of Contributions *14*
1.10 Dissertation Outline *15*

Chapter 2 : EEG Microstates: Theory, Principles, and Analyses **18**

2.1 Introduction *18*
2.2 EEG-ms Modeling *21*
2.3 Generalization from Subject Level to Group Level *24*
2.4 EEG-ms Characteristics *26*
2.5 Extracting EEG-ms in Practice *26*

Chapter 3 : Evidence of Altered EEG Microstates' Temporal Dynamics in Individuals with Mood and Anxiety Disorders **28**

3.1 Introduction *28*
3.2 Methods *30*
3.2.1 Participants 30
3.2.2 EEG Data Acquisition 30

3.2.3 EEG Data Preprocessing 30
3.2.4 Summary of EEG-ms Analysis Summary 32
3.2.5 Information Theoretical Analysis 33
3.3 Results *34*
3.4 Discussion *43*
3.5 Limitations *49*
3.6 Conclusions *49*

Chapter 4 : Predicting Age from EEG Using Unbiased Machine Learning Framework 51

4.1 Introduction *51*
4.2 Methods *56*
4.2.1 Participants 56
4.2.2 EEG Data Acquisition 56
4.2.3 EEG Data Preprocessing 56
4.2.4 EEG Feature Extraction 57
4.2.5 General Configuration 58
4.2.6 Feature Reduction 63
4.2.7 Machine Learning Methods 64
4.3 Results *68*
4.4 Discussion *74*
4.4.1 Age-related changes are affecting brain EEG signals 74
4.4.2 Can age be predicted from EEG signals? 75
4.2.3 Comparison with other works 76
4.5 Limitations *78*
4.6 Conclusions *78*

Chapter 5 : BrainAGE Prediction Using Simultaneous EEG-fMRI Features 80

5.1 Introduction *80*
5.2 Defining Regions of Interest from fMRI BOLD Signal *81*
5.3 Methods *82*
5.3.1 Participants 82
5.3.2 EEG-fMRI Data Aqusition 83
5.3.3 EEG Data Preprocessing 83
5.3.4 fMRI Data Preprocessing 83
5.3.5 Features of Interest 85
5.3.6 Features Preprocessing 86
5.3.7 Machine Learning Methods 86
5.4 Results *87*
5.5 Discussion *91*
5.6 Limitations *92*

5.7 Conclusions *92*

Chapter 6 : Studying Brain Based Biomarkers of Mood and Anxiety Disorders: An EEG-ms Informed fMRI Analysis **94**

6.1 Introduction *94*
6.2 EEG-ms inform fMRI *96*
6.3 Methods *97*
6.3.1 Participants 97
6.3.2 EEG-fMRI Data Acquisition 98
6.3.3 EEG Data Preprocessing 98
6.3.4 fMRI Data Preprocessing 98
6.3.5 Multimodal Analysis 98
6.4 Results *106*
6.4.1 Correlation Analysis between EEG-ms Brain Regions Functional Connectivity and Clinical Assessment Measures 118
6.5 Discussion *121*
6.6 Limitations *122*
6.7 Conclusions *123*

Chapter 7 : Proposal of a New Approach to Analyze EEG Microstates Data **124**

7.1 Introduction *124*
7.2 Methods *125*
7.2.1 Participants 125
7.2.2 EEG Data Acquisition 125
7.2.3 EEG Data Preprocessing 125
7.3 GFP Peaks and Labeling EEG *126*
7.4 Noise Effects on EEG-ms Templates Similarity and Sensitivity *128*
7.5 Towards Reproducible EEG-ms Results *134*
7.6 Limitations *136*
7.7 Conclusion *136*

Chapter 8 : Conclusions and Future Work **137**

8.1 Future work *138*

Appendix A **141**

INSTRUMENTS FOR CLINICAL SYMPTOMS ASSESSMENTS 141
GENERALIZED LINEAR MODEL ANALYSIS 142
SUPPLEMENTAL TABLES 142

Appendix B **147**

Glossary of Terms **153**

References..... 155

List of Figures

Figure 1-1: The basics of measuring the BOLD signal. Part A offers an illustration about the relationship between the oxygenation of Hb and the measured BOLD signal. Part B presents a general overview of vascular system activity and the BOLD signal. 3

Figure 1-2: The canonical Hemodynamic Response Function. 4

Figure 1-3: The basics of fMRI recording from the brain. The brain is divided into cubes, referred to voxels. Each voxel is composed of thousands of dense neurons. Relative changes in the BOLD signal is an indirect indication of underlying neural activity. 4

Figure 1-4: Understanding EEG recording. Each electrode measures a summed electrical field produced by neural activity. Using several electrodes spread out across the scalp, EEG analysis is conducted for the resulted time courses of electrodes. 6

Figure 1-5: Shared information between EEG and fMRI. Both modalities may reflect the same neural activity and yet differ in measuring techniques. 7

Figure 1-6: EEG-fMRI integration concept. Information from each modality is combined with information from the other modality using certain weights, depending on the integration approach. 8

Figure 1-7: GLM approach for integrating EEG-fMRI. The time course of EEG regressors are convolved with HRF function and down-sampled to BOLD signal resolution. After extracting the time course of BOLD signal from Brain's voxels, the Beta coefficients of the linear relationship between EEG regressors and BOLD signal are estimated using GLM. 10

Figure 2-1: EEG-ms segmentation over time. During any recording of EEG, each point can be assigned to one of four canonical EEG-ms classes. 21

Figure 2-2: A diagram of the main steps for extracting EEG-ms from N subjects..... 27

Figure 3-1: EEG-ms topographies for both groups—HC group top row, MA group lower row. The obtained EEG-ms topologies are similar to those reported previously in the literature. 35

Figure 3-2: Average duration for EEG-ms classes (A-D) for MA and HC groups (p-value corrected for multiple comparisons using Bonferroni-Holm). Results revealed a trend towards significance for MS-C with p=0.09. 36

Figure 3-3: Occurrence frequency of EEG-ms classes (A-D) for both MA and HC groups. For each EEG-ms class, no statistically significant difference among the two groups was found. 36

Figure 3-4: Transition probabilities for MA and HC groups (A); and (B) represents connections with the statistically significant difference between two groups—red and blue arrows indicate the direction of the changes in the transition probabilities (red represent an increase, while blue represent a decrease for MA compared to HC). p-values corrected for multiple comparisons using Bonferroni-Holm. The level of significance was set to $p<0.05$. 38

Figure 3-5: The ratio of subjects with non-stationary transition matrices ($p< 0.05$) of EEG-ms evaluated at different block lengths. 41

Figure 3-6: The semi-log time-lagged mutual information plot for the MA and HC groups at different time lags. The shaded area represents the 95% confidence intervals for each group. 42

Figure 3-7: Time-lagged mutual information plots for each class of EEG-ms averaged across subjects of each group. The shaded area represents the 95% confidence intervals for each group. 42

Figure 4-1: Feature extraction procedure. Each channel is divided into m epoch. From there, each epoch was filtered into α, β, θ, γ, and W frequency bands. Then, for each filtered epoch, the desired features were extracted. This resulted in m feature value from all epochs, which are then averaged to estimate the channel-level feature. In the figure, each feature is represented using three indices: f (channel, epoch, band) with channel= [1...N]; epoch= [1...m]; and band = [α, β, θ, γ, W]. The final out is a channel-level feature represented with two indices f (e.g., channel, band). 62

Figure 4-2: The effect of removing correlated features on prediction. 64

Figure 4-3: The nested-cross-validation procedure for predicting age. The example here demonstrates the first fold of the outer loop. The procedure consists of an inner loop (yellow color) and outer loop (grey color). The inner loop is used to find the best models to predict age. The outer loop uses those models to predict the age on the testing set. The process is repeated for all folds of the outer loop, which results in building a prediction of age from all samples. 67

Figure 4-4: The complete framework for estimating the BrainAGE from EEG. The framework uses the nested-cross-validation method to build estimations for age. Those estimations are then used to calculate BrainAGE from the entire dataset. 68

Figure 4-5: Model performance in terms of the explained variance using NCV. Error bars represent the standard deviation of performance across the outer loop of the NCV. 69

Figure 4-6: Model performance in terms of MAE using NCV. Error bars represent the standard deviation of performance across the outer loop of the NCV. 69

Figure 4-7: Predicted age vs. age constructed from the outer loop of the NCV. 70

Figure 4-8: The 20 most important features for predicting age, sorted from most important (bottom) to least important (top). Ventricle axis shows the scoring values from the stack-ensemble model predictor, while the color indicates the correlation values between that feature and age. 71

Figure 4-9: PDP for the top feature from NCV via the stack-ensemble model 72

Figure 4-10: Mean feature importance scores sorted by bands and channels for predicting age. The darker the color, the more important the feature. 73

Figure 4-11: The effect of the number of samples on age prediction. 74

Figure 5-1: The selected ROIs for feature extraction from fMRI colored based on the indices of the ROIs. The top part represents the 2D Axial view for the locations of the ROIs, and bottom part shows the 3D Sagittal view of the ROIs. 82

Figure 5-2: fMRI preprocessing pipeline. 85

Figure 5-3: Age prediction fusion from EEG -fMRI features. The predicted age values from each set of features (Age_{EEG}, Age_{ALFF}, and Age_{FC}) are used to train a GLM model using cross-validation. The final predicted age (Age_{Fusion}) is constructed from GLM prediction. 87

Figure 5-4: The correlation between age and the predicted age using SVM for ALFF, EEG, and FC features. 88

Figure 5-5: The correlation between age and the predicted age using RF for ALFF, EEG, and FC features. 88

Figure 5-6: The correlation between age and the predicted age using the ensemble model for ALFF, EEG, and FC features. 89

Figure 5-7: The predicted age vs. the chronological age using GLM prediction fusion. 90

Figure 5-8: The correlation matrix of predicted age values from EEG, ALFF, and FC set of features. 90

Figure 6-1: A sample of EEG-ms regressors to inform fMRI. Each regressor is used by the GLM to estimate Beta coefficients. 101

Figure 6-2: EEG-ms inform fMRI analysis framework for N subjects (Subj). The Beta coefficients of GLM are estimated for individual subjects. The statistical analysis of Beta coefficients reveals the brain regions that are active with respect to EEG-ms features. Later, those brain regions can be used as brain templates representation for the corresponding EEG-ms features. Several post-hoc analyses can be conducted based on the obtained brain templates; Beta analysis can be conducted to estimate the variation in the linear relationship between EEG-ms feature and BOLD signal. On the other hand, FC Analysis may reveals any changes in the connectivity between those brain regions... 105

Figure 6-3: EEG-ms templates for HC and MA. 106

Figure 6-4: Significant clusters for MS-A. Clustering was performed at $p<0$ .005 and corrected at $p<0.05$. 107

Figure 6-5: Significant clusters for MS-B. Clustering was performed at $p<0.005$ and corrected at $p<0.05$. 107

Figure 6-6: Significant clusters for MS-C. Clustering was performed at $p<0.005$ and corrected at $p<0.05$. 108

Figure 6-7: Significant clusters for MS-D. Clustering was performed at p<0.005 and corrected at p<0.05. 108

Figure 6-8: Statistical analysis for FAIR metrics between HC and MA subjects. Error bars represent the standard error. The p-value of the t-test is shown at the top of each bar pairs. 110

Figure 6-9: Statistical analysis for FAIR metrics between HC and subgroups of MA subjects. Error bars represent the standard error. The p-value of the t-test is shown at the top of each bar pairs. 111

Figure 6-10: Statistical analysis for Coherence-based FAIR metrics between HC and MA subjects. Error bars represent the standard error. The p-value of the t-test is shown at the top of each bar pairs. 112

Figure 6-11: Statistical analysis for Coherence-based FAIR metrics between HC and subgroups of MA subjects. Error bars represent the standard error. The p-value of the t-test is shown at the top of each bar pairs. 113

Figure 6-12: Graph analysis for HC vs. MA subjects estimated at different edge densities. The analysis shows the small-worldness index, clustering coefficient, path length, node betweenness, and efficiency (ns: not significant difference, *: p<0.05 and **: p<0.01). 114

Figure 6-13: Graph analysis for HC vs. Dep subgroups estimated at different edge densities. The analysis shows the small-worldness index, clustering coefficient, path length, node betweenness, and efficiency (ns: not a significant difference, *: p<0.05 and **: p<0.01). 115

Figure 6-14: Graph analysis for HC vs. Dep+Anx subgroups estimated at different edge densities. The analysis shows the small-worldness index, clustering coefficient, path length, node betweenness, and efficiency (ns: not significant difference, *: $p<0.05$ and **: $p<0.01$). 116

Figure 6-15: Graph analysis for Dep+Anx vs. Dep subgroups estimated at different edge densities. The analysis shows the small-worldness index, clustering coefficient, path length, node betweenness, and efficiency (ns: not significant difference, *: $p<0.05$ and **: $p<0.01$). 117

Figure 6-16: Correlation analysis between FC of the brain regions associated with significant connections obtained from Chapter 3 and PHQ. 119

Figure 6-17: Correlation analysis between Coherence of the brain regions associated with significant connections obtained from Chapter 3 and PHQ. 120

Figure 7-1: An illustrative example of GFP peaks and the gap between peaks..... 127

Figure 7-2: Inter-peak distribution from an exemplar dataset. 127

Figure 7-3: Inter-peak distribution taken from 43 HC subjects. 128

Figure 7-4: EEG-ms templates correlation matrix..... 129

Figure 7-5: Boxplot of noise level effects on the average duration of MS-D (ns: not a significant difference, *: $p<0.05$, **: $p<0.01$ and ***:$p<0.005$). 130

Figure 7-6: Boxplot of noise level effect on the occurrence of MS-D (ns: not a significant difference, *: $p<0.05$, **: $p<0.01$ and ***:$p<0.005$). 130

Figure 7-7: The effect of noise level on the transition probability between MS-C and MS-D (ns: not a significant difference, *: $p<0.05$, **: $p<0.01$ and ***:$p<0.005$). 131

Figure 7-8: An example of the noise effect on MS-D occurrence taken from five randomly selected subjects. 131

Figure 7-9: The Manhattan plot for the t-test of MS-A occurrence before and after adding noise with 100 repetitions. 133

Figure 7-10: The Manhattan plot for the t-test of MS-D occurrence before and after adding noise with 100 repetitions. 133

Figure 7-11: An example of the suggested probabilistic EEG-ms assignment. 135

List of Tables

Table 3-1: Correlation results among connections B to C and A to D and subjects' assessment measures. Correlation was estimated after combing both groups (n.s.: not a significant). 39

Table 3-2: Correlation results among connections B to D and D to B and subjects' assessment measures. Correlation was estimated after combing both groups (n.s.: not a significant). 39

Table 3-3: Markovian property and symmetry assessment for both groups. 40

Table 4-1: Summary of related work for predicting age from brain imaging data. 55

Table 4-2: The extracted features from EEG data. 60

Table 5-1: The performance of age prediction from EEG, ALFF, and FC set of features. 89

Table 6-1: Demographics of EEG-ms Informed fMRI analysis dataset. The MA subjects were divided into four subgroups based on the comorbidity of symptoms. 97

Table 6-2: Demographics of EEG-ms Informed fMRI analysis dataset with combined MA subgroups. 98

Table 6-3: Significant clusters from the healthy control group after applying one-sample t-test on the GLM coefficients. 109

Abstract

Determining clinically relevant biomarkers of mental disorders for reliably indicating pathophysiological processes or predicting therapeutic responses remains a major challenge, despite decades of research. Identifying such biomarkers can help patients significantly improve their quality of life and alleviate their suffering. Electroencephalography (EEG) and functional magnetic resonance imaging (fMRI) are non-invasive tools to investigate neurobiological mechanisms underlying mental disorders. Extracting and leveraging informative features from the high temporal resolution EEG and high spatial resolution fMRI may offer a more comprehensive understanding of brain spatial and temporal activities in health and disease. More importantly, this information can lead to a better understanding of the neurobiology of mental illness. This dissertation investigates the analyses and applications of extracting and combining informative features from EEG and fMRI, along with applying machine learning (ML) and computational methods for building biomarkers of mental illnesses.

Several methodological challenges in the extraction of informative and reproducible features are also addressed. First, two types of EEG features obtained from resting state EEG-fMRI measurements were extracted: 1) broadband-multichannel EEG dynamical features, called EEG microstates (EEG-ms); and 2) heterogeneous, static EEG features. Using EEG features only, results elucidate that: 1) EEG-ms characteristics and information theoretical properties can successfully differentiate individuals with mood

and anxiety disorders from healthy comparison subjects with potential applications for other clinical groups; and 2) heterogeneous static EEG features can successfully predict "brain aging," noted here as BrainAGE from 468 EEG datasets, achieving a correlation of r=0.61 between predicted age and chronological age.

Next, extracted EEG features were leveraged with fMRI to enhance the predictivity of BrainAGE and localizing the associated EEG-ms brain regions. More specifically, static EEG features were combined with resting state fMRI features to construct a multimodal BrainAGE predictor as a case study. Notably, it was found that EEG and fMRI contain a large portion of shared information about age, although each modality has its fingerprint of the aging process. The developed approach is a general purpose and be applied to predict other outcomes from brain imaging data. Similarly, EEG-ms features were integrated with fMRI to localize associated brain regions within fMRI space, revealing functional brain connectivity changes in individuals with mood and anxiety disorders as a case study. As a result, harnessing combined EEG-fMRI methods have enriched our knowledge some mental disorders and broadened our understanding of them with potential applications for other clinical groups and outcomes. Finally, this work evaluated the reproducibility and replication of EEG-ms analysis to address technical issues that have thus far been overlooked in the literature.

In conclusion, the presented work describes technical methods developed to study and discover several clinically translatable biomarkers that can be reliably used to characterize various mental disorders.

Chapter 1 : Primer on EEG–fMRI Analysis

1.1 Introduction

The human brain may be considered among the most complex dynamical systems. In terms of functionality, the brain is organized into large neural clusters, which are synchronized among each other to form a set neurocognitive and functionally neural network [1, 2]. The high level of synchrony allows the networks to work collaboratively for sustaining necessary and complex human actions, like walking, speaking, writing, or even flying an airplane. While the spatial distribution of these networks is widely agreed upon, the underlying neural mechanism(s) have remained understudied, and many unanswered questions remain. Elucidating the underlying mechanism's governing the brain's temporal dynamics may help us to better understand how the brain works, and more importantly for this dissertation, how mental disorders alter these neural functionalities. Various techniques are available to measure brain activity and extract information that directly or indirectly characterizes the functionality of brain networks. Among those techniques, electroencephalography (EEG) and functional magnetic resonance image (fMRI) stand out due to their safe and non-invasive techniques. fMRI measures the change in the blood oxygenation level-dependent (BOLD) signal induced by neural activity. EEG measures the underlying electrical activity produced by large

coherent electric activities of pyramidal neurons. Thus, both modalities reflect and capture similar neural activity but do so using different signal mechanism formation. Recently, combing these modalities has become possible; hence, more valuable information can be drawn from analyzing both modalities. The next section offers an overview of fMRI, EEG, and the foundations of combing principles.

1.2 fMRI Signal and Measurement

fMRI relies on the magnetic property of the hemoglobin molecule, which depends on whether or not the molecule is attached to oxygen. Oxygenated hemoglobin (Hb) is diamagnetic due to the absence of unpaired electrons. Thus, the presence of external magnetic field (e.g., MRI polarizing magnetic field B_0) Hb effect on a magnetic field in its vicinity is minimal. In contrast, deoxygenated hemoglobin (dHb) influences a more polarizing magnetic field in its vicinity due to the existence of unpaired electrons. Deoxygenated blood has a magnetic susceptibility that is approximately 20% greater than fully oxygenated blood [3]. The contrast (i.e., measured effect in the local magnetic fields changes) is then identified as the difference between oxygenated and deoxygenated hemoglobin concentrations. When a brain region becomes active, it consumes energy and uses oxygen for that process, resulting in deoxygenation of hemoglobin and local increase

of fully oxygenated blood flow [4-7]. Figure 1-1 depicts an illustrative example of the relationship between BOLD signal and hemoglobin.

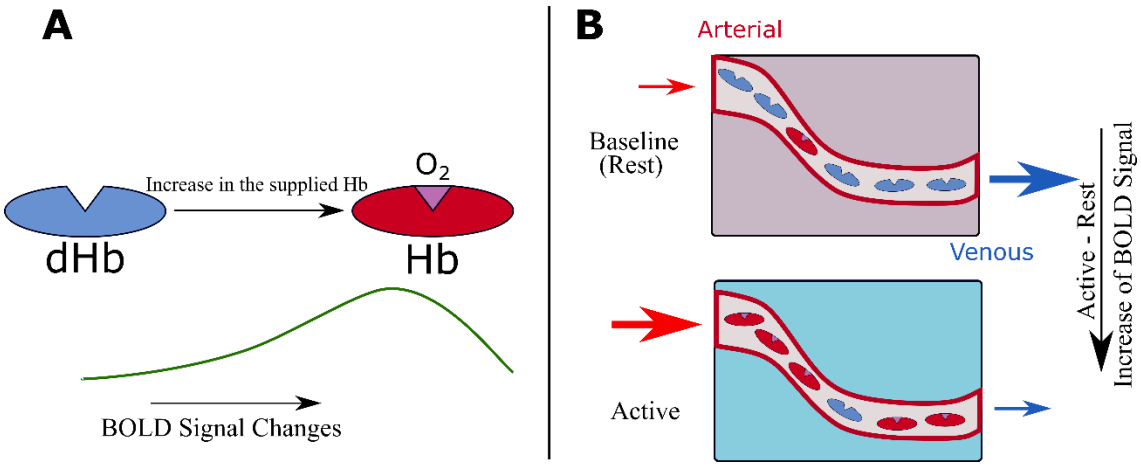


Figure 1-1: The basics of measuring the BOLD signal. Part A offers an illustration about the relationship between the oxygenation of Hb and the measured BOLD signal. Part B presents a general overview of vascular system activity and the BOLD signal.

Change in the magnetic resonance (MR) signal due to the neural activity can be modelled with the hemodynamic response function (HRF), which is usually divided into a series of phases as a response to an event. Firstly, the initial small decline of the HRF is a short-term decrease in MR signal immediately following neural activity and can be explained as the immediate increase in deoxygenated hemoglobin due to oxygen extraction before the vascular system overcompensates for oxygen consumption. Secondly, as heightened neural activity demands more blood flow to supply energy to the current brain region, deoxygenated hemoglobin starts to decrease rapidly. Therefore, the MR signal recorded from a particular voxel in this brain region begins to increase. Typically, the HRF peak is reached two to four seconds after a particular event (i.e., brain activity). Finally, when neural activity has ceased, the BOLD signal begins to decrease to a level that is below the baseline; this reduction is called the HRF under-shoot. Later, when blood volume returns

to its normal flow, the MR signal returns to its pre-event baseline state. Figure 1-2 presents a plot for the canonical HRF function, highlighting the phases explained above.

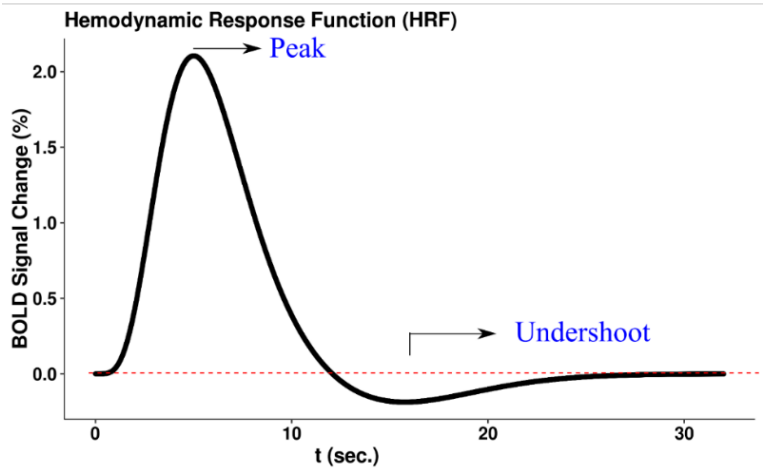


Figure 1-2: The canonical Hemodynamic Response Function.

An illustrative example of the fMRI recording is demonstrated in Figure 1-3.

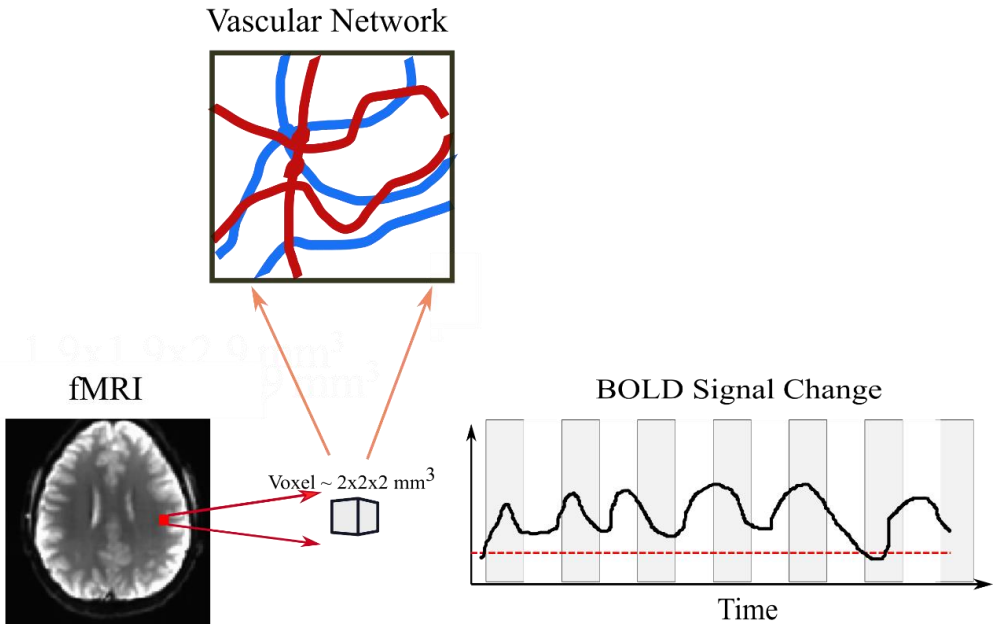


Figure 1-3: The basics of fMRI recording from the brain. The brain is divided into cubes, referred to voxels. Each voxel is composed of thousands of dense neurons. Relative changes in the BOLD signal is an indirect indication of underlying neural activity.

Due to the nature of fMRI (i.e., entire brain recording parameters), its temporal resolution is on the order of ~0.6-2 seconds. This imposes limitations on deriving conclusions about the temporal dynamics of the brain. When recording the entire brain fMRI data at multiple time points, the brain is divided into cubes, typically with relative dimensions of $2\times2\times2$ mm^3, referred to as voxels, and time course of the fMRI signal in each brain voxel is recorded simultaneously. For fMRI analysis, the BOLD time course signal from each voxel is used for subsequent analysis. An illustrative example of the fMRI recording is demonstrated in **Figure 1-3**.

1.3 EEG Signal and Recording

EEG signal primarily results from electrical activities of a large population of pyramidal neurons synchronized in space and time. As the brain is functionally divided into interleaving networks, the central processing units are neurons that form hubs of these networks. When evoking a network, neurons become active and produce electrical and magnetic fields. EEG sensors placed on the scalp obtain and record summed electrical field effects (e.g., electric potentials) from active neurons (See **Figure 1-4**). This summation of electrical signal provides a direct and high-temporal resolution measurement of brain activity. However, the fact that the measure is conducted at the scalp (e.g., order of 2 to 4 cm away from cortical electric dipole sources) brings into question the accuracy of spatial localization of the precise source location of neural activity. The problem is ill-posed without a unique solution—rather an infinite number of possible source configurations [8].

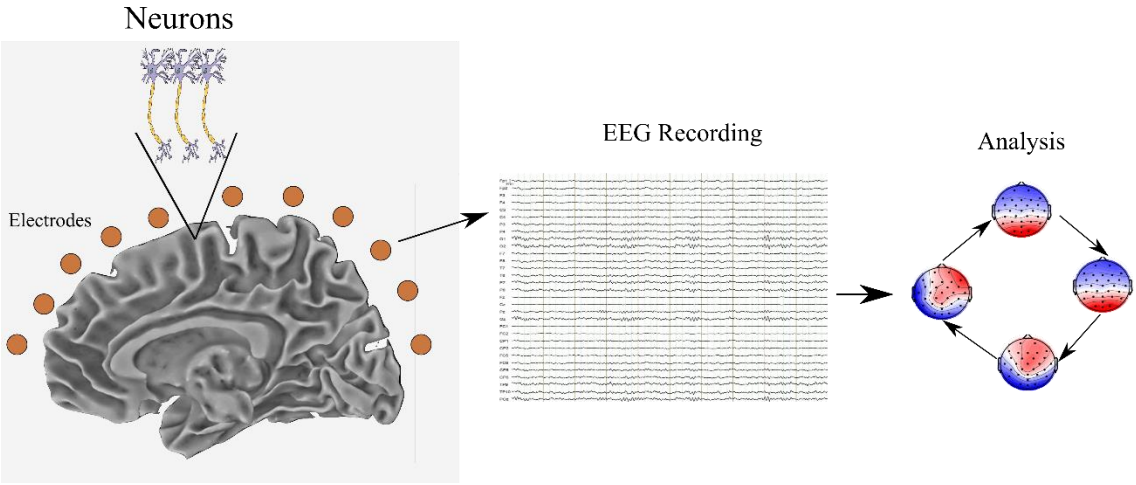


Figure 1-4: Understanding EEG recording. Each electrode measures a summed electrical field produced by neural activity. Using several electrodes spread out across the scalp, EEG analysis is conducted for the resulted time courses of electrodes.

1.4 Combining EEG-fMRI

Both EEG and fMRI have strengths and weaknesses. Foremost, EEG is a direct measure of brain neuronal activity with a high temporal resolution (e.g., order of milliseconds [ms]), although it suffers from low spatial resolution. On the contrary, fMRI can detect hemodynamic changes associated with brain neuronal activity and has an excellent spatial resolution, albeit with low temporal resolution (e.g., order of 1s). Therefore, combining information from both techniques can significantly enhance our understanding of the brain's spatio-temporal neuronal activity and, thus, how different mental disorders alter functionalities of the brain. This work utilized simultaneous EEG-fMRI data and integrated EEG and fMRI analysis, where information from EEG data is used to provide a better understanding of the functional connectivity of specific spatial locations within and across the brain. Hence, detailed temporal information from EEG can be combined with high spatial fMRI resolution. Thus, one can assume that both EEG

and fMRI can capture and reflect the same neural activity in the brain [4-7, 9-13] (See **Figure 1-5**). Therefore, combining information from EEG and fMRI can enhance our knowledge of when, where, and what is happening during various brain functions. To do so, EEG data (e.g., time or frequency) are utilized in the fMRI side by correlating BOLD signal with EEG-derived metrics.

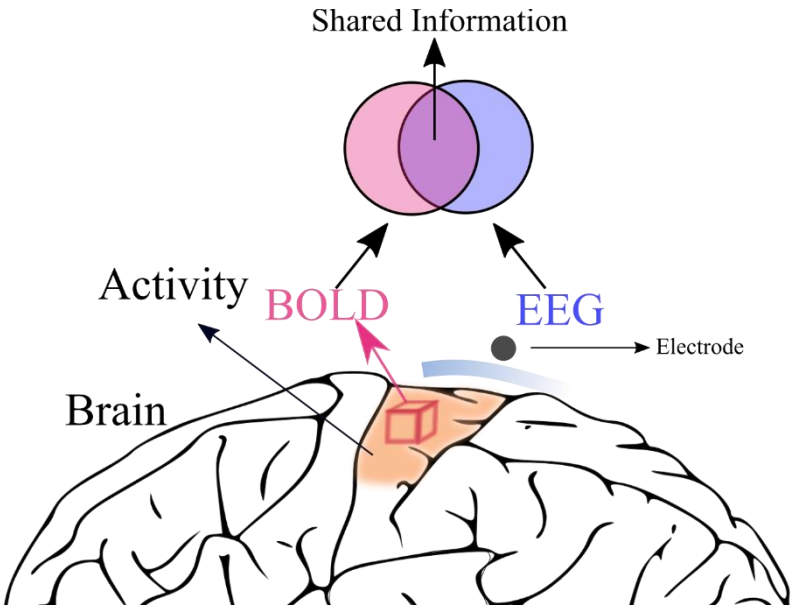


Figure 1-5: Shared information between EEG and fMRI. Both modalities may reflect the same neural activity and yet differ in measuring techniques.

1.5 Methods of Integrating EEG-fMRI Data

Based on the weight of each modality in the overall model, combining EEG–fMRI can be divided into either asymmetrical or multimodal fusion (**Figure 1-6**).

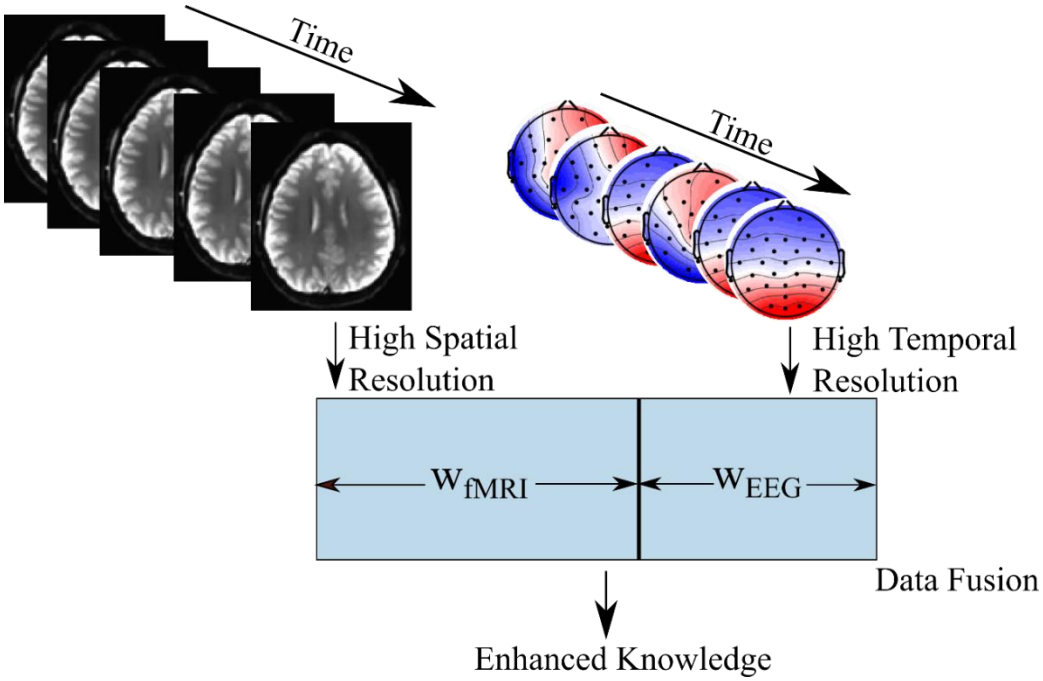


Figure 1-6: EEG-fMRI integration concept. Information from each modality is combined with information from the other modality using certain weights, depending on the integration approach.

1.5.1 Asymmetrical EEG-fMRI Integration

Asymmetrical integration relies on using one modality to inform the other by benefiting from either the high temporal resolution of EEG or the high spatial resolution of fMRI. Thus, one can divide the asymmetrical integration into EEG-informed fMRI and fMRI-informed EEG analyses.

- *EEG-informed fMRI*

In this type of analysis, high temporal resolution information from EEG are used to generate regressors, and then used for fMRI data analysis to localize the brain regions associated with effect (i.e., revealing brain regions with a significant association between EEG information and hemodynamic brain activity). This type of analysis does not impose

any assumptions about the neural generators of EEG in terms of spatial distribution. Therefore, selecting potential EEG information depends on the research question and the task. For instance, one can use specific frequency, event-related potential (ERP) information or even spectral information to inform fMRI. This freedom may sometimes come at the cost of the interpretability of results. Several studies have used this type of integration. For example, associating ERP features with changes in BOLD signal has been explored for attention [14-16], memory [17], and visual [18, 19] processing. Other EEG features have also been used to inform fMRI [20, 21], including the use of EEG-ms [22-25].

Methodologically, the General Linear Model (GLM) [26] is considered one of the primary approaches for combining EEG and fMRI information by relying on associating BOLD signal with EEG information. The time course of each voxel (i.e., response of neural activity at specific brain regions) is used to build a weighted sum of EEG information (or regressors), as follows:

$$y_i = \beta_1 x_{i1} + \beta_2 x_{i2} + \beta_3 x_{i3} + \cdots + \varepsilon_i \quad (1.1)$$

where *i* indexes each brain voxel; β_j indexes model parameters; x_{ij} is the regressor value associated with each model parameter β_j; and ε_i is the error term. The previous equation can be put into matrix format, as follows:

$$y = X\beta + \varepsilon \quad (1.2)$$

Regressors represent the effects of interest. However, fMRI response is delayed relative to onset time of neural activity. BOLD is induced by changes in blood flow rather than a direct neural measure; therefore, regressors should be convolved with the HRF (Figure 1-2) to account for signal delay. Various types of information can be used

as regressors. This project used EEG microstate (EEG-ms) features as regressors to inform and to interpret fMRI analysis (See **Figure 1-7** for a depiction of EEG-fMRI GLM modeling). The next chapter introduces EEG-ms and delineates the set of features that can be used as regressors.

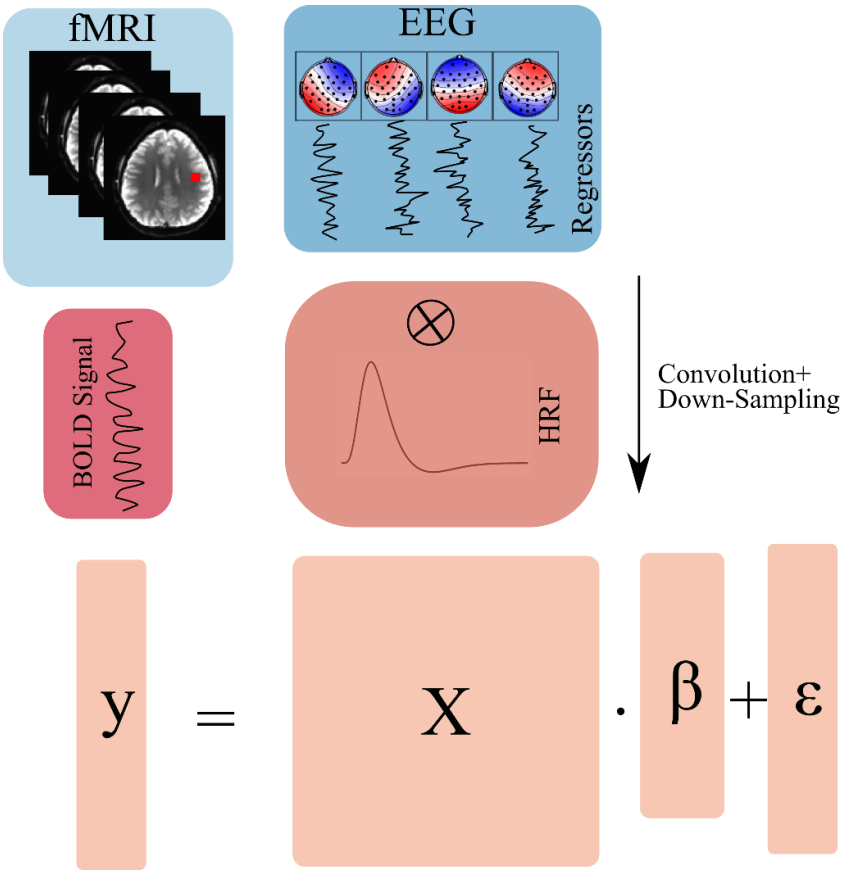


Figure 1-7: GLM approach for integrating EEG-fMRI. The time course of EEG regressors are convolved with HRF function and down-sampled to BOLD signal resolution. After extracting the time course of BOLD signal from Brain's voxels, the Beta coefficients of the linear relationship between EEG regressors and BOLD signal are estimated using GLM.

fMRI-informed EEG

In this type of integration, the information from functional and structural MRI data is used to guide EEG analysis for improving EEG source localization and for alleviating the low spatial resolution of EEG data. Various algorithms used to localize sources of EEG data assume a particular biophysical structure of the brain (e.g., brain tissues and skull electric conductivities), and, thus, fMRI can be used to relax and gain a better estimate of the activity or limit the search space of the neural generators. Hence, this approach assumes that fMRI carries information about the neural activity (i.e., neural activity is always accompanied by changes in BOLD activity)—an assumption that is not always valid. While this approach is now less common than EEG-informed fMRI analysis, it is still being used in the literature [27-29].

1.5.2 Multimodal Fusion

Unlike asymmetric integration, multimodal fusion does not favor one modality over the other but instead utilizes supervised or unsupervised approaches to deduce latent variables from both modalities [30-33]. In other words, both EEG and fMRI data are concatenated at the same level, and then latent variables from both modalities are extracted. This fusion approach relies on the nature of the deployed methods, as well as various research assumptions. One of the most common approaches to fuse data is independent component analysis (ICA), which relies on the assumption that the data can be decomposed into a set of linearly independent sources [34]. While multimodal fusion may overcome the issue of the biased representation in asymmetric data confusion, interpretation of multimodal fusion results is more challenging.

1.6 EEG and fMRI for Discovery of Mental Disorders Biomarkers

The brain concurrently processes a tremendous amount of information in both time and space [1, 2]. Thus, it is plausible to assume that there is an association between mental disorder symptoms and alterations in brain functionality. Studying brain functionality in different mental disorders can provide indicators about those mental disorders. However, the relationship might be more complex than can be explained by mere changes in the functionality of the brain. Nevertheless, mental disorders certainly may have a strong influence on the brain spatial and temporal neural activities that could be detected by brain multimodal EEG-fMRI imaging.

Concurrent processing occurring in regions across the brain is measured by the brain's functional connectivity (FC) during fMRI recording while individuals are in a resting state [35]. FC has been used for characterizing various disorders, including major depressive disorder [36], generalized anxiety and panic disorders [37], Alzheimer's disease [38], schizophrenia [39] and autism [40]. EEG, on the other hand, has also achieved remarkable diagnostic accuracy for several disorders, such as epilepsy [41], depression [42] [43], anxiety disorders [44], schizophrenia [45] and Alzheimer's disease [46]. Moreover, the combination of EEG and fMRI has also been used to advance our understanding of post-traumatic stress disorder (PTSD) [22], depression [47], and epilepsy [48]. Thus, neuroimaging techniques provide great potential in identifying brain-based biomarkers of mental disorders that may aid in clinical screening, early intervention, and treatment outcome evaluation.

The work presented herein aims at enriching brain-based disorder classification by using several analyses, including EEG, fMRI, and simultaneous EEG-fMRI to attempt

to differentiate individuals with mood and/or anxiety disorders [MA] (e.g., major depressive disorder, social phobia, generalized anxiety disorder, posttraumatic stress disorder, and/or panic disorder) from healthy control (HC) comparison subjects without a current or lifetime history of such disorders.

1.7 Dataset of Simultaneous EEG-fMRI Recording

Participants were selected from the first 500 subjects of the Tulsa 1000 (T-1000), a naturalistic study assessing and longitudinally following 1000 individuals, including healthy comparisons and treatment-seeking individuals with mood disorders and/or anxiety, substance use, and eating disorders [49]. The T-1000 study aims to determine how MA, substance use, and eating behaviors organize across different levels of analysis with a focus on predictors of long-term prognosis, symptom severity, and treatment outcome. The T-1000 study is conducted at the Laureate Institute for Brain Research in Tulsa, Oklahoma. The study human research protocol was approved by the Western Institutional Review Board. All participants provided written informed consent and received financial compensation for participation. As detailed [49], the participants in this work were screened on the basis of treatment-seeking history and dimensional psychopathology scores: Patient Health Questionnaire-9 (PHQ-9) ≥ 10 and/or Overall Anxiety Severity and Impairment Scale (OASIS) ≥ 8. Each participant underwent approximately 24 hours of testing over the course of one year, including a standardized diagnostic assessment, self-report questionnaires, behavioral and physiological measurements indexing RDoC domains, and blood/microbiome collection. A structural MRI, resting-state fMRI, task-based fMRI during reward-related processing, fear

processing, cognitive control/inhibition, and interoceptive processing were also collected with simultaneous EEG recording. Please refer to **Appendix A** for detailed clinical assessment information. Specifications for subjects are reported in each chapter, including the clinical population, recording type, and other preprocessing steps.

1.8 Data Acquisition of Simultaneous EEG-fMRI

MRI imaging and simultaneous EEG-fMRI was conducted on a General Electric Discovery MR750 whole-body 3T MRI scanner with a standard 8-channel, receive-only head coil array. A single-shot gradient-recalled EPI sequence with Sensitivity Encoding (SENSE) was employed for the fMRI acquisition. EEG signals were recorded simultaneously with fMRI using a 32-channel, MR-compatible EEG system (Brain Products GmbH) with measuring electrodes arranged according to the international 10–20 system. ECG signal was recorded using an electrode on the subject's back. In order to synchronize the EEG system clock with the 10 MHz MRI scanner clock, a Brain Products' SyncBox device was utilized. The EEG acquisition of temporal resolution and measurement resolutions was 0.2 ms (i.e., 16-bit 5 kS/s sampling) and 0.1 μV, respectively. Hardware filtering throughout acquisition in a frequency band between 0.016 and 250 Hz was applied to EEG signals.

1.9 Summary of Contributions

The following points summarize the contribution of this work.

- Revisiting mathematical derivation of EEG-ms extraction and revealing several issues that have been overlooked in the literature (**Chapter 2** and **Chapter 7**).

- Building a toolbox for extracting EEG-ms with various configurations based on **Chapter 2**.
- Extracting and identifying biomarkers for MA subjects using EEG-ms features and information theory. Published in [44].
- Modeling and implementing an extensive feature extraction from EEG data. Published in [50].
- Building a comprehensive ML framework to study BrainAGE and other responses from EEG data. Published in [50].
- Analyzing the shared information analysis between EEG and fMRI for predicting BrainAGE (**Chapter 5**).
- Building a Combined EEG-fMRI ML framework for predicting BrainAGE and other responses.
- Utilizing and building a pipeline for using EEG-ms to inform fMRI with a case study on MA subjects (**Chapter 6**).
- Analyzing various parameters that can affect EEG-ms feature extraction and proposal of a new approach for conducting robust EEG-ms analysis (**Chapter 7**).

1.10 Dissertation Outline

This dissertation is organized as follows.

Chapter 2. EEG Microstates: Theory, Principles, and Analyses

This chapter offers a mathematical and theoretical explanation for EEG-ms extraction, detailing the necessary steps to move EEG-ms from subject-level to group-level analysis.

Chapter 3. Evidence of altered EEG Microstates' Temporal Dynamics in Individuals with Mood and Anxiety Disorders

Using EEG-ms features explained in Chapter 2, this chapter explores the alteration of EEG-ms properties in individuals diagnosed with MA when compared with HC subjects from the Tulsa-1000 study.

Chapter 4. Predicting Age from EEG Using Unbiased Machine Learning Framework

The interaction between heightened mental illness and accelerated brain aging has been relatively unexplored, yet, may provide insight into mechanisms characterizing symptom severity. This chapter explores the feasibility of predicting age from EEG data by extracting a set of widespread and heterogonous features from EEG data. Also, this chapter presents a non-biased machine learning (ML) framework for regression from biomedical data.

Chapter 5. BrainAGE Prediction Using Simultaneous EEG-fMRI Features

Extending the work in Chapter 4, Chapter 5 investigates how much information EEG and fMRI share with regard to age. FC metrics were extracted, as well as the amplitude of low-frequency fluctuation (ALFF) features from fMRI. Then, those features were used along with EEG features obtained in Chapter 4 to build a more comprehensive age predictor.

Chapter 6. Studying Brain Based Biomarkers of Mood and Anxiety Disorders: An EEG-ms Informed fMRI Analysis

Localizing the effect of EEG-ms features in the fMRI domain may help to overcome the low spatial resolution of EEG-ms analysis. Given that Chapter 4 details alterations of EEG-ms transition dynamics in MA subjects, this chapter explains how templates of EEG-ms representation in the brain were extracted from HC subjects using GLM

modeling. Then, the global FC among EEG-ms templates was explored and correlated with a specific MA symptom to better understand alterations in individuals with significant psychopathology.

Chapter 7. Proposal of a New Approach to Analyze EEG Microstates Data

One of the goals of human subject research is to produce reliable and robust results, which could be replicated independently. This chapter addresses several practical issues with reproducing EEG-ms results. First, the chapter explains several challenges of EEG-ms extraction and analyses, along with the exemplary data. Then, it provides some guidelines to avoid such challenges.

Chapter 8. Conclusion and Future Work

This chapter integrates all analyses presented in this dissertation and provides recommendations for further studies involving EEG and fMRI data.

Chapter 2 : EEG Microstates: Theory, Principles, and Analyses

2.1 Introduction

Electroencephalography (EEG) has been used for studying and phenotyping various types of neuropsychiatric and neurodegenerative disorders [51-53]. Recent efforts aim to discover and provide cost-effective, reliable markers for aberrant brain activity patterns relevant to major psychiatric disorders. Distinct topographic representation of the EEG electric scalp potentials—lasting a few dozen of a millisecond and coined an EEG-microstates (EEG-ms)—provides an opportunity and a novel tool for discovering unique markers of different brain disorders [54]. EEG-ms was first introduced by Lehmann, et al. [55], where it was revealed that EEG signals could be segmented into a few spatially independent quasi-stable (i.e., lasting a few dozen ms) states (i.e., microstates). The segmentation of EEG signals is carried out at extrema points of the EEG global field power (GFP), which can maintain a high signal-to-noise ratio (SNR) and provide a reliable source for identifying microstates (MSs) **Figure 2-1**. Two seminal reviews of EEG-ms were presented in [54, 56].

The functional interpretation of EEG-ms could be explained as coordinated and synchronized neuronal current activity of many neurons that happen to be activated together, as demonstrated in previous studies [54, 56]. Thus, a change in the topographies

of MSs may be attributed to a change in the orientation or distribution of the current dipoles [55, 57]. Alteration in the properties of EEG-ms presumably reflects a disruption in the underlying brain networking processes and information flow. Furthermore, spatially independent EEG-ms [55], and especially temporally independent EEG-ms [22, 23], were revealed to be correlated with resting state networks (RSNs), measured fMRI [23, 24, 58]. Additionally, other studies reported that EEG-ms are associated with particular mental processes [24, 56, 59-65]. The source localization of EEG-ms was investigated in [66], in which authors identified seven MSs (A through G) and localized the source of these MSs. Their results suggest a common activation among those MSs in the brain's main hubs (e.g., precuneus, anterior and posterior cingulate cortices, insula, superior frontal cortex, and other brain regions). Therefore, the EEG-ms can characterize network alteration or disruption in brain functionality due to disorders and offer potential biomarkers. Evidence of the relationship between mental processes and EEG-ms has led to several works aimed at studying EEG-ms properties in neuropsychiatric disorders. Early works of spatially independent EEG-ms focused on schizophrenia and showed moderate to substantial differences in EEG-ms properties between subjects with schizophrenia and healthy groups [67-71]. Other works have also revealed an alteration in EEG-ms for other diseases, like dementia produced by Alzheimer's [72-74]. Some neuropsychiatric illnesses were also shown to affect certain MSs, including depression [71], panic disorder [75], narcolepsy [76], multiple sclerosis [77] and Tourette syndrome [78].

It is reasonable to assume that the brain can be in one MSs at each time point in the ideal case. To understand modeling EEG-ms, the EEG-ms derivation was revisited and several

aspects were emphasized to ensure the quality of extracted MSs. While in the ideal case, it is reasonable to use the entire resting state dataset to compute individual templates of EEG-ms. Also, the level of noise within the EEG data might lead to data mislabeling. Assigning labels to each point in the EEG time course should also take into consideration that some points of EEG could be contaminated by noise. Thus, one suggestion is to label only points corresponding to high SNR (i.e., reflective of peaks in GFP) and interpolate data points in between (i.e., points that do not correspond to GFP peaks are assigned based on labels of the nearest peak).

GFP is commonly used to determine the extrema points, defined as the spatial standard deviation of EEG signals across all channels. GFP is a reference-free measure, wherein regardless of the EEG reference methods during and after EEG recording, the GFP will be the same. It has been shown that the peaks of GFP maintain a high SNR [54, 55]. Thus, focusing on GFP peaks may improve results. Furthermore, taking into consideration the peaks of GFP helps reduce the dimensionality of EEG data.

$$GPF = \sqrt{\frac{\sum_{i=1}^{p}(v_i(t) - \bar{v}_i(t))^2}{n}} \quad (2.1)$$

where p is the number of electrode; $\bar{v}_i(t)$ is the mean of electrode values at time point t; and $v_i(t)$ is the values of electrode i at time point t.

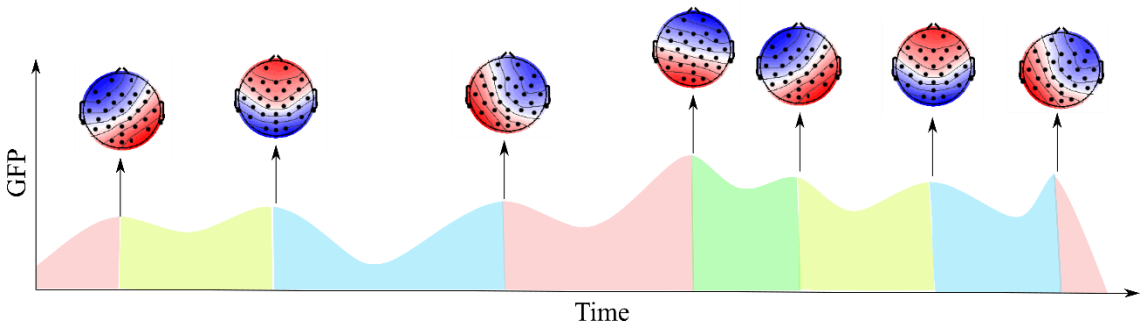


Figure 2-1: EEG-ms segmentation over time. During any recording of EEG, each point can be assigned to one of four canonical EEG-ms classes.

2.2 EEG-ms Modeling

EEG-ms assumes that EEG topographies of the brain can be explained by a set of states or, in this analysis, MSs. Typically, the number of MSs is between two and six states. Mathematically, one can represent EEG as a function of EEG-ms by the following equation:

$$x_t = \sum_{i=1}^{K} a_{it} T_i + \epsilon_t \tag{2.2}$$

where x_t $(p \times 1)$ is the electrodes value at timepoint t. a_{it} is a factor related to each MS at each time point and ϵ_t is an error term associated with assigning that time point to one of the MSs (i.e., noise due to the lack of explained topographical representation of that point by the assigned MSs template). K is the number of assumed MSs. Given the assumption that each time point in EEG can belong to one and only one MS holds (i.e., non-overlapping), then the following condition must be satisfied:

$$\begin{cases} a_{lt} a_{mt} = 0 \; \forall l \neq m \\ \sum_{i=1}^{K} a_{it}^2 > 0, \; \forall t \end{cases} \tag{2.3}$$

If T ($p \times K$) was normalized as following, then:

$$\|T_i\| = 1 \text{ and } (\mathrm{T}_i' T_j)^2 < 1 \; for \; i \neq j \text{ and } i, j \in [1..k]$$

The goodness of fit for time point x_i is given as follows:

$$f_i = x_i{}' \times T \tag{2.4}$$

The result is a vector $1 \times K$ corresponding to the fit of x_i against each template. Typically, each x_i is assigned to the MS with the highest fit.

$$L_i = \underset{k}{\operatorname{argmax}}(f_i) \tag{2.5}$$

To account for the polarity invariant property of EEG-ms, one should use the following equation instead:

$$L_i = \underset{k}{\operatorname{argmax}}(abs(f_i)) \tag{2.6}$$

However, T must first be randomly initialized, since there is no other information about T. Thus, there is a need for an iterative process to improve estimation for T. To do so, this research relied on finding the Eigenvector that corresponds with the largest Eigenvalue to update templates T. Let us first find the sample covariance S_i of all EEG points X_i that belong to the template T_i , where i is the index of the MS.

$$S_i = X_i X_i' \tag{2.7}$$

$$T_i = \underset{x}{\operatorname{argmax}}(X_i' S_i X_i) \tag{2.8}$$

The process of updating labels for each time should be repeated (2.6), as new templates are available. It should be noted that the process of updating the templates is a heuristic procedure. Thus, a stopping criterion is needed for iteratively updating templates. One way to evaluate the stopping criterion is to measure the explained variance by the template.

$$\sigma_D^2 = \frac{\sum_{i=1}^{n}(X'_i X_i)^2}{n(p-1)} \tag{2.9}$$

where σ_D^2 represents the fit around the mean for the dataset, n is the number timepoints in the considered dataset and p is the number of electrodes in the datasets. Thus, the explained variance can be written as:

$$\sigma_u^2 = \sum_{i=1}^{n}\left((X'_i X_i - (T'_i X_i)^2\right)/(n(p-1)) \tag{2.10}$$

The coefficient of determination R^2 (referred to as the global explained variance (GEV)) can be found as follows:

$$R^2 = 1 - \sigma_u^2/\sigma_D^2 \tag{2.11}$$

While the previous derivation of EEG-ms is the mathematical basis of any EEG-ms analysis, other variations appear frequently in the literature. The most common variation is referred to as Atomize and Agglomerate Hierarchical Clustering (AAHC) [79, 80]. The approach relies on top-down hierarchical clustering for EEG data. AAHC starts by assuming each EEG time point is cluster and then does iterative elimination (Atomizing) and merging, until reaching the desired number of clusters (K). Mathematically, AAHC assumes each EEG timepoint x_i a cluster and treats it as templates of clusters:

$$T = [x_i] \qquad i \in [1..n] \tag{2.12}$$

To find the potential clusters to eliminate (atomizing), the explained variance (EV) is calculated as follows:

$$EV_i = T_i \times T_i \quad i \in [1..n] \tag{2.13}$$

AAHC finds clusters with smallest fit for later elimination:

$$f_e = min(EV_i) \quad i \in [1..n] \tag{2.14}$$

Typically, the AAHC eliminate one cluster, T_e, at each iteration and assign it to the best fit cluster:

$$f_e = T' \times T_e \quad i \in [1..n] \ \wedge i \neq e \tag{2.15}$$

$$L_e = \underset{i \in [1..n] \wedge i \neq e}{argmax} \ (abs(f_e)) \tag{2.16}$$

Updating clusters is needed after each process of elimination and reassignment. This is done by deploying equations (2.7) and (2.8).

The processes of elimination, reassignment, and clusters updating are repeated until the number of remaining clusters is equal to the number of desired clusters.

The previous steps identify the templates from individual datasets. To compare different datasets (i.e., subjects), one should find the mean template across all subjects.

2.3 Generalization from Subject Level to Group Level

The template from subjects may not be similar to templates across all subjects from the same group. Keeping this in mind, it is important to find a common template across all subjects.

Let's first assume a random mean template ${}^{M}T_i$, and that the template from subject j is represented by superscript, such as ${}^{j}T_i$. To find the fit between the ${}^{M}T_i$ and subject template:

$${}^{j}f_i = {}^{j}T_i' \times {}^{M}T_i \tag{2.17}$$

As this procedure is for one subject, we must use the following to determine fit for N subjects:

$$F = [{}^{j}f_i] \text{ with } j = 1..N \tag{2.18}$$

Since the mean template was chosen arbitrarily (i.e., individual templates from subjects are not ordered), the mean must be updated. First, the subject with the smallest fit was determined:

$$r = \min_{f}(F) \tag{2.19}$$

Then, templates of the subject r corresponding to the smallest fit ${}^{r}T$ were permuted to find the best order for maximizing overall fit:

$${}^{r}T = ag\max_{T}({}^{r}f) \tag{2.20}$$

Next, the mean template was updated based on the new order. Eigenvector corresponding the largest Eigenvalue was used again to find the new mean template. First, sample variance across each template was found from all datasets:

$$S_i = T_i \times T_i' \tag{2.21}$$

with ${}^{j}T_i$ representing template i from all subjects.

$${}^{M}T_i = \operatorname{argmax}_{T}(T_i' S_i T_i) \tag{2.22}$$

The previous process was repeated for all templates until no subject remained for ordering. Having found the mean template for all datasets, each time point from each subject was reassigned to the corresponding template based on the mean template:

$$f_i = {x_i}^{T} \times {}^{M}T \tag{2.23}$$

$$L_i = \operatorname{argmax}_{k}(abs(f_i)) \tag{2.24}$$

The previous equation represents updated labels for each time point from each dataset. The next step is finding the corresponding features from each dataset.

2.4 EEG-ms Characteristics

From there, one can extract several EEG-ms characteristics:

- Average Duration of cluster k:

$$D_k = \frac{\text{sum}(L_{i=k})}{n \times Fs} \tag{2.25}$$

With Fs is the sampling rate of EEG.

- The occurrence of cluster k:

$$C_k = \frac{n}{\text{sum}(L_{i=k})} \tag{2.26}$$

- The transition probability (TP) between two clusters TP(p → q) across the entire dataset is given below:

$$TP(\text{u} \rightarrow \text{v}) = \frac{\text{sum}(L_{t=v} | L_{t-1=u})}{n} \tag{2.27}$$

2.5 Extracting EEG-ms in Practice

From the practical point of view, extracting EEG-ms can be summarized in **Figure 2-2**. There are necessary steps needed before conducting EEG-ms, including EEG preprocessing for artifacts removal and filtering. EEG-ms are sensitive for the presence of noise in EEG as has been shown the **Chapter 7**; hence, noise suppression is required. On the other hand, EEG filtering is commonly used in the literature with two options [2-20] Hz and [1-40] Hz [56].

Selecting EEG timepoints for extracting EEG-ms templates is achieved based on the peaks of GFP. Thus, extracting those peaks is necessary before extracting EEG-ms

templates. **Chapter** 7 provides analyses of the effect of using GFP peaks for extracting EEG-ms.

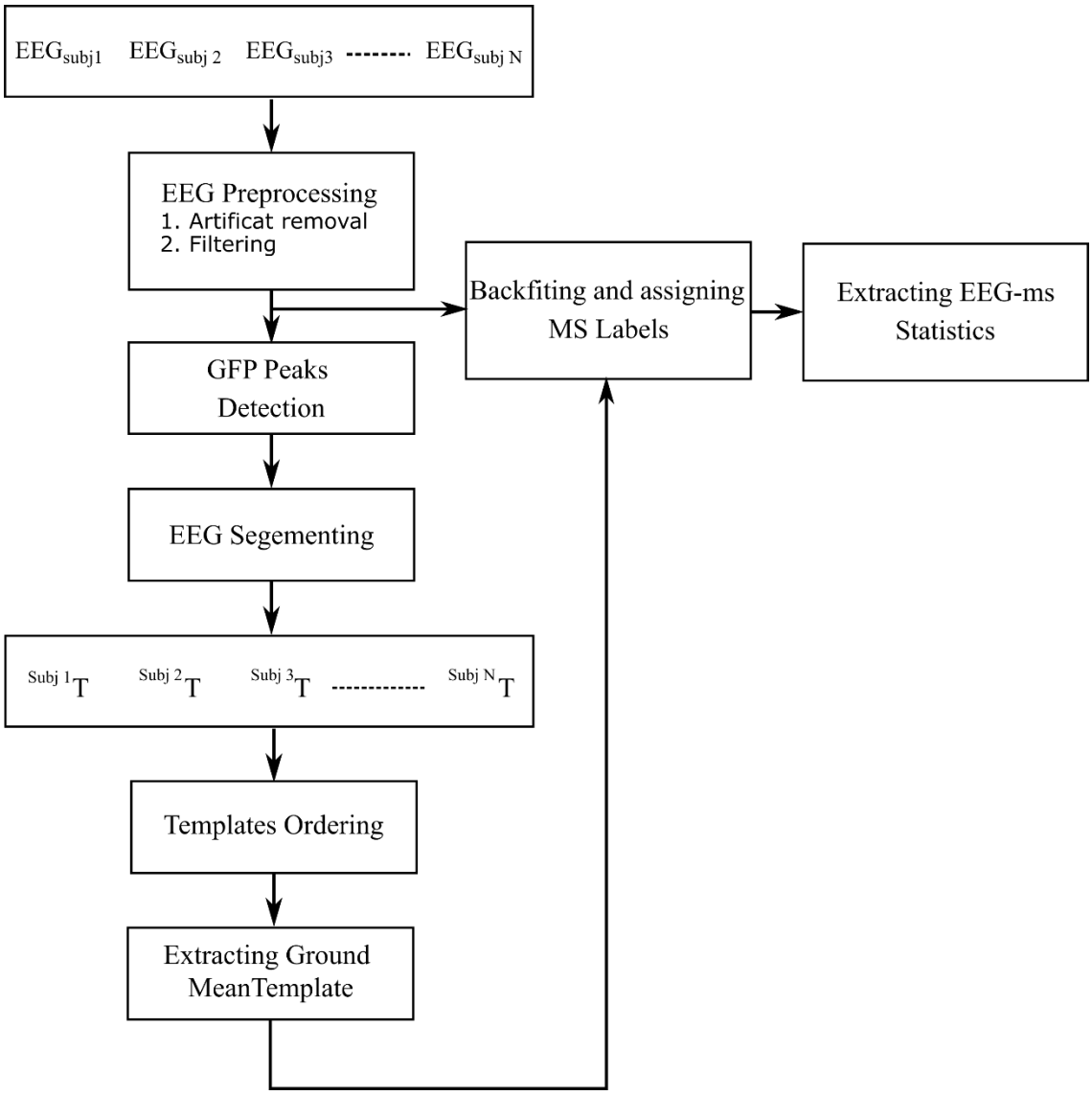


Figure 2-2: A diagram of the main steps for extracting EEG-ms from N subjects.

Chapter 3 : Evidence of Altered EEG Microstates' Temporal Dynamics in Individuals with Mood and Anxiety Disorders

(All the presented results in this chapter are reproduced and adapted from: *Al Zoubi, Obada, et al. "EEG Microstates Temporal Dynamics Differentiate Individuals with Mood and Anxiety Disorders From Healthy Subjects." Frontiers in human neuroscience 13 (2019): 56.)*

3.1 Introduction

Chapter 2 elaborated on EEG-ms analysis to extract potential biomarkers for mental disorders. This chapter uses the same analysis to study subjects with MA disorders and compare with HC subjects. MA demonstrated an altered brain network and brain region activities (e.g., default mode, executive, salience networks, and prefrontal cortex, cingulate cortex, hippocampus, and amygdala [81, 82]). Therefore, detecting and characterizing the dynamics of brain neuronal activity through transient spatio-temporal EEG-ms patterns may provide novel information and improve our understanding of the mechanisms of irregularities in cognitive and emotion processing among psychiatric disorders.

The typical spatially independent EEG-ms analysis is conducted by locating GFP peaks, and then clustering EEG points around these peaks. For running such an analysis, the desired number of MSs (i.e., clusters) must be specified before running the clustering algorithm. A majority of EEG-ms studies have used the four canonical MSs to study group

differences [56]; however, other studies have identified MSs in addition to the four canonical metrics [23, 66]. Although using a predefined number of clusters is arguable, it is preferable for comparisons among different groups. The literature was followed by defining the number of desired MSs (k = 4) for both MA and HC Tulsa-1000 groups [56]. Several characteristics for EEG-ms can be extracted, such as average duration, frequency of occurrence, and transition probabilities. Each property can be interpreted based on the underlying neural activities. For instance, the average EEG-ms duration represents the temporal stability of each MS, while the frequency of EEG-ms occurrence may represent the tendency of MSs to be active. Transition probabilities extract the asymptotic behavior of transitions between MSs (i.e., the likelihood of switching between different MSs). To further examine dynamics in the EEG-ms sequence, a new set of features introduced in [83] was adopted. An information-theoretical analysis is provided to investigate the dynamics of EEG-ms and to assess temporal dependencies between MSs.

The present analysis aimed to further explore possible associations among the EEG-ms dynamic patterns and categorical Diagnostic and Statistical Manual of Mental Disorders-5 (DSM-5) MA diagnoses, as well as dimensional MA symptoms consistent with the National Institute of Mental Health's Research Domain Criteria (RDoc). The latter focused on both general EEG-ms properties and temporal associations within EEG-ms occurrence sequence and temporal dynamics. As the EEG-ms relates to intrinsic brain functional networks that are active at rest, it was hypothesized that there should be significant differences in EEG-ms dynamics between MA and HC.

3.2 Methods

3.2.1 Participants

For this Chapter, EEG and fMRI datasets are composed of 52 HC subjects (28 females) and 61 unmedicated MA subjects (38 females). Please refer to **Chapter 1**, **Section 1.7** and **Table A1** in **Appendix A** for detailed information about the dataset. The self-report questionnaires are presented in **Appendix A**.

3.2.2 EEG Data Acquisition

Please refer to **Section 1.8** in **Chapter 1** for detailed information about data acquisition. This chapter includes EEG only data collected from 113 subjects during resting EEG-fMRI testing for 8 min. Participants were instructed to relax, keep their eyes open, and fixate their eyes on a cross displayed on the fMRI stimulus projection screen.

3.2.3 EEG Data Preprocessing

The following preprocessing steps were performed in BrainVision Analyzer 2 software, as described in [84]. In short, MRI imaging artifacts within the EEG signal were reduced using the average artifact subtraction (AAS) method [85], and EEG signals were down-sampled to 250 Hz. Next, band-rejection filters (1 Hz bandwidth) were used to remove fMRI slice selection fundamental frequency (19.5 Hz) and its harmonics, mechanical vibration noise (26 Hz), and AC power line noise (60 Hz). Then, a bandpass filter from 0.1 to 80 Hz (48 dB/octave) was used. BCG artifacts also were removed using AAS [86]. ICA Infomax algorithm [87] implemented in Analyzer 2 was applied for EEG signal decomposition. The topographic map, power spectrum density, time course signal,

energy value, and kurtosis value were used for detecting and removing artifactual ICs, including residual BCG and imaging, ocular, and muscle artifacts. Finally, the EEG signal was reconstructed using back-projection (i.e., inverse ICA) after selecting ICs related to neural activities. Please see **Algorithm 1** below for detailed information about the preprocessing pipeline.

Algorithm 1: EEG preprocessing pipeline

Input $\boldsymbol{x}$. 31-channel raw EEG time series + single-channel ECG time series sampled at 5000 S/s.

Output. $\boldsymbol{y}$: corrected 31-channel EEG time series after artifact removal sampled at 250 S/s

Procedures. Artifact removal

1 $\boldsymbol{T_{image}}$**:** generate a template for imaging artifact for each EEG and ECG channel using the fMRI slice acquisition markers.

2 $\boldsymbol{y_1}$**:** remove MRI imaging artifacts by subtracting the $\boldsymbol{T_{image}}$ from **x**: $\boldsymbol{y_1 = x - T_{image}}$

3 $\boldsymbol{y_2}$**:** down-sample $\boldsymbol{y_1}$ to 250 Hz.

4 $\boldsymbol{y_3}$**:** bandstop filter with 1 Hz bandwidth for removing fMRI slice selection fundamental frequency (19.5 Hz) and its harmonics (39 Hz, 58.5 Hz, 78 Hz), mechanical vibration noise (26 Hz), and AC power line noise (60 Hz).

5 $\boldsymbol{y_4}$**:** bandpass filter from 0.1 to 80 Hz (48 dB/octave).

6 **R:** cardiac cycle determination using ECG channel.

7 $\boldsymbol{T_{BCG}}$**:** Generate a template for BCG artifact for each EEG channel using the $\boldsymbol{R}$.

8 $\boldsymbol{y_5}$**:** Remove BCG artifacts by subtracting the $\boldsymbol{T_{BCG}}$ from $\boldsymbol{y_4}$: $\boldsymbol{y_5 = y_4 - T_{BCG}}$

---

9 $\boldsymbol{y_6}$**:** Remove ECG channel. $\boldsymbol{y_6}$=$\boldsymbol{y_5}$**[1:31]**

10 A, S: Run ICA Infomax algorithm to decompose independent components (ICs): $\boldsymbol{y_6 = AS}$, where $\boldsymbol{A}$ is the mixing matrix and $\boldsymbol{S}$ is the ICs time series.

11 $\boldsymbol{T_{map}, P, K}$**:** Extract ICs features, including topographic map ($\boldsymbol{T_{map}}$), power spectrum density ($\boldsymbol{P}$) using equation 3.1, and kurtosis ($\boldsymbol{K}$) using equation 3.2.

12 $\boldsymbol{A'}$**:** Determine ICs associated with artifacts using ICA with artifacts that were selected and the column associated with those components that were substituted with zero.

13 $\boldsymbol{y}$**:** EEG signal was reconstructed using back-projection (i.e., inverse ICA) after selecting ICs related to neural activities. $\boldsymbol{y = A'S}$

3.2.4 Summary of EEG-ms Analysis Summary

The typical spatially independent EEG-ms analysis described in **Chapter 2** was conducted. In this section, we specify the parameters used to produce the results in this chapter. EEG was referenced using average-reference [56]. The number of desired MSs was set to k=4. The following steps were required before running the clustering algorithm: first, the GFP for each subject was calculated from band-passed filtered EEG data between 2 and 20Hz (using finite impulse response (FIR) with heuristically estimated transition band implemented with pop_eegfiltnew from EEGLAB [88]) as suggested in several EEG-ms studies [56]. GFP peaks were then identified after smoothing the data with a Gaussian-weighted moving average of 5-time points. Finally, to offer a higher level

of accuracy, we randomly selected up to n=10000 peaks and extracted the corresponding EEG points for later analysis. The selected EEG points were then submitted to the AAHC algorithm to identify the MSs with k=4. Next, the group means of EEG-ms (MA and HC) were computed by first sorting individual EEG-ms and then finding the common topography across all subjects. Next, individual EEG datasets were fit-back using the MA and HC group mean topographies. Finally, we extracted the following EEG-ms characteristics from each subject: average duration, the frequency of occurrence, and transition probabilities. Also, we conducted a theoretical information analysis described below to examine the temporal dynamics of EEG-ms.

3.2.5 Information Theoretical Analysis

Studying the dynamic behavior and the temporal dependencies of EEG-ms sequence may carry useful information that embodies differences in information flow between MA and HC groups. To do so, a new set of features introduced by von Wegner, et al. [83] was adopted. The approach relies on handling the spatially independent EEG-ms as discrete stochastic processes and examines the temporal dependencies in EEG-ms sequences. To elaborate on the set of utilized features, let us assume a random variable X_t that represents the state of MS at time point t. The X_t can take one of the possible labels $S_i \in [A, B, C, D]$, such that $P(X_t = S_i)$ represents the distribution of the MSs labels across the sequence of EEG-ms. The probability of transition between two states is given as $T_{ij} = P\left(X_{t+1} = S_j | X_t = S_i\right)$, and the transition matrix is denoted as T.

Herein, the low-order Markovianity of order 0, 1, and 2 was assessed. That is, EEG-ms were tested to see whether the transition of MSs relied on only the current state (order

0; $P(X_{t+1}) = P(X_{t+1}|X_t)$), the previous state (order 1; $P(X_{t+1}|X_t, X_{t-1}) = P(X_{t+1}|X_t)$), or the two previous states (order 2;$P(X_{t+1}|X_t, X_{t-1}, X_{t-2}) = P(X_{t+1}|X_t, X_{t-1})$). Transition matrix T was tested to determine whether it is stationary by first dividing the data into B overlapping blocks of length L. Then, the transition matrix for each block was assessed against the overall transition matrix. Furthermore, this matrix was tested against the symmetry property (i.e., $P(X_{t+1} = S_j|X_t = S_i) =, P(X_{t+1} = S_i|X_t = S_j)$). Finally, the time-lagged mutual information (i.e., autoinformation, AIF) was computed for the global sequence of EEG-ms, as well as for individual MSs. AIF examines the amount of information that $X_{t+\tau}$ has about X_t, with τ indicated as the desired time lag. The higher the value of AIF, the more shared information is carried by $X_{t+\tau}$ about X_t.

3.3 **Results**

First, we examined the EEG-ms topographies for MA and HC groups. **Figure 3-1** shows the four canonical EEG-ms classes for both groups. Similar EEG-ms topography templates were found for both groups (i.e., MS A through D) and were similar to those obtained by previous work [56]. The performance of the EEG-ms segmentation algorithm is reported in terms of the explained variance, which estimates the portion of EEG point topography that can be explained by the four MSs [89]. The explained variance in the case reported in this work was 82 % ± 0.02 % for HC and 82 %± 0.01 % for MA.

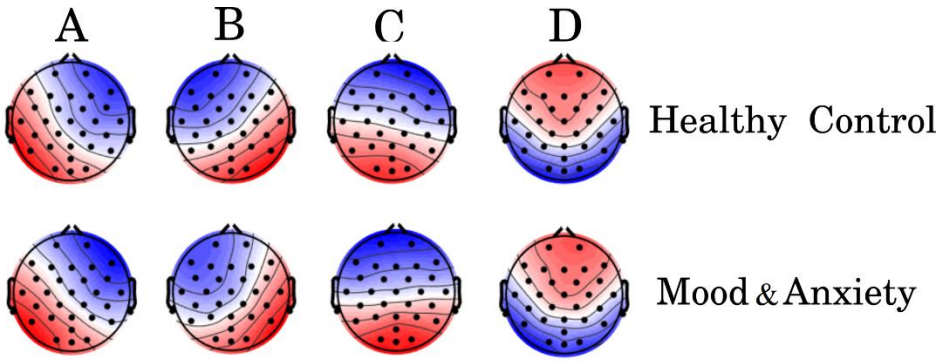


Figure 3-1: EEG-ms topographies for both groups—HC group top row, MA group lower row. The obtained EEG-ms topologies are similar to those reported previously in the literature.

Second, the average duration and occurrence frequency were investigated for both groups using independent sample t-tests. **Figure 3-2** shows the average duration for each MS. The p-values for the t-test between each MS were 0.12, 0.04, 0.02, and 0.24 for MS A, B, C, and D, respectively. After correcting for multiple comparisons using Bonferroni-Holm, the adjusted p-values were 0.23, 0.13, 0.09, and 0.24 for A, B, C, and D, respectively.

Similarly, the occurrence of each MS per second was computed for both groups (See **Figure 3-3**). Results did not reveal any significant difference between groups.

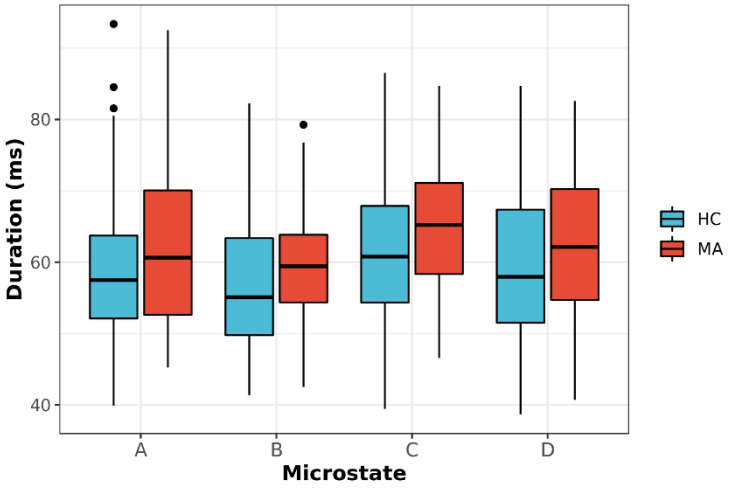


Figure 3-2: Average duration for EEG-ms classes (A-D) for MA and HC groups (p-value corrected for multiple comparisons using Bonferroni-Holm). Results revealed a trend towards significance for MS-C with p=0.09.

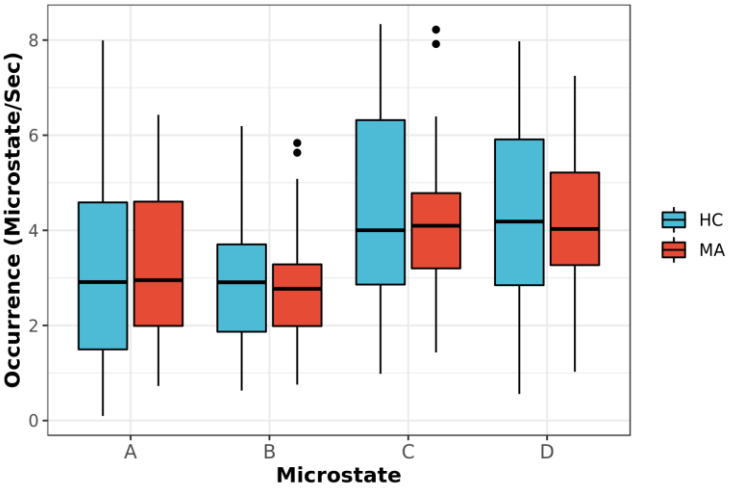


Figure 3-3: Occurrence frequency of EEG-ms classes (A-D) for both MA and HC groups. For each EEG-ms class, no statistically significant difference among the two groups was found.

Next, the model of transition among MSs for both groups was investigated and depicted in **Figure 3-4A**. Transition probabilities appear to have a normal distribution after checking and using Q-Q and density plots [90]. The statistical analysis of the transition probabilities of groups using independent samples t-tests unraveled a significant difference (i.e., Bonferroni-Holm corrected, p-value of significance was set to 0.05 [91]) between HC and MA in four transition probabilities (TP): from MS-B to MS-D: TP (B→D); D to B: TP (D → B); A to D: TP (A→D); and B to C: TP (B→C). The statistical analysis for the significant connections was reported in terms of the t-test p-value (p) and Cohen's d (d) effect size, as follows: TP (B→D): $t(111)=2.69$, $p=0.045$, $d=0.51$; TP (D→B): $t(111)=3.87$, $p=0.002$, $d=0.73$; TP (B→C): $t(111)=-3.05$, $p=.003$, $d=-0.58$; and TP (A→D); $t(111)=-2.88$, $p=0.045$, $d=-0.54$. **Figure 3-4B** highlights the transition

probabilities that show a statistically significant difference across groups and the direction of change.

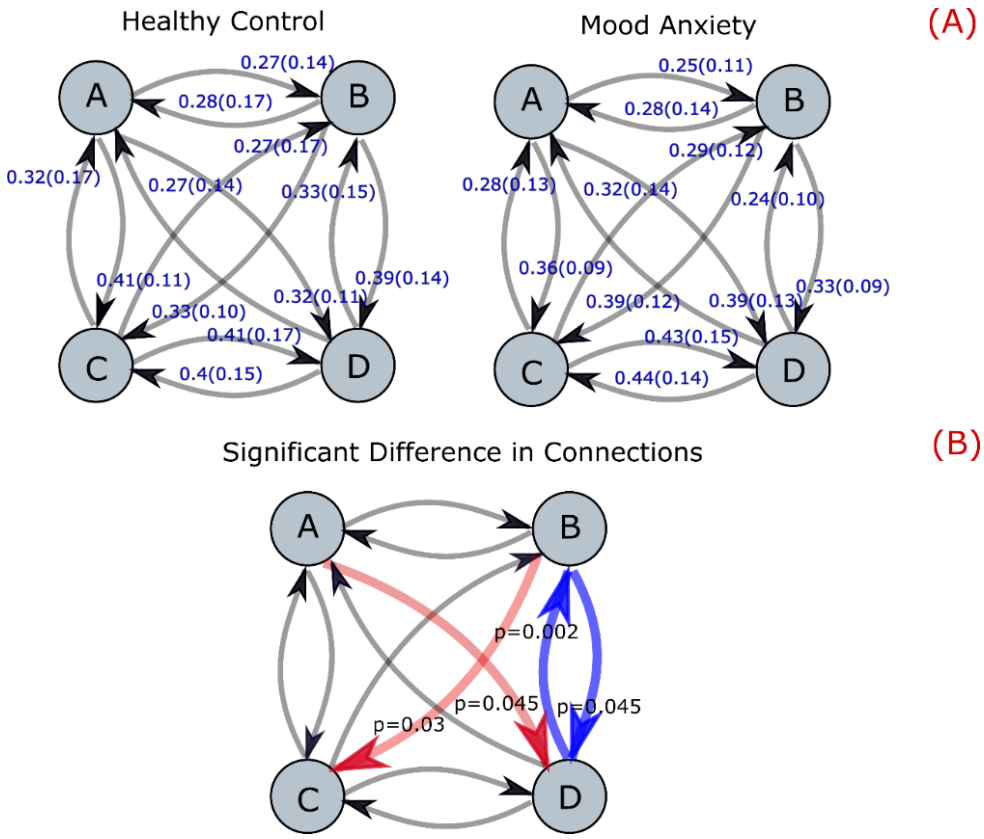


Figure 3-4: Transition probabilities for MA and HC groups (A); and (B) represents connections with the statistically significant difference between two groups—red and blue arrows indicate the direction of the changes in the transition probabilities (red represent an increase, while blue represent a decrease for MA compared to HC). p-values corrected for multiple comparisons using Bonferroni-Holm. The level of significance was set to $p<0.05$.

Associations between these transition probabilities and the symptoms (e.g., PHQ-9, RSS, STAI-Trait, STAI-State, PROMIS-Depress, and PROMIS-Anxiety scores; See **Appendix A** for more information about the clinical assessments) were investigated in Error! Not a valid bookmark self-reference. and **Table 3-2**.

Table 3-1: Correlation results among connections B to C and A to D and subjects' assessment measures. Correlation was estimated after combing both groups (n.s.: not a significant).

	TP (B → C)		TP (A→ D)	
	r	**p**	**r**	**p**
PHQ	0.251	0.008	0.253	0.008
RRS	0.290	0.002	0.284	0.003
STAI_State	0.313	0.001	0.171	n.s.
STAI_Trait	0.260	0.006	0.238	0.012
PROMIS_Anxiety	0.216	0.023	0.261	0.006
PROMIS_Depress	0.233	0.014	0.232	0.015

Table 3-2: Correlation results among connections B to D and D to B and subjects' assessment measures. Correlation was estimated after combing both groups (n.s.: not a significant).

	TP (B → D)		TP (D → B)	
	r	**p**	**r**	**p**
PHQ	-0.205	0.032	-0.267	0.005
RRS	-0.133	n.s.	-0.363	0.001
STAI_State	-0.245	0.010	-0.333	0.001
STAI_Trait	-0.182	n.s.	-0.317	0.001
PROMIS_Anxiety	-0.122	n.s.	-0.360	0.001
PROMIS_Depress	-0.149	n.s.	-0.277	0.003

Furthermore, the EEG-ms temporal dynamic within EEG-ms sequences was investigated. For both groups, the symmetry property of transition matrices was assessed

and tested for Markovianity of order 0, 1, and 2 properties (**Error! Not a valid bookmark self-reference.**), as described in the information theoretical analysis section. The two-sample t-test yielded a *p*-value representing the null-hypothesis that subject's EEG-ms sequence exhibits a low-order Markovian property (e.g., for an order of 0, the transition probability relied on only the current MS) or symmetrical transition matrix (e.g., the likelihood of switching from microstate X to Y is not statistically different from the likelihood of switching from Y to X). All tests were conducted at alpha = 0.01 and $p < 0.05$. **Error! Not a valid bookmark self-reference.** reports the testing results as the ratio of how many subjects within each group showed statistically significant hypothesis (e.g., the EEG-ms sequence exhibits a Markovian property of order 0).

Table 3-3: Markovian property and symmetry assessment for both groups.

	Order 0	**Order 1**	**Order 2**	**Symmetry**
HC	0%	0%	0%	58%
MA	0%	0%	0%	65%

The reported transition probabilities in **Figure 3-4** were estimated for the entire recording of EEG (e.g., 8 min). The stationary of the transition matrices was further probed over a shorter period (i.e., whether the transition matrices remain constant over a short duration). Specifically, the stationarity of the transition matrices was computed at period lengths of 2 to 40 secs, and the ratio of subjects who had statistically significant non-stationary matrices at each period were reported (**Figure 3-5**).

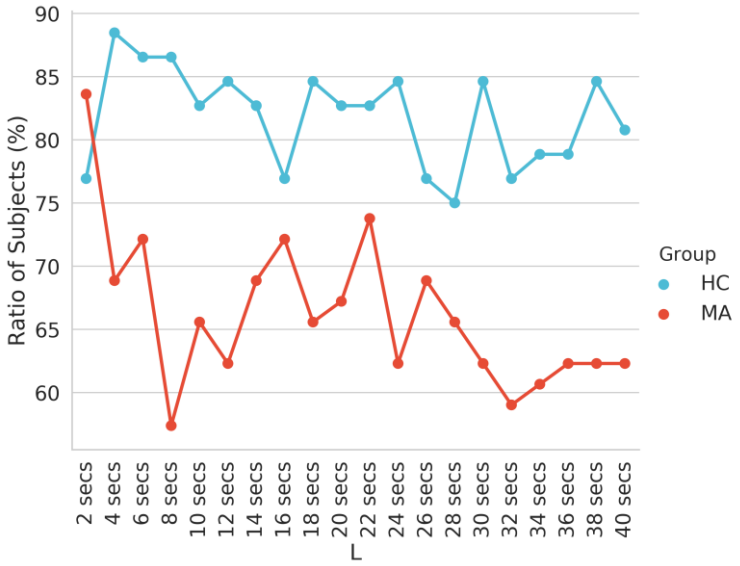


Figure 3-5: The ratio of subjects with non-stationary transition matrices ($p< 0.05$) of EEG-ms evaluated at different block lengths.

Finally, the AIF to examine the temporal dependencies in EEG-ms was computed. AIF estimates the amount of information that the appearance of MSs carries, given previous information (i.e., previous MSs). In other words, it evaluates the memory effect in MSs' sequence over the shorter duration; the higher the value, the more similar the MS sequence given the past. By comparing AIF among groups, one can tell whether a certain group has a higher tendency to evoke the same patterns of MS sequences over and over. **Figure 3-6** shows the AIF plot as a function of different time-lags ($\tau \leq 4000$ ms) for both MA and HC groups. The individual contribution to the overall AIF graph is presented in **Figure 3-7.**

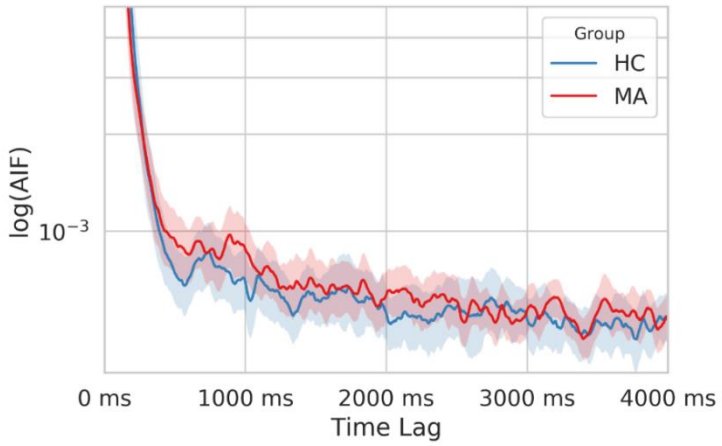


Figure 3-6: The semi-log time-lagged mutual information plot for the MA and HC groups at different time lags. The shaded area represents the 95% confidence intervals for each group.

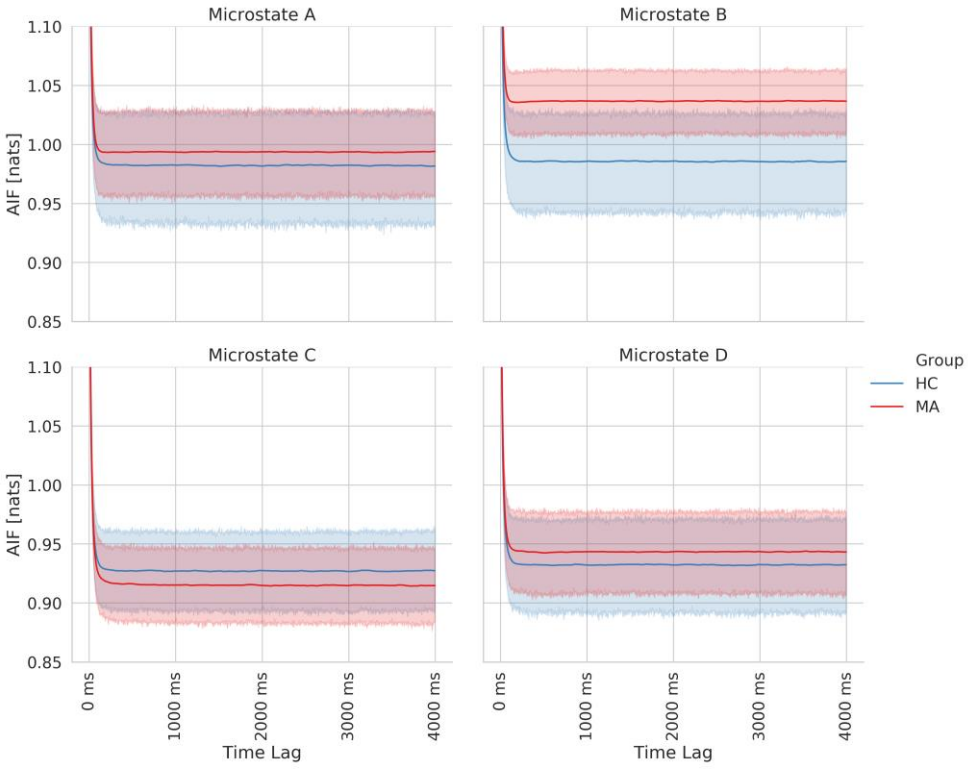


Figure 3-7: Time-lagged mutual information plots for each class of EEG-ms averaged across subjects of each group. The shaded area represents the 95% confidence intervals for each group.

3.4 **Discussion**

This chapter details deriving and dissecting the EEG-ms from large cohorts of MA and HC individuals. Four canonical EEG-ms classes (A through D) in these individuals were found, which confirms a successful replication of previously reported topographies [56]. Notably, a specific dissimilarity in the topographies of EEG-ms between HC and MA groups was not found (**Figure 3-1**). That is, EEG-ms topographies were stable and robust regardless of the presence of MA symptoms. Given that EEG-ms represent spontaneous, synchronized in time, and significant spatial-scale cortical neuronal activities [54, 56], the lack of differences between participant cohorts suggests that there are no major structural cortical changes among groups [92-94]. If EEG-ms topography exhibited significant changes between HC and MA cohorts, then that might indicate substantial structural changes and alterations of the brain. The lack of topographical differences among study cohorts supports the notion that mental disorders are more manifested in disruption of brain network dynamics rather than structural changes. Taken together, the similarity in EEG-ms topographies between HC and MA cohorts may suggest that the effect of depression and anxiety is far more pronounced at the level of dynamic functional connectivity of the brain, rather than at the level of structural abnormalities of the brain.

Next, EEG-ms average duration and occurrence frequency in the cohorts were appraised, as these properties have been used frequently in the literature to differentiate groups [22]. The spatially independent EEG-ms analysis revealed a trend towards significant difference for an average duration of MS-C ($p<0.09$ corrected for multiple comparisons using the Bonferroni-Holm method). Results did not reveal any other

significant difference for average duration or occurrence frequency properties among groups. Furthermore, transition probabilities among different MS classes were analyzed for both groups. The analysis showed significant differences in transition probabilities in four out of 12 connections in the transition matrices across groups. Specifically, the TP (D→B) and TP (B→D) showed a statistically significant difference between groups ($p < 0.05$, Bonferroni-Holm corrected), where MA subjects have a lower transition probability between TP (B→D) and TP (D→B) when compared with HC subjects. That is, MA subjects tend to have a lower switching frequency between MS-B and MS-D when compared with HC subjects. Also, results revealed a significant difference in transition probabilities for TP(A→D) and TP(B→C) in one direction ($p < 0.05$, Bonferroni-Holm corrected), where MA subjects tend to have a higher transition from A→ D and B→C. Such disturbances in transition between MSs have been reported for subjects with other mental disorders like schizophrenia [69] and frontotemporal dementia [70] when using traditional EEG-ms analysis.

To understand the results, outstanding works that investigated the association between EEG-ms and RSNs by using simultaneous EEG-fMRI were consulted. Research suggested a strong association between EEG-ms and RSNs [22-24, 58]. RSNs are set of networks that are intrinsically active during task-negative state (i.e., when there is no task) and can be observed as changes in the BOLD signal. **Chapter 6** offers in-depth analysis for the association between EEG-ms and brain regions. For interpreting the results in this chapter, consulting Britz, et al. [24] is recommended, since the authors utilized the same conventional approach in extracting EEG-ms as used in this work. Please refer to **Table A2** and **Table A3** in Appendix A for detailed information about the association between

each MS and RSNs. Based on Britz, et al. [24], MS-B was shown to be associated with the visual network (VN), while MS-D was related to the dorsal attention network (DAN). The associated networks with MSs were similar to the RSNs found in other works [1, 2]. DAN is often considered as an activity-modulating network in the VN, especially the frontoparietal areas [95]. The low transition probabilities between MS-B and MS-D in the MA group indicates less frequent transitions between VN and DAN. The previous study showed a modulatory role of DAN with VN [95], and the impaired modulatory role of DAN might cause less frequent transitions among MA subjects. Several studies reported an alteration in FC between the two networks for subjects with PTSD [96-99], stress [100], anxiety [101], and social anxiety disorder [102]. Furthermore, DAN appears to exhibit an FC alteration associated with depression, as reported in multiple meta-analyses [103-105] and in a recent study [106]. Thus, lower transition probability between B and D may indicate aberrant functionalities between DAN and VN.

In addition, MA subjects exhibit a higher transition between MSs (B→C) in one direction. Notably, MA subjects spend on average more time in microstate C than HC ones (**Figure 3-2**). MS-C has been shown to be correlated with the brain regions responsible for the self-referential mental activity (e.g., parts of DMN). An increase in the self-referential processes in DMN has been shown to be closely related to depression [107, 108]. Along with an increase in the average duration of MS-C and the higher transition from MS-B to MS-C, the result may be explained by an increase in the self-referential activity for MA subjects with engaging VN in recalling visual memories, although more research is warranted to determine whether the valence of these memories

is predominantly negative, thereby contributing to aversive emotional processing in individuals with depression and/or anxiety.

Similarly, MA subjects have a higher TP (A→D) in one direction. Brain regions associated with MS-A have been shown to be involved in the auditory-phonological system, especially the bilateral superior temporal cortex. Such alteration in this RSN has been reported in meta-analyses for subjects with depression [103-105]. Additionally, the association between the four significant transition probabilities and other clinical assessments was studied (Associations between these transition probabilities and the symptoms (e.g., PHQ-9, RSS, STAI-Trait, STAI-State, PROMIS-Depress, and PROMIS-Anxiety scores; See **Appendix A** for more information about the clinical assessments) were investigated in Error! Not a valid bookmark self-reference. and **Table 3-2**.

Table 3-1 and **Table 3-2**). The results showed a relative correlation between transition probabilities after combining both groups, but not when considering groups independently. However, the transition probabilities showed different patterns based on the group. To further investigate the interaction between groups and symptoms, a GLM was designed to study the interaction between groups and symptoms after controlling for age and gender (**Table A4** in **Appendix A**). The results suggest a significant interaction between groups and symptoms in connections B→D and D→B for PHQ, STAI (State), STAI (Trait), and PROMIS (Anxiety Total Score). These results may imply that HC and MA groups behave differently based on the symptoms, but the relation between symptoms and transition probabilities within groups is more complicated than can be explained by one connection.

While transition matrices unravel the overall behavior of MSs, AIF characteristics of EEG-ms may encompass an insight into the dynamics of EEG-ms. To do so, the approach introduced by von Wegner, et al. [83] was adopted. Results were in line with their results that there is a short-term memory effect in the EEG-ms sequence, as shown in Associations between these transition probabilities and the symptoms (e.g., PHQ-9, RSS, STAI-Trait, STAI-State, PROMIS-Depress, and PROMIS-Anxiety scores; See **Appendix A** for more information about the clinical assessments) were investigated in Error! Not a valid bookmark self-reference. and **Table 3-2**.

Table 3-1. For both groups, EEG-ms do not exhibit any Markovian property of order 0, 1, or 2 (i.e., the appearance of next MS [in time] does not rely merely on the current state, previous state, or two previous MSs). If MS sequence exhibits any low Markovian order, then one can conclude that MSs' appearance relies only on the past—depending on the order. This demonstrates that MSs embody the underlying neural activities and are closely associated with brain activity [25]. Furthermore, non-Markovian properties show that the sequence has memory.

In addition, the analysis in this work suggests a difference in the information flow manifested in changes of the symmetry and stationary of transition matrices—taken at different periods, besides AIF contents between HC and MA groups. Specifically, the MA group tends to have a higher ratio of subjects with symmetrical (Furthermore, the EEG-ms temporal dynamic within EEG-ms sequences was investigated. For both groups, the symmetry property of transition matrices was assessed and tested for Markovianity of order 0, 1, and 2 properties (**Error! Not a valid bookmark self-reference.**), as described in the information theoretical analysis section. The two-sample t-test yielded a *p*-value

representing the null-hypothesis that subject's EEG-ms sequence exhibits a low-order Markovian property (e.g., for an order of 0, the transition probability relied on only the current MS) or symmetrical transition matrix (e.g., the likelihood of switching from microstate X to Y is not statistically different from the likelihood of switching from Y to X). All tests were conducted at alpha = 0.01 and $p < 0.05$. **Error! Not a valid bookmark self-reference.** reports the testing results as the ratio of how many subjects within each group showed statistically significant hypothesis (e.g., the EEG-ms sequence exhibits a Markovian property of order 0).

Table 3-3) and stationary transition matrices (**Figure 3-5**) when compared with HC subjects. This may be interpreted as less flexibility and dynamicity of brain connectivity for MA subjects, where similar patterns of brain activations may be evoked frequently (e.g., ruminative or self-referential thoughts). Likewise, the MA group has a relatively higher overall AIF content when compared with the HC group (**Figure 3-6**) driven by MS-B (**Figure 3-7**). Hence, this might be explained as an increase in the overall temporal dependency in MA subjects and a more regular appearance for MS-B (associated with VN).

Given these points, MA subjects exhibit a systematic difference in the way of activating their brain regions reflected by changes in transition probabilities, duration of MS-C, and temporal dependencies of MSs.

3.5 Limitations

The present analysis has provided several aspects of analyzing MA when compared with HC. We have shown a significant transition probability difference between groups. However, the underlying neurophysiological mechanism of transition probabilities of MSs is still not clear. The provided interpretations of EEG-ms dynamics properties and their associations with brain networks relied on previous studies that found a correlation between EEG-ms time series and different brain regions to interpret the results. In addition, the study cohort is very heterogeneous, thus understanding specific network abnormalities as reflected by EEG-ms within the MA cohort should warrant future studies with an even larger number of subjects to better characterize individual differences and subtypes of the MA disorder cohort. Finally, the AIF approach for analyzing the EEG-ms temporal dynamics revealed a group difference among MA and HC cohorts; however, results need further exploration to provide a more comprehensive mechanistic interpretation.

3.6 Conclusions

This chapter delved into the spatially independent EEG-ms in a large cohort of MA and HC individuals. Previously reported studies were replicated and four EEG-ms classes (A through D) showed no differences among MA and HC individuals. This suggests a lack of significant structural cortical abnormalities among the groups, which would otherwise affect the EEG-ms topographies. Several EEG-ms characteristics between groups were investigated in terms of average duration, frequency of occurrence, and transition matrices. In addition, various autoinformation properties between groups

were extracted to evaluate the temporal dependences of MSs between subjects. Results revealed an alteration in EEG-ms transitions probabilities among MSs; in B → D, D →B, A →D and B →C transitions. In addition, testing the temporal dependencies unveiled an alteration in information flow between groups in different properties. Such properties can be used as biomarkers for MA and a basis for future interventions.

Chapter 4 : Predicting Age from EEG Using Unbiased Machine Learning Framework

(All the presented results in this chapter are reproduced and adapted from: *Al Zoubi, Obada, et al. "Predicting Age From Brain EEG Signals—A Machine Learning Approach." Frontiers in aging neuroscience 10 (2018): 184.)*

4.1 Introduction

In **Chapter 3**, EEG-ms features were harnessed to study subjects with MA. This chapter utilizes a different set of static features to study the aging of the brain. Brain age gap estimates (BrainAGE) is defined as the difference between the estimated age and the chronological age of the individual. BrainAGE has been investigated primarily using structural and functional MRI and diffusion tensor imaging (DTI). However, EEG signals, particularly in combination with ML approaches, have not been commonly utilized and validated for human age prediction and the determination of BrainAGE. This work reported in this chapter investigated whether age-related changes are affecting brain EEG signals and whether chronological age can be predicted with an extensive feature extraction-approach of EEG signal properties. The goal of this investigation was to provide a rigorous framework for obtaining BrainAGE estimates from EEG using comprehensive feature extraction and ML.

Brain changes due to age have been studied for decades (e.g., [109-111]) and more recently using genetics [112]. The term BrainAGE (i.e., the difference between predicted age and chronological age) was introduced to examine and capture any disease-related

deviations from natural aging by comparing BrainAGE estimates in a particular disease group to a HC group. Structural MRI has been widely used to build predictive models for age by utilizing white matter (WM) and gray matter (GM) properties. Authors in [113] employed T1-weighted (T1w) MRI structural images to establish a framework—using a kernel method for regression—for automatically and efficiently estimating the age of healthy individuals. This framework proved to be a reliable, scanner-independent, and efficient method for age estimation, yielding a correlation of r=0.92 between the estimated and the real age in the test samples, with a mean absolute error of only 5 years. Similarly, [114] used deep learning (DL) to study BrainAGE using both pre-processed and raw T1w MRI images. Their approach predicted age with minimal effort by achieving a correlation between age and predicted age: r= 0.96, with an error of 4.16 years. Using similar structural images, [115] obtained $R^2 = 0.77$ from a large sample of healthy subjects (n=3144) by training features from various anatomical brain regions. Researchers in [116] studied age-related changes in water self-diffusion in cerebral WM using DTI, revealing that WM changes with age in multiple brain regions, including the corpus callosum, prefrontal cortex, internal capsule, hippocampal complex, and the putamen. fMRI has also been used to predict age alone or combined with other imaging approaches. For instance, [117] researchers were able to explain up to 55% of their sample variance from the fMRI FC data. Likewise, [118] related the developmental changes in the amplitude of low-frequency spontaneous fluctuations in resting-state fMRI to age. They reported an error of 4.6 years between chronological age and predicted age.

More recently, [119] utilized cortical anatomy and whole-brain FC for predicting brain-based age, achieving an error of 4.29 years. Several BrainAGE studies revealed

changes and differences among clinical groups. For example, BrainAGE estimations in schizophrenia patients were attributed to accelerated aging when compared to healthy comparison subjects, as well as individuals with bipolar disorder [120]. In addition, individuals diagnosed with refractory epilepsy had a higher predicted age than healthy subjects [114].

Herein, we focus on studying BrainAGE using EEG signals. Several studies have demonstrated that EEG features like EEG rhythmic activity (e.g. delta, theta, alpha-1, alpha-2, beta, and gamma) changes as a function of age (Ashburner [121], Clarke, et al. [122], Cragg, et al. [123], Marshall, et al. [124], Matthis, et al. [125]). For instance, [126] found theta band showed an increase in power spectra with age, while delta exhibited a decrease for healthy children between 4 to 17 years. Analyzing the coherence of EEG during a resting-state recording revealed that elderly subjects had a lower coherence than younger healthy subjects for delta, theta, alpha-3, beta-1, and beta-2 [127]. Relative beta power was positively correlated with age for older subjects [128]. In contrast, alpha reactivity decreased and showed a negative correlation with age in the older group when they were performing mental tasks, as opposed to resting [128]. Furthermore, theta power was shown to increase from resting to arithmetic task processing for the younger group while decreasing for the older group [129]. Power in delta and beta-3 bands increased from resting to arithmetic task processing, while alpha power decreased [129].

A more recent study used four channels of EEG recording to investigate age-related changes in EEG power from thousands of subjects throughout adulthood [130]. Researchers' findings showed an overall age-related shift in band power from lower to a higher frequency and a gradual slowing of the peak alpha frequency with increasing age.

Furthermore, studying the source of these cortical rhythms suggested that occipital delta and posterior cortical alpha rhythms decrease in magnitude during physiological aging with both linear and nonlinear trends [131].

Age prediction from EEG was studied in [132], where authors used FC features from EEG to predict age from 94 healthy subjects. Their results showed an accuracy of R^2=0.60 for eyes-open and R^2=0.48 for eyes-closed.

The influence of diseases on EEG features has been investigated elsewhere. For instance, [133] used the mean EEG power spectrum to study group differences between multi-infract dementia (MID) and dementia of Alzheimer's disease (AD), and then compared results with a healthy comparison group. The MID group showed a significant increase of theta activity in occipital regions and decrease in alpha activity—a pattern not evident in the other two groups. An abnormality in cortical neural synchronization for subjects was observed in subjects with mild cognitive impairment due to AD (ADMCI) and to Parkinson Disease (PDMCI) in delta and alpha [134]. Differentiating subjects with AD from healthy ones was studied in [134]. Authors reported 70% accuracy using the power and FC of cortical sources, which was later improved to 77% using artificial neural network computational methods [135]. This chapter proposes a robust and rigorous framework to predict BrainAGE using different features of EEG signals recorded during fMRI in a sample of N=468 individuals. First, an open-source EEG feature extraction software was extended in MATLAB [136] to provide a feature representation of individual subjects. Then, a set of ML methods was applied to predict age from features.

Table 4-1 provides a summary of studies that specifically reported age prediction performance from brain imaging data.

This chapter proposes a robust and rigorous framework to predict BrainAGE using different features of EEG signals recorded during fMRI in a sample of N=468 individuals. First, an open-source EEG feature extraction software was extended in MATLAB [136] to provide a feature representation of individual subjects. Then, a set of ML methods was applied to predict age from features.

Table 4-1: Summary of related work for predicting age from brain imaging data.

Work	**Data**	**# of Samples**	**Performance**
[113]	MRI	650	r=0.92, MAE =5 years
[114]	MRI	2001	r=0.96, MAE =4.16 years
[117]	fMRI	238	$R^{\wedge 2}$=0.55
[118]	fMRI	183	MAE =4.6 years
[115]	MRI	3144	$R^{\wedge 2}$=0.77
[132]	EEG	94	R^2=0.6 for eyes open R^2=0.48 for eyes closed
[119]	fMRI+sMRI	2354	MAE=4.29 years

*MAE=Mean Absolute Error

The data, results, and discussions included in this chapter were already published and are reproduced from [50].

4.2 Methods

4.2.1 Participants

Participants were selected from the first 500 subjects of the T-1000 [49] (Please refer to **Section 1.7** in **Chapter 1** for more information about the participants). The age histogram of participants is shown in **Figure B1** in **Appendix B**.

4.2.2 EEG Data Acquisition

Please refer to **Section 1.8** in **Chapter 1** for a detailed description of the EEG recording. Included EEG data was collected from only 468 subjects (mean age: 35 years, 297 females). One resting EEG-fMRI run was conducted for each subject, lasting 8 min. Participants were instructed to relax, keep their eyes open, and fixate on a cross.

4.2.3 EEG Data Preprocessing

Unlike the manual preprocessing of EEG data used in **Chapter 3**, an automatic EEG preprocessing was adopted for the work reported in this chapter due to the large number of subjects. In details for each scan, EEG data were preprocessed with an in-house script developed using MATLAB [137]. The script was designed to remove the MR gradient artifact and BCG artifacts from EEG data. Details about the preprocessing script are given as follow. The MR gradient artifact was first removed from the EEG data using optimal basis sets [85, 88, 138]. Then, the EEG data was band-pass filtered between 1 Hz and 70 Hz, down-sampled to 4 ms temporal resolution, and band-stop filtered (1 Hz bandwidth) at the harmonics of 19.5 Hz. This was the fMRI slice selection frequency for 39 slice acquisition in TR=2sec; for AC power line frequency (60 Hz); and for a 26 Hz

vibration artifact frequency. Then, the cardioballistic artifact was corrected using optimal basis sets subtraction [138], which requires the timing of the artifact cycle. In order to achieve a robust artifact cycle determination, the script determined the artifact cycle using the cardioballistic component directly from the EEG-fMRI data [139], which was extracted by ICA [87] and was automatically identified [137].

4.2.4 EEG Feature Extraction

Feature extraction is a quintessential phase in any EEG analysis that depends on finding common feature representation among EEG samples. The existing literature provides quite an extensive span of features extraction using a variety of signal processing approaches [140]. Choosing a feature extraction method relies on the applications of the prediction and the balance between interpretation and performance. For instance, advanced feature extraction methods can be used at the cost of interpretation, where such approaches have been shown to outperform typical approaches [132, 141]. For the case reported herein, BrainAGE emphasizes the interpretation and understanding of predictors, since the goal is to find those features that influence BrainAGE modeling. Thus, a similar set of features used by [136] was adopted, which extracted a wide range of commonly used features from EEG. However, this work takes an extensive approach to survey all features from all channels and bands without reducing features by averaging, as performed in [136]. Such a feature-extraction approach ensures a comprehensive survey of all possible EEG information to identify feasible predictors for age from brain data. Also, the types of features used in this work are commonly used in the literature to analyze EEG data. That is, the interpretation and replication of such features are less challenging than using uncommon features. However, the approach detailed herein

resulted in a relatively large number of features from EEG. Therefore, feature selection and suitable ML algorithms are needed to deduce which predictors account for the most variance in age. All features were extracted from each subject independently and arranged in one row/sample.

4.2.5 General Configuration

EEG bands of interest are [δ = .5–4; θ=4 –7; α =7–13; β=13–30; W=0.5–30] Hz using the bipolar montage of the EEG, where W denotes the entire frequency range of EEG. EEG time series was denoted as $x_i[n]$ with frequency bands of $i = \alpha,\ \beta,\ \theta,\ \gamma, W$, and n in each channel's index (i.e., total number of channels is N=31). Five types of features were selected: amplitude, range, spectral power, connectivity, and fractal dimension (FD). EEG recordings were divided from each subject into 60 sec, with a 50% overlap among epochs—14 epochs in all. **Figure 4-1** elaborates on the feature extraction process. For each channel, the signal was divided into m epochs, and then each epoch was filtered into corresponding frequency bands. Specific feature extraction was applied to each sub-segment yielding m values. Finally, channel-level feature was estimated for the corresponding frequency band as the average across all epochs. The process is slightly different for FD features, since features were estimated without filtering into frequency bands.

4.2.5.1 Amplitude Domain Features

Amplitude features characterize the statistical properties of the signal power A^i_{power} and the signal envelope E^i_{mean}. This was accomplished by calculating: i) mean, ii) standard deviation, ii) skewness, and iv) kurtosis for each channel across frequency

bands. The E_{mean}^{i} is calculated using the mean of the envelope $e[n]_i$, which is identified in complex notation as: $e_i[n] = |x_i[n] + jH\{x_i[n]\}|^2$, wherein H is the Hilbert transformation.

4.2.5.2 Range Domain EEG Features (rEEG)

Range features account for peak-to-peak voltage changes and characterize changes in the signal over time. To achieve this, each epoch was segmented into short-time portions, each with a window size of $w = 2\ sec$ and overlap of 50%. Then, for each segment, the corresponding peak-to-peak range was calculated. This produced samples from each epoch to estimate the mean, median, 5th and 95th percentiles, standard deviation, coefficient of variation, and the measure of symmetry.

4.2.5.3 Spectral Domain Features

Spectral features have been the most commonly used features for EEG. To extract these features, Welch periodogram was applied to estimate power spectral density (PSD) and Hamming window with a length of 2 secs and an overlap of 50%. The following spectral features were extracted: 1) power; 2) relative power; 3) entropy (using Wiener and Shannon methods); 4) edge frequency (the cut-off frequency at which encompasses 95% of spectral power); and 5) differences between consecutive short-time spectral estimations.

4.2.5.4 Connectivity Domain Features

The brain symmetry index (BSI) was calculated as the mean of PSD difference between the left and right hemispheres for each frequency band (K=δ, θ, α, β, γ).

Let a_i and b_i be the lower and upper-frequency limit of band$i$, the BSI for band i is:

$$C_{BSI}^{i} = \frac{1}{(b_i - a_i)} \sum_{k=a_i}^{b_i} \left| \frac{P_{left}[K] - P_{right}[K]}{P_{left}[K] + P_{right}[K]} \right| \tag{4.1}$$

where

$$P_{left}[K] = \frac{\sum_{m=1}^{n/2} P_m[K]}{n/2} \text{ and } P_{right}[K] = \frac{\sum_{m=\frac{M}{2}+1}^{M} P_m[K]}{n/2} \tag{4.2}$$

Also calculated was the median and lag of the maximum correlation coefficient of the Spearman correlation between envelopes of hemisphere-paired channels and coherence between channel pairs.

4.2.5.5 Fractal Dimension Domain Features

FD for the time series is a value that estimates to what extent the fractal pattern changes with respect to the scale at which it embeds. The Higuchi method was applied with $k = 6$ for each EEG channel to estimate FD. **Table 4-2** summarizes the extracted set of features from EEG data.

Table 4-2: The extracted features from EEG data.

Feature Group	Subset of features	Across Bands	Across channels	Number of features
Amplitude	Total power, mean, standard deviation, skewness, kurtosis, envelope mean and standard deviation	Yes	Yes	$6 \times 4 \times 31$
peak-to-peak	Mean, median, 5th and 95th percentiles, standard deviation, coefficient of variation, and measure of symmetry	Yes	Yes	$7 \times 4 \times 31$
Spectral power	Spectral power and relative power, spectral entropy (using Wiener and Shannon methods), spectral edge	Yes	Yes	$6 \times 4 \times 31$

	frequency (the cut-off frequency at which encompasses 95% of spectral power), and spectral differences between consecutive short-time spectral estimations			
Connectivity	Brain symmetry index, correlation, mean and maximum of frequency at which the maximum coherence is achieved	Yes	No	5×4
Fractal dimension	Fractal dimension	No	Yes	31

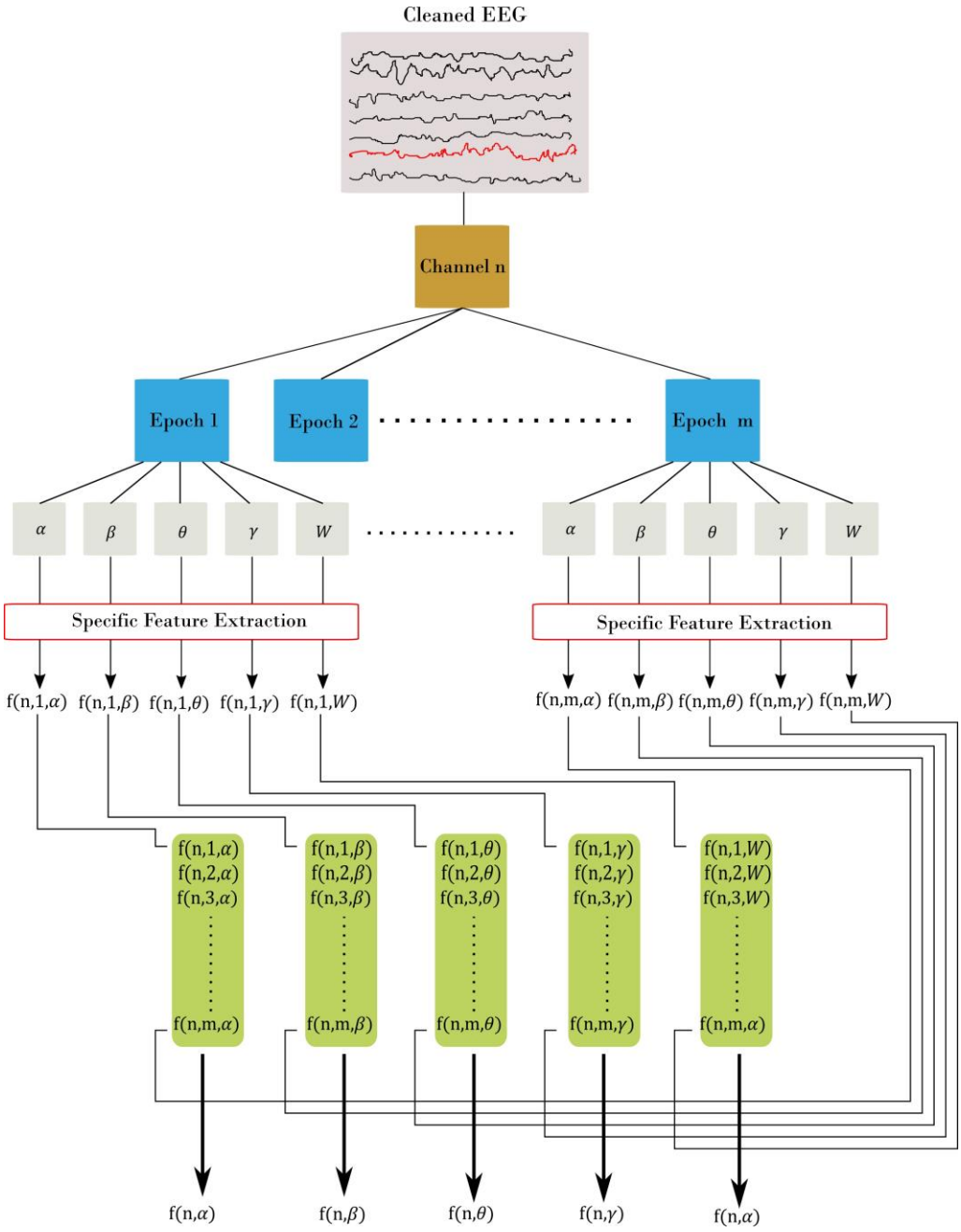


Figure 4-1: Feature extraction procedure. Each channel is divided into m epoch. From there, each epoch was filtered into α, β, θ, γ, and W frequency bands. Then, for each filtered epoch, the desired features were extracted. This resulted in m feature value from all epochs, which are then averaged to estimate the channel-level feature. In the figure, each feature is represented using three indices: f (channel, epoch, band) with channel= [1...N]; epoch= [1...m]; and band = [α, β, θ, γ, W]. The final out is a channel-level feature represented with two indices f (e.g., channel, band).

4.2.6 Feature Reduction

After feature extraction, features—either low in variation among subjects or highly correlated with other features using the "findCorrelation" function in the "caret" package [142], version "6.0-78"— were eliminated. "FindCorrelation" evaluates pair-wise correlation of features, and then finds the highest absolute pairwise correlation. Given that two features have a high correlation (r>=0.9 Pearson's correlation), "findCorrelation" eliminates the feature with the highest mean absolute correlation. It should be noted that other feature selection methods could be used to select the best features using the Nested-Cross-Validation (NCV) approach. However, the interpretation of such an approach could be challenging, because selected features from the inner loop of the NCV may vary across folds. In addition, using other feature selections should be applied within each loop of NCV, which increases computational overhead. Thus, removing correlated features provides a better way to select features in this case. **Figure B2** and **Figure B3** in **Appendix B** show the correlation matrices before and after removing correlated features.

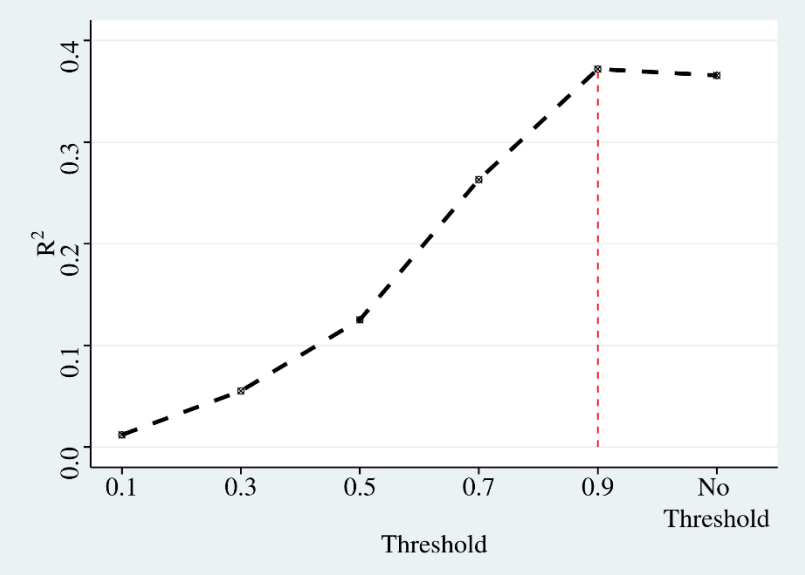


Figure 4-2: The effect of removing correlated features on prediction.

4.2.7 Machine Learning Methods

Selecting appropriate ML algorithms is a critical step for achieving robust BrainAGE estimation. Having represented each subject's features in one row, the final dataset dimension is $x = n \times m$, where $n = 468$ and $m = 863$. R package "caret" was used to perform a set of regression algorithms: elastic net (ENET), support vector regression (SVR), random forest (RF), extreme gradient boosting tree (XgbTree), and Gaussian process with polynomial kernel (gaussprPoly). The aim was to test different ML techniques and to provide a better estimation for age. First, ENET is a linear regression technique that uses L1 and L2 regularization to prevent overfitting. Second, SVR uses optimization to build the regression model, although specifically within a high dimensional version of the training data. In this case, a kernel with a radial basis function was used to project the data into high dimensional space. Third, RF is one of the most common ensemble techniques, as it performs subsampling for the feature space of

training data to build multiple weak learners. Thus, different models from the training data are produced and then averaged to minimize variance across models. Fourth, XgbTree utilizes a combination of ensemble learning, optimization, and regularization to build a generalized model from training data. Finally, gaussprPoly is a probabilistic approach to build a regression model by learning the distribution of the training data, given the response (age). Similar to the kernel function in SVR, gaussprPoly adopts a polynomial kernel to project data into high dimension space.

To provide an unbiased prediction for age, NCV was adopted in building age prediction models [143]. **Figure 4-3** depicts the NCV procedure consisting of two main loops: inner and outer. The inner loop is used to find the preferred parameters from the training set, while the outer loop is used to evaluate the preferred parameters on the testing set. To elaborate on the NCV, let the subscript refer to data and models from the inner loop of NCV, while the superscript represents those from the outer loop. A10-fold cross-validation (K_I=10) was used for the inner loop, and 10-fold cross-validation for the outer loop (K_O=10). The inner loop was used to estimate optimal parameters on training data (Tr^1) using a grid search and the one-standard error rule. Each inner loop consists of 5-repeat (R=5) for each method. The outer loop uses the best-obtained models to build a stack-ensemble model. Best models are represented by their optimal parameters θ_i^l, where i is the method index of the corresponding method M_i, and l refers to the fold l from the outer loop. This stacking ensemble helps to improve the stability of prediction by combining the prediction from other models (i.e., predictions from the three methods were combined by learning weights via a GLM). Specifically, the GLM was trained on the resampled predicted age from the inner loop (yTr_i^l), and then the GLM was used to

provide one weighted-average prediction in 10-fold cross-validation ($K_{Ens} = 10$). From there, the best stack-ensemble model (θ_{Ens}^{l}) was used to predict age for the testing set ($\widehat{YTs^{l}}$). That is, the prediction of age is calculated for the individual methods $yTr_i^l = predict(Tr^l, \theta_i)$, and then the weighted average is estimated for fold l.

$$\widehat{YTs^{l}} = predict([yTr_1^l, yTr_2^l, \dots, yTr_n^l],\ \theta_{Ens}^{l})$$

After iterating over all folds from the outer loop, a prediction for the age of the entire dataset can be built. In addition, the variable importance of predictors from the stacking ensemble models was estimated across the outer loop of NCV. Finally, the predicted age and age values were used to estimate the BrainAGE for the dataset. **Figure 4-4** shows the overall framework to estimate BrainAGE.

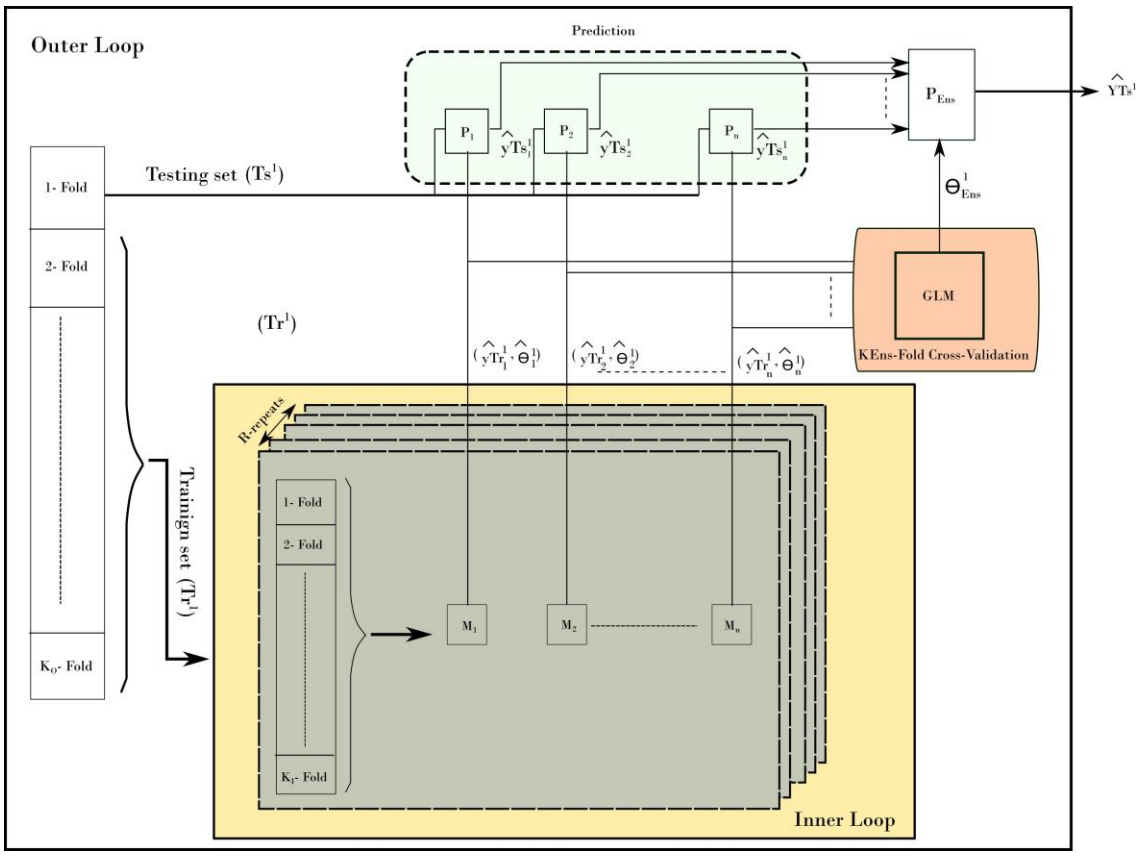


Figure 4-3: The nested-cross-validation procedure for predicting age. The example here demonstrates the first fold of the outer loop. The procedure consists of an inner loop (yellow color) and outer loop (grey color). The inner loop is used to find the best models to predict age. The outer loop uses those models to predict the age on the testing set. The process is repeated for all folds of the outer loop, which results in building a prediction of age from all samples.

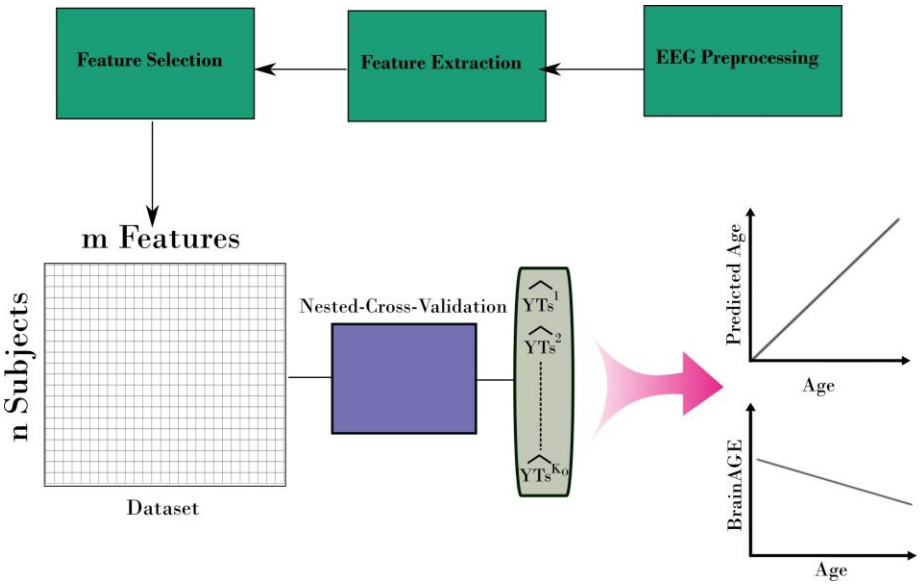


Figure 4-4: The complete framework for estimating the BrainAGE from EEG. The framework uses the nested-cross-validation method to build estimations for age. Those estimations are then used to calculate BrainAGE from the entire dataset.

4.3 **Results**

NCV R^2 performance (i.e., variance shared between predictors and outcome) for stack-ensemble and underlay methods is shown in **Figure 4-5**.

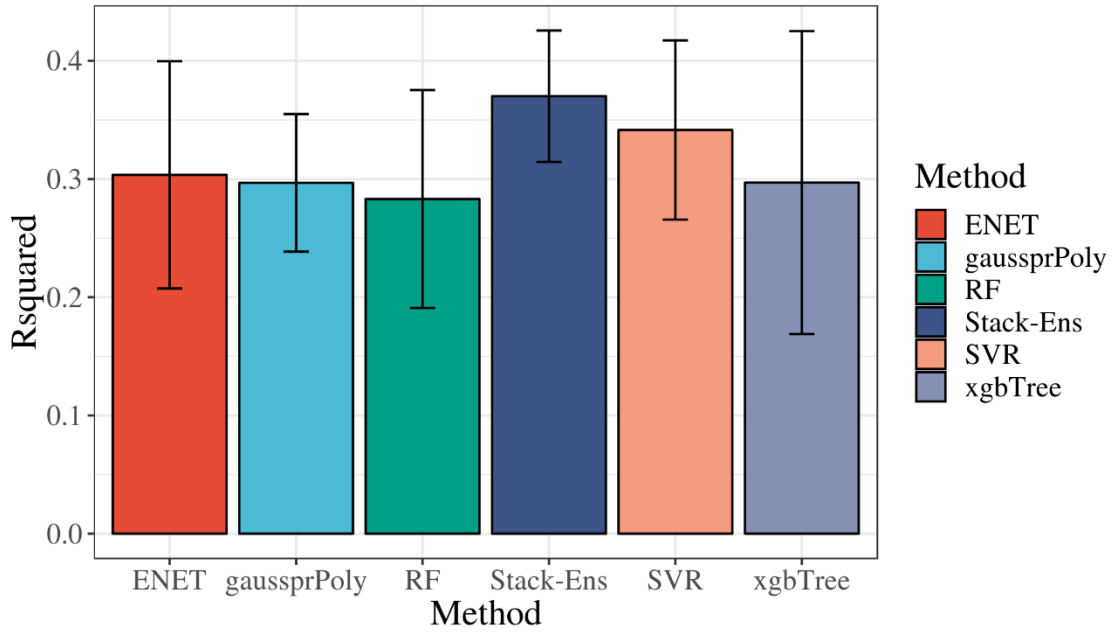


Figure 4-5: Model performance in terms of the explained variance using NCV. Error bars represent the standard deviation of performance across the outer loop of the NCV.

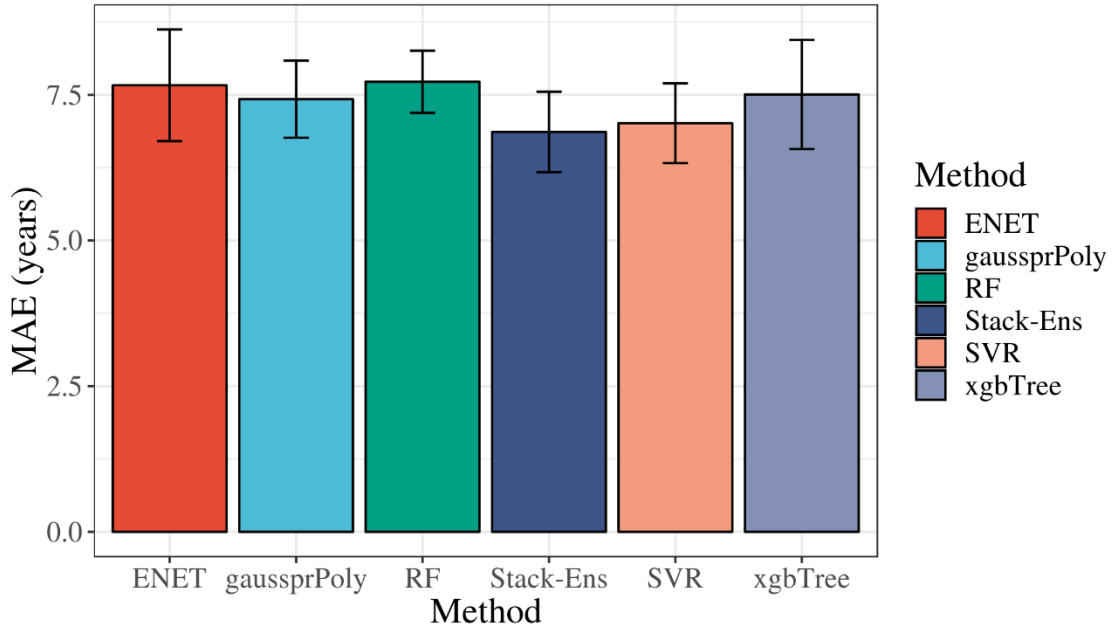


Figure 4-6: Model performance in terms of MAE using NCV. Error bars represent the standard deviation of performance across the outer loop of the NCV.

The individual performance for each ML method was calculated before the stack-ensemble phase. Results showed that SVR with radial kernel was most accurate: $R^2 = 0.34(0.06)$; MAE=7.01(0.68) years; and Root Mean Square Error (RMSE)=8.7(0.63) years. The stack-ensemble improved overall performance with $R^2 = 0.37\ (0.064)$; MAE=6.87(0.69) years; and $RMSE = 8.46\ (0.59)$ years.

The correlation between predicted age and actual age is shown in **Figure 4-7**, sharing approximately 36% of the variance.

The correlation between predicted age and actual age is shown in **Figure 4-7**, sharing approximately 36% of the variance.

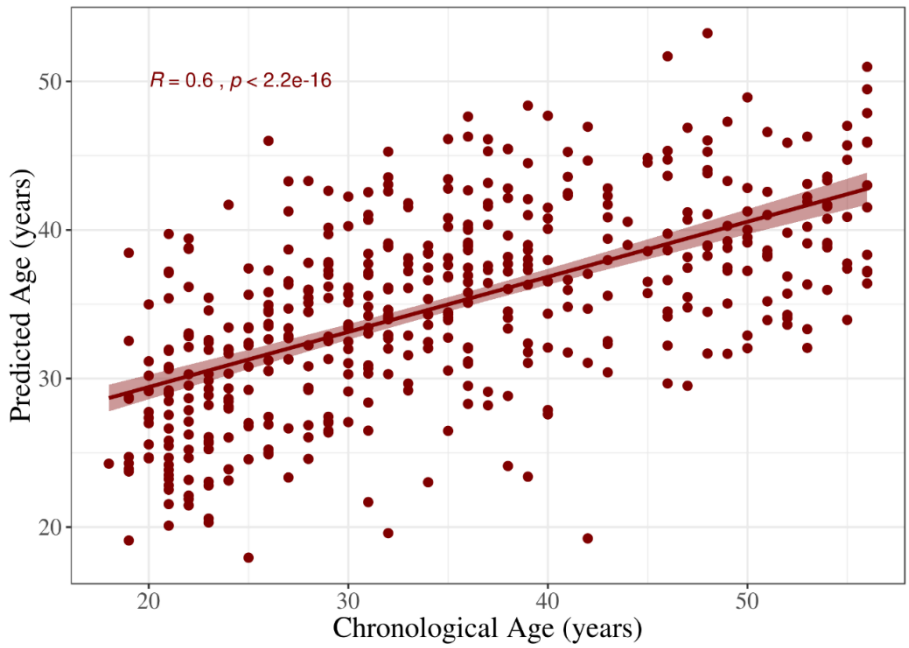


Figure 4-7: Predicted age vs. age constructed from the outer loop of the NCV.

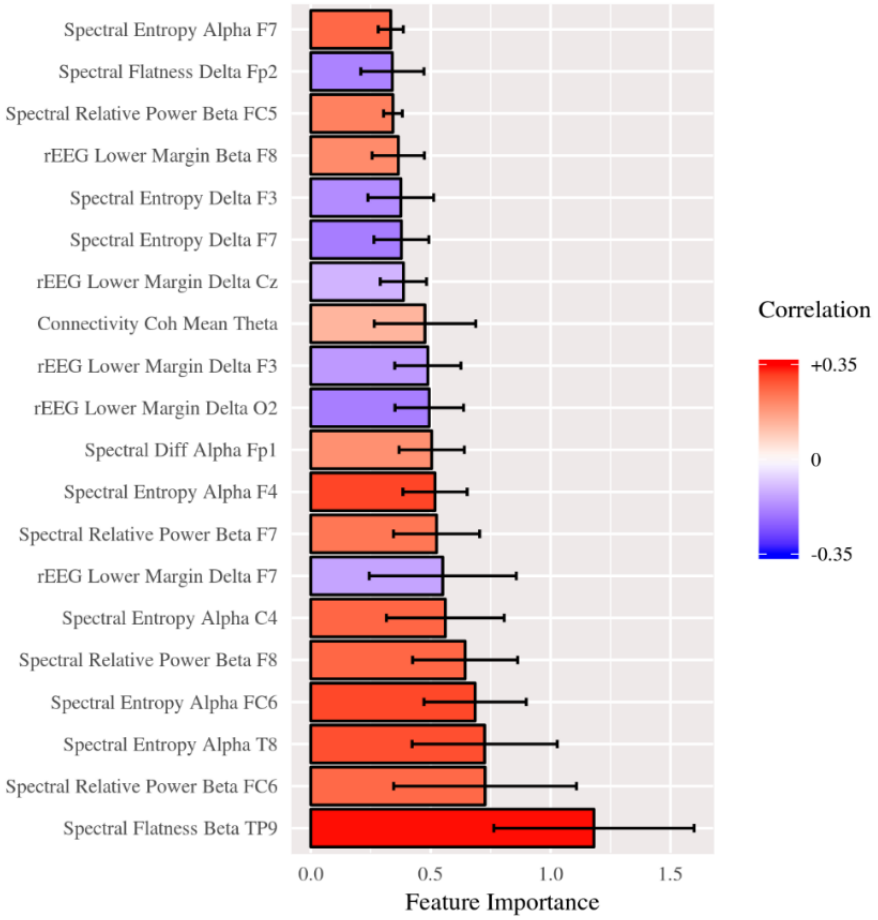


Figure 4-8: The 20 most important features for predicting age, sorted from most important (bottom) to least important (top). Ventricle axis shows the scoring values from the stack-ensemble model predictor, while the color indicates the correlation values between that feature and age.

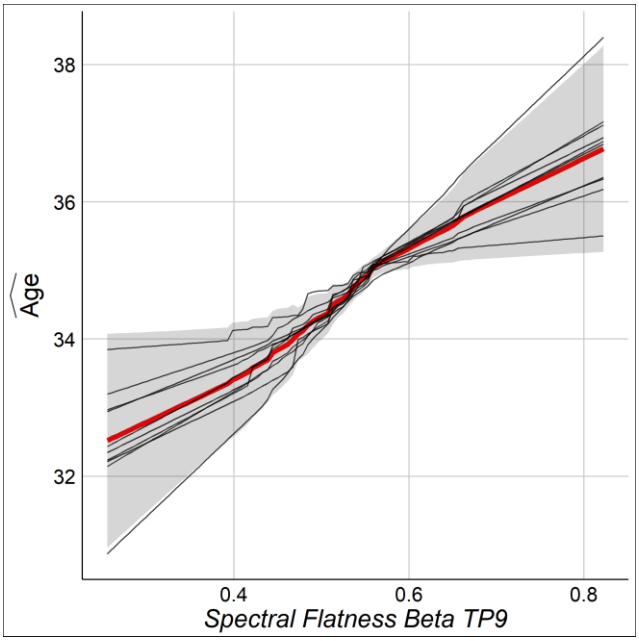


Figure 4-9: PDP for the top feature from NCV via the stack-ensemble model

Importance of features was estimated such that total summation of feature importance is 100 from each fold of the outer loop of the NCV. Subsequently, importance scores were averaged across folds. In this case, results were reported as the mean across all folds. **Figure 4-8** shows the 20 most important predictors of age. The color of the bars represents the Pearson's correlation values between each predictor and age. From the graph, we can see that "spectral flatness of beta band from channel TP9" is the most important predictor of age, where $r = 0.34$. Please refer to **Figure B4** in **Appendix B** for detailed graphing of the relationship between the leading predictors and age.

The relationships between chronological age and the most important features were described by the Partial Dependence Plot (PDP) [144] for each training model, and consistency across folds was examined by overlaying the PDP curves. It is desirable for the same feature to behave similarly among the folds of the outer loop of the NCV. **Figure 4-9** shows the PDP for the most important feature. PDP for each fold (i.e., thin lines)

shows consistent behavior among all folds. **Figure B6** in **Appendix B** illustrates PDPs for the leading features.

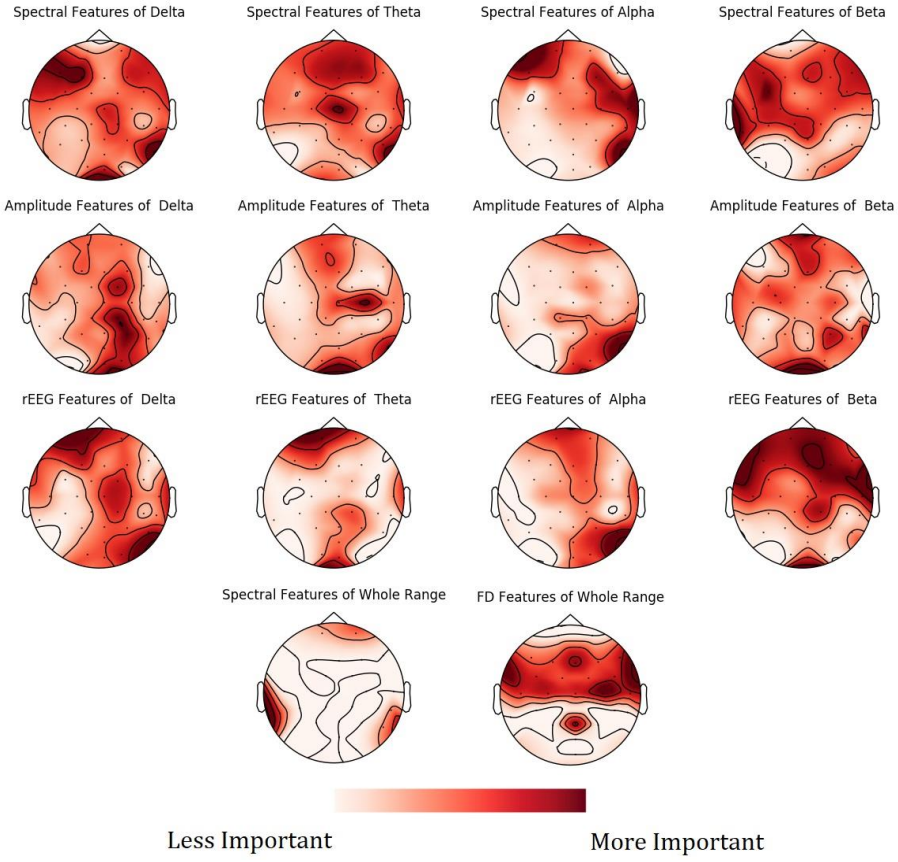


Figure 4-10: Mean feature importance scores sorted by bands and channels for predicting age. The darker the color, the more important the feature.

To show spatial distribution of feature importance, MNE software [145] was used. More specifically, feature importance scores obtained from the NCV were averaged based on feature type and categorized based on frequency bands. The resultant mapping for the feature importance scores is shown in **Figure 4-10**.

Finally, work reported in this chapter considered the effect of several samples on performance in predicting age. The framework was tested on a different number of

samples. **Figure 4-11** graphs the R^2 of the NCV as a function of the number of samples in our dataset.

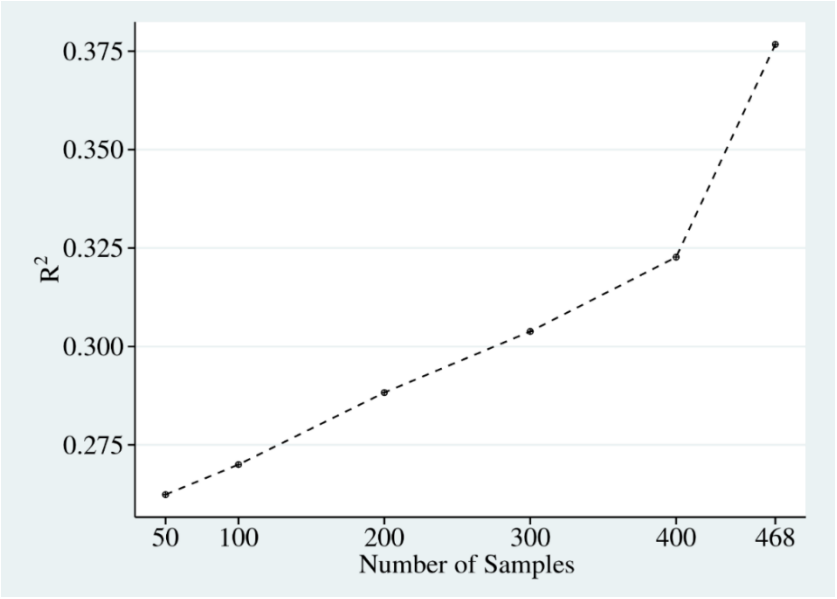


Figure 4-11: The effect of the number of samples on age prediction.

4.4 Discussion

4.4.1 Age-related changes are affecting brain EEG signals

Results suggest that indeed aging affects human brain EEG signals. This work also determined that comprehensive feature extraction is required from EEG signals to capture the relationship between chronological age and age predictors. This suggests that aging is reflected broadly on the EEG signals without one selected predominating feature and also suggests that utilized EEG predictors feature various mechanisms of influence by age. Additionally, for feature extraction, selecting the best features is vital for improving performance and reducing model complexity. Correlated features were

eliminated to select preferred features, which improves the overall R^2. The selection for correlated features preserves the consistency among NCV folds and, more importantly, eases interpretation of results. The age-related changes in EEG are strongly supported by the literature [126-131, 146] and by results detailed in this work, as well, where the correlation between the four most important features and age was relatively high: r=0.34, 0.3, 0.26, and 0.24, respectively.

4.4.2 Can age be predicted from EEG signals?

Given an unbiased prediction of age using NCV, it was possible to achieve reasonable accuracy for predicting age. Optimal results were obtained by SVR ($R^2 = 0.37$) and were slightly improved by the Stack-ensemble approach ($R^2 = 0.38$). The correlation between predicted age and age was also relatively high (r=0.60), which shows the ability of the model presented herein to predict this objective metric. Overall feature importance scores were extracted for each fold in the outer loop of the NCV, and then averaged across all folds. Feature importance showed that leading predictors are spread out across different features, types, and bands. Also, a PDP was used to examine the consistency of features across the outer loops of the NCV, where leading features were shown to have a similar behavior across the folds.

The effect of the number of samples on prediction accuracy is shown in **Figure 4-11**. The graph indicates a potential improvement may be achievable by adding more samples. When testing on 50 samples, overall accuracy was R^2~=0.26, which shows that the features are informative for predicting age, even from a small number of samples. It should be noted that the sample size used in this work was relatively smaller than the size used in other works, especially those that used MRI.

Mapping spatial distribution of feature importance scores revealed that age predictors do not uniquely correspond to specific channels, frequency bands, nor to a specific feature domain. That is, different feature types capture some characteristics of EEG, but not the entire relationship. For example, **Figure 4-8** showed that among the 15 most important features, spectral features are positively correlated with age, while rEEG features are negatively correlated (i.e., one type of feature captures a specific aspect of the relationship between that feature type and age). Thus, providing heterogeneous features can improve the predictability of age. This is also supported by **Figure 4-10**, wherein the spatial distribution of feature importance scores does not exhibit a uniform representation. This analysis shows that the relative contribution of feature importance is 46%, 31%, 18%, 3%, and 2% for spectral, rEEG, amplitude, FD, and FC, respectively. It should be noted that the number of features among different domains are not the same; this is especially the case for FD and FC features. Similarly, feature contributions are also spread out across bands, as follows: 31%, 21%, 27%, and 18% for theta, delta, alpha, beta, and theta, respectively.

4.2.3 Comparison with other works

Predicting age from EEG features was also studied in [132]. When compared with this study, one will note that those authors reported relatively higher prediction accuracy—0.6 compared with 0.4 in this work. There are several differences which may contribute to this disparity. Perhaps the most significant difference is that the researchers seem to have selected features using the response variable and the entire dataset, which will generally lead to more positive evaluations when compared with selecting features within an NCV framework, as done in this work. Additionally, R^2 was reported in this

study as 1-SSresid/SStotal (i.e., SSresid is the squared residuals from the regression; SStotal is the total sum of squares of differences from the mean) taken from the model prediction, while researchers from the other study seem to have reported the R^2 of a line fit through age vs. predicted age. Other differences include the feature sets used and the fact that EEG data in this work were collected during fMRI, which may leave some residual artifact. Furthermore, interpretation-friendly features were used in this work.

Predicting age from functional brain imaging is probably more challenging than structural imaging. This chapter proposes a robust and rigorous framework to predict BrainAGE using different features of EEG signals recorded during fMRI in a sample of N=468 individuals. First, an open-source EEG feature extraction software was extended in MATLAB [136] to provide a feature representation of individual subjects. Then, a set of ML methods was applied to predict age from features.

Table 4-1 shows that fMRI generally yields a lower performance than structural MRI data. Best results were reported by [114] with r=0.96 from structural imaging of healthy subjects. EEG and fMRI are both functional imaging for the brain, and thus, are more subjective to compare EEG results with fMRI results. The method reported herein indicates performance is relatively lower than those from fMRI works reported in [117] with R^2=0.55 and [118] with MAE = 4.6 years. Without a subjective comparison between EEG and fMRI from the same dataset, it is hard to draw conclusions about the amount of information that each domain embeds. Although fMRI/MRI imaging may yield a higher accuracy, this method comes at extra cost and less portability when compared with EEG methods.

The contribution of some features linked to BrainAGE is in line with previous works [147, 148]. For instance, the findings in this work replicate a negative correlation between age and alpha power spectra in healthy groups initially reported in [147]. This correlation trend was also observed in other frequency bands, especially delta and theta bands. FD is positively correlated with age for healthy subjects (see **Appendix B**, **Figure B7**), which is consistent with a prior finding in [148]. However, [148] showed that FD increases for subjects aged from 20 to 50 years, and then decreases. Since the age limit in this work is 58, the pattern is increasing overall for ranges from 18 to 58 years. **Figure B6** and **Figure B7** in **Appendix B** provide a spatial mapping of the correlation values between the spectral and FD features and age.

4.5 Limitations

This chapter used a set of static EEG features to predict age for 468 subject. EEG preprocessing was applied using an automatic preprocessing pipeline instead of manual preprocessing. Moreover, the used dataset consists of heterogeneous subjects, due to the limited number of HC subjects. Finally, for feature selection, correlated features were removed from the datasets. Other feature selection methods can be tested and evaluated.

4.6 Conclusions

This chapter introduced the rigorous framework for BrainAGE estimation based on EEG brain signals. Proof-of-concept analysis showed that it is possible to build a robust BrainAGE estimation by harnessing both extensive EEG feature representation and suitable ML algorithms. ML and NCV play a significant role in identifying

informative features and studying the spatial distribution of significant predictors, as well as providing unbiased prediction. In addition, this work showed how to evaluate and interpret the results using the feature importance scores and partial dependence plots. The introduced framework can be extended to test association with and predict other physiological relevant measures based on EEG brain signals.

Chapter 5 : BrainAGE Prediction Using Simultaneous EEG-fMRI Features

5.1 Introduction

Extracting BrainAGE predictors from EEG data was investigated in **Chapter 4**. Results showed that wide-range heterogeneous features can predict age, yielding an explained variance of $R^2 = 0.37$. The challenges of building age predictors from EEG are rooted in the nature of EEG data and the type of information that EEG measures. In other words, EEG is a functional measurement of brain activity, and thus, age prediction relies on how much functional information changes with age.

This chapter investigates the extent to which information about fMRI features reveals about age. More specifically, how is aging associated with brain functionalities, and what potential features are linked to age? Also, the shared information between EEG and fMRI for predicting age is investigated in this chapter. More specifically, the correlation between predicted age from EEG is compared with predicted values from fMRI features. Finally, improving the predictability of age from simultaneous EEG and fMRI is explored by prediction fusion. To do so, this work used simultaneous EEG-fMRI recording from the same cohort of heterogeneous participants used in **Chapter 4**. The literature review for using neuroimaging modalities for BrainAGE was extensively discussed in **Chapter 4** and, therefore, not duplicated below.

5.2 Defining Regions of Interest from fMRI BOLD Signal

Identifying brain regions of interest (ROIs) is an essential step for any fMRI analyses since it could significantly affect the predictability and identification of the assumed response (e.g., clinical assessment measure, neural activity in a brain region, or accuracy of performing a task). The network structure and connectivity of the brain must be considered for selecting ROIs. For example, one can select ROIs from within specific RSN or specific brain regions. Defining these ROIs is beyond the scope of this work. Therefore, a predefined set of ROIs was used from the seminal work presented in [149]. Specifically, authors in [149] defined n=279 ROIs that span most resting state networks. Specifically, these ROIs are defined in a way that minimizes the short distance correlation between ROIs while forming similar spatial/functional distributions of the known brain networks. **Figure 5-1** shows the distribution of the ROIs colored based on indices of the ROIs.

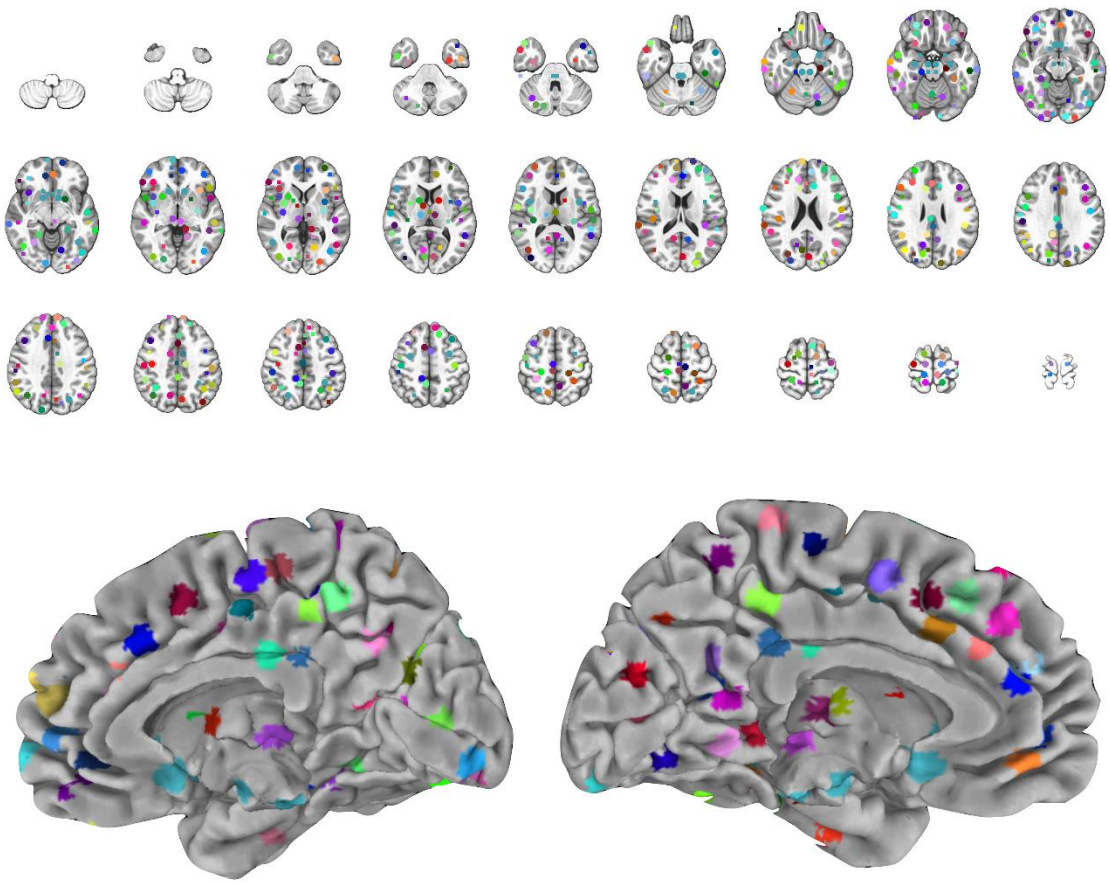


Figure 5-1: The selected ROIs for feature extraction from fMRI colored based on the indices of the ROIs. The top part represents the 2D Axial view for the locations of the ROIs, and bottom part shows the 3D Sagittal view of the ROIs.

5.3 Methods

5.3.1 Participants

Participants were selected from the 500 subject T-1000 study. Please refer to **Section 1.7** of **Chapter 1** for more information about the population of participants.

5.3.2 EEG-fMRI Data Aqusition

Please refer to **Section 1.8** in **Chapter 1** for detailed information about data acquisition. This chapter highlights simultaneous EEG-fMRI recordings from 456 subjects after passing quality assurance procedures. The following section describes the necessary preprocessing steps for suppressing artifacts.

5.3.3 EEG Data Preprocessing

Please refer the preprocessing procedure deployed in **Chapter 4**, **Section 4.2.3**.

5.3.4 fMRI Data Preprocessing

The following preprocessing pipeline is adapted by the neuroimaging community and used as-is to suppress artifacts. To best of this author's knowledge, the deployed steps yield best results for preprocessing data (See **Figure 5-2** for a general overview about procedure of preprocessing the fMRI data). Imaging analyses were carried out using Analysis of Functional NeuroImages (AFNI) software (http://afni.nimh.nih.gov/afni/). The afni_proc.py command was employed to preprocess the data using the default parameters, unless otherwise noted. The first three volumes were omitted from the analysis. The despike option was applied to replace outlier time points with interpolation. RETROICOR [150] and respiration volume per time (RVT) correction [151] were applied to remove cardiac- and respiration-induced noise in BOLD signal. Slice-timing differences were adjusted by aligning to the first slice, and motion correction was applied by aligning all functional volumes to the first volume. EPI volumes were acquired using the 3dvolreg AFNI program with two-pass registration. The volume with the minimum

outlier fraction of the short EPI dataset acquired immediately after the high-resolution anatomical (MPRAGE) brain image was used as the registration base. Linear warping was applied to the MNI space and resampled to 2 mm^3 voxels. Also, individual time points and previous ones were censored, where the root sum square motion was greater than 0.2 mm.

Noise reduction was implemented by regressing out: (1) low-frequency fluctuation from the signal time course (i.e., third-order polynomial model), (2) 12 motion parameters (i.e., three shift and three rotation parameters with their temporal derivatives), (3) local WM average signal (ANATICOR) [152], and (4) three principal components of the ventricle signal from the signal time course. FreeSurfer 5.3 (http://surfer.nmr.mgh.harvard.edu/) was used to extract WM and ventricle masks from the anatomical image of an individual subject, and then warped them to the normalized fMRI image space. Frame-wise displacement and DVARS were calculated according to [153] using the FSL motion outliers package (https://fsl.fmrib.ox.ac.uk/fsl/fslwiki/FSLMotionOutliers).

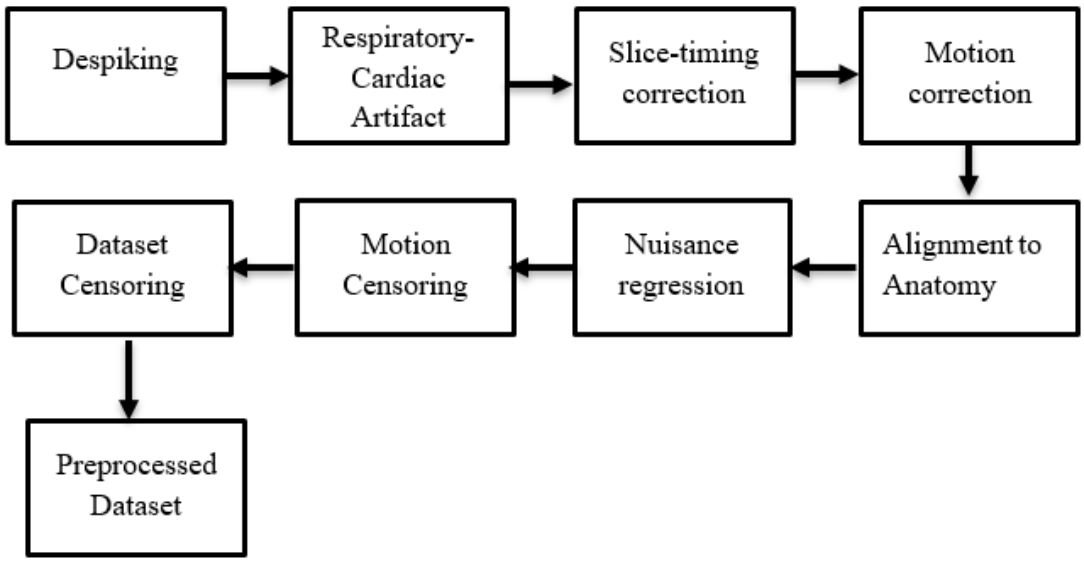


Figure 5-2: fMRI preprocessing pipeline.

5.3.5 Features of Interest

Several features can be extracted from the selected ROIs. The work presented herein focuses on two sets of features. The first set of features depends on the pairwise FC between ROIs and deplpoys Pearson's correlation for this purpose. More specifically, the BOLD signal from each ROI is averaged and correlated with every other BOLD signal from other ROIs. Similar features have already been used in the literature [154, 155], albeit using a different ROI selection procedure. For selected ROIs reported herein, this resulted in a feature vector with $n = (279 \times 278)/2 = 38781$ elements. Thus, further feature reduction was needed and is explained in the next section.

The second set of features relies on the amplitude of low-frequency functions (ALFF) in BOLD signal, which is identified as the total power within the frequency range of 0.01 and 0.1 Hz [156]. ALFF can measure the low-frequency BOLD fluctuation of the brain hemodynamic activity and may indicate the correlated activities within RSNs of the

brain. ALFF is estimated as a single value from each ROI's BOLD signal, and then concatenated with the estimated ALFF values from other ROIs, resulting in a feature vector of n=279. Similar to FC features, ALFF has been used for clinical prediction [157-159].

5.3.6 Features Preprocessing

The high dimensionality of fMRI has always been a challenge for ML methods. Focusing on the 279 ROIs alleviates the curse of the dimensionality in the data; however, FC features still suffer from this problem. Thus, a further feature selection and reduction are needed. In order to do that, the correlated features between subjects were removed, as was utilized in **Chapter 4**. The threshold for removing the correlated features was set to (thr=0.5). This procedure reduced the number of features for FC from 38781 features to 3693.

It should be noted that other thresholds can be used, but at the cost of accuracy and computational efforts. That is, using lower threshold values results in smaller numbers of features, yet removes potential information in the data. On the other hand, using larger threshold values may retain more information, yet increases the computational overhead.

5.3.7 Machine Learning Methods

A similar ML framework used in **Chapter 4** was adopted for fMRI features. However, to reduce computational efforts, only SVM and RF were deployed. Training and testing were done using (K=5) nested-cross-validation procedure.

To combine predictions from all feature sets (e.g., both fMRI and EEG), a GLM was used to fuse prediction after training on EEG, ALFF, and FC features. Particularly, for each

fold of the NCV, a GLM model was trained from each set of features on the predicted age of the remaining 4-fold predictions. Then, the trained GLM was tested on the current fold predictions. A final prediction vector was constructed and compared to the actual age values (See **Figure 5-3**).

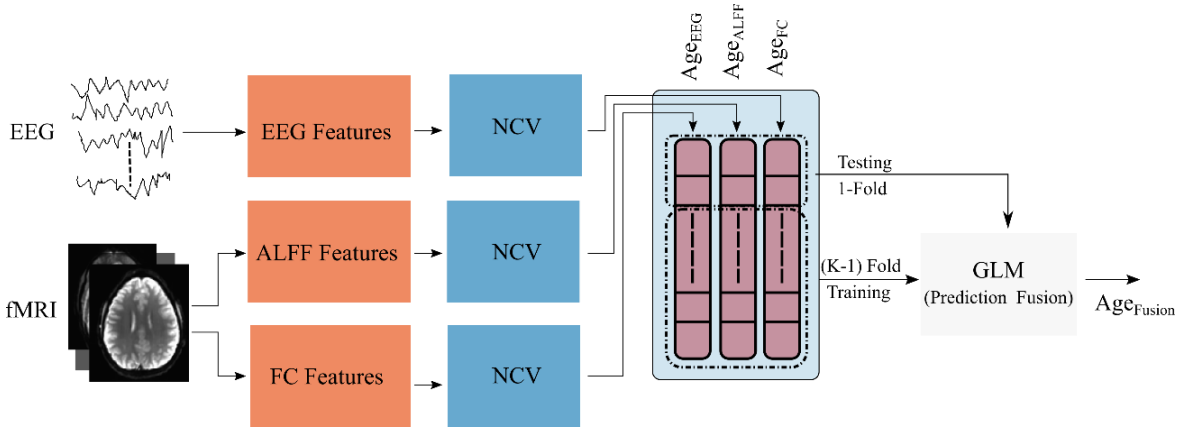


Figure 5-3: Age prediction fusion from EEG -fMRI features. The predicted age values from each set of features (Age_{EEG}, Age_{ALFF}, and Age_{FC}) are used to train a GLM model using cross-validation. The final predicted age (Age_{Fusion}) is constructed from GLM prediction.

5.4 **Results**

Using the NCV framework presented in **Chapter 4**, the age prediction from each set of features was computed. For each modality, the correlation between age and the predicted age was investigated. Specifically, we plotted the predicted age vs. chronological age for SVM (**Figure 5-4**), RF (**Figure 5-5**) for RF, and the ensemble method (**Figure 5-6**). In addition, RMSE, MAE, and the explained variance for the NCV was estimated (**Table 5-1**).

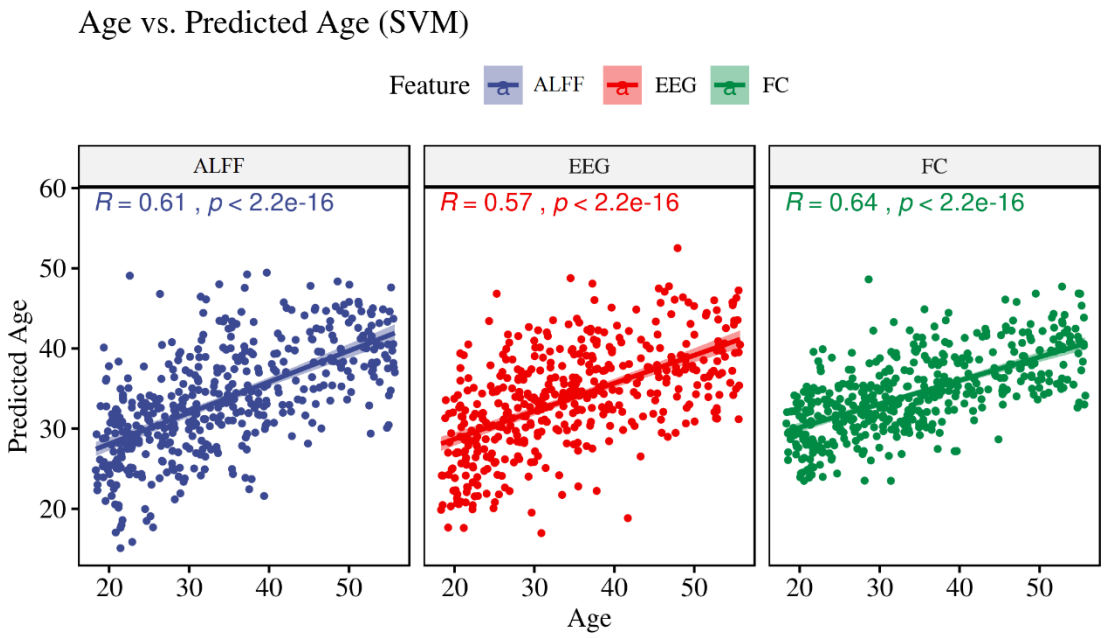


Figure 5-4: The correlation between age and the predicted age using SVM for ALFF, EEG, and FC features.

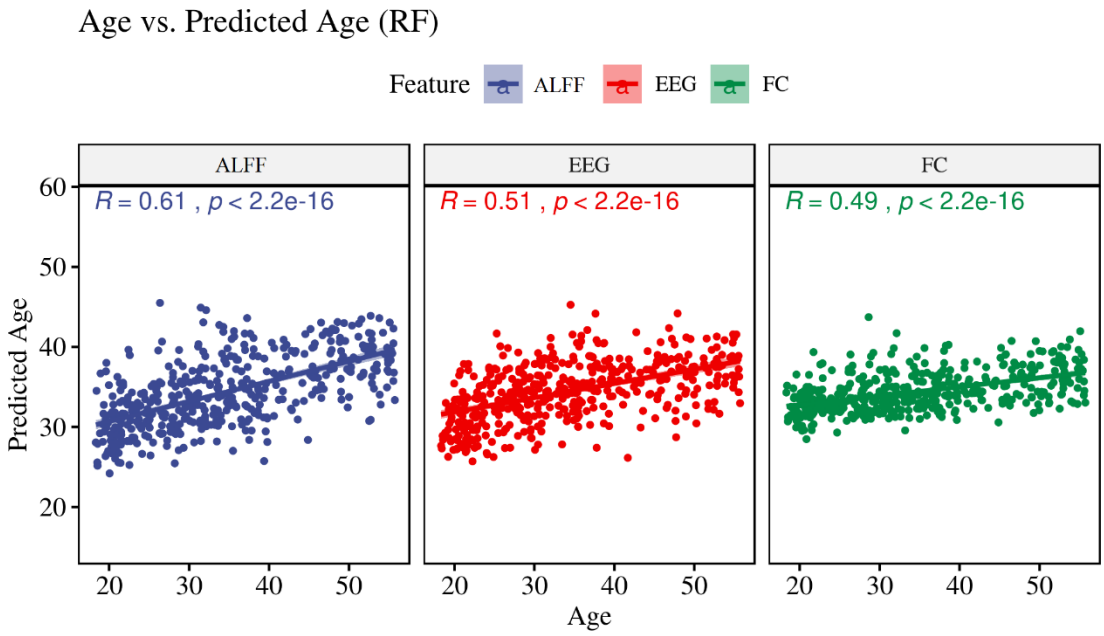


Figure 5-5: The correlation between age and the predicted age using RF for ALFF, EEG, and FC features.

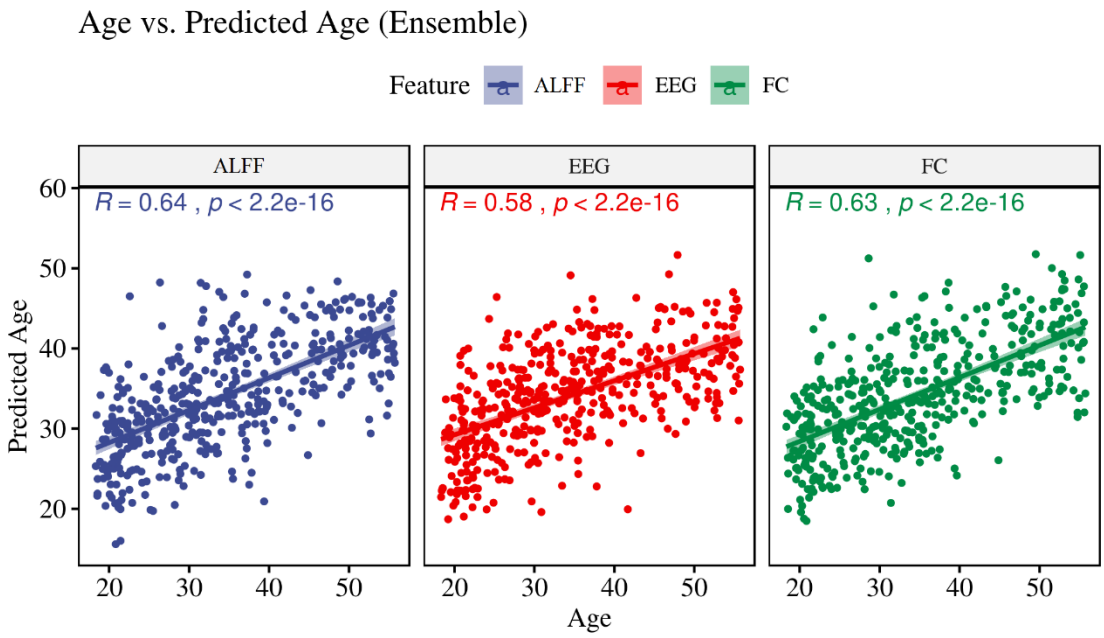


Figure 5-6: The correlation between age and the predicted age using the ensemble model for ALFF, EEG, and FC features.

Table 5-1: The performance of age prediction from EEG, ALFF, and FC set of features.

Features	RMSE	R^2	MAE (years)
EEG	8.62	0.33	6.92
Functional Connectivity	8.24	0.41	6.69
ALFF	8.26	0.40	6.67
Fusion	7.29	0.54	5.87

Next, the fused predictions from all feature sets were estimated using the GLM model, and then the scatter plot of age vs. predicted age was depicted.

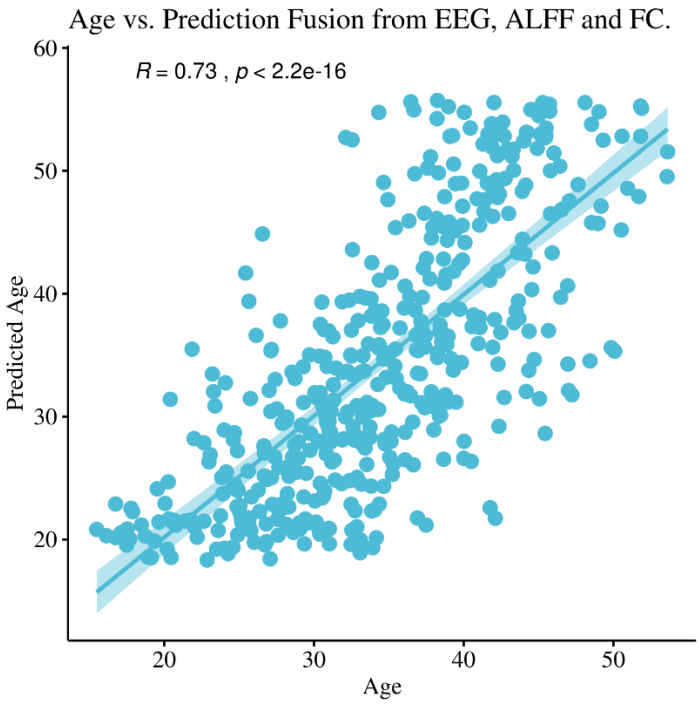


Figure 5-7: The predicted age vs. the chronological age using GLM prediction fusion.

To investigate the shared information that each modality has about age, the correlation matrix among predicted age values from each modality was computed (**Figure 5-8**).

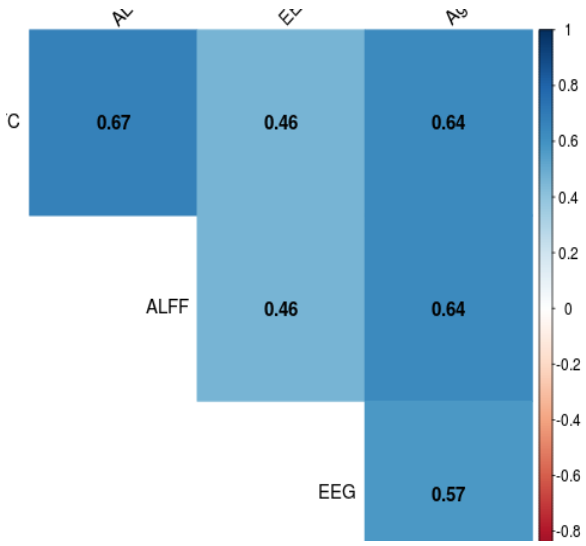


Figure 5-8: The correlation matrix of predicted age values from EEG, ALFF, and FC set of features.

5.5 Discussion

Predicting age from fMRI data may carry important information about how aging is linked to various brain functions. Unlike predicting age from structural imaging data, estimating age from functional imaging may be challenging due to high dimensionality and data variation. Nevertheless, **Chapter 4** has revealed that it is possible to predict the age from heterogeneous EEG features. This chapter extended the effort of predicting age from EEG by using other types of functional imaging, fMRI, and further combining prediction from EEG and fMRI. In order to do this, the ALFF and FC from 279 ROIs were extracted from 453 datasets. Using NCV—which was introduced in **Chapter 4**, age was predicted using EEG feature (explained in **Chapter 3**), FC, and ALFF of fMRI features. The obtained results revealed that FC and ALFF of fMRI hold significant information about age. Specifically, the unbiased NCV framework yielded R^2 of 0.41 for the ensemble model when evaluated on the FC features. Similarly, ALFF yielded a close prediction performance with an R^2 of 0.40 for the ensemble model. These results suggest that age is associated with a wide range of effects on the functionality of the brain. Notably, each set of fMRI features carries different information about aging, since the correlation between the predicted age from each set of features was different. This phenomenon has been shown in the correlation matrix of predicted age (**Figure 5-8**). With a maximum of 0.46 correlation among EEG and fMRI predicted age values, the results suggest that fMRI and EEG feature sets potentially carry shared information about age. However, the results also suggest that EEG and fMRI measure different aging indicators from the brain since there is no perfect correlation between predicted age from EEG features and fMRI features. Furthermore, combining prediction from all features sets has

improved the predictability of age, which explains up to 54% of the variance in the data and indicates that age prediction fusions leveraged more information about the age from the three sets of features.

5.6 Limitations

The presented work deployed EEG-fMRI feature sets to build a BrainAGE predictor. Two types of fMRI feature sets, namely ALFF and FC, were used. Other features can be adopted and studied. Also, a predefined set of ROIs was used to extract fMRI features. There are several kinds of ROIs based on the anatomical or functional distribution that can be harnessed [160, 161]. Moreover, prediction fusion was applied at the level of the predicted age values from individual feature sets. Other types of fusion can be examined, like fusion at the level of the features. Finally, a simple feature selection was utilized for FC features. Investigating other feature selection methods could improve the predicted age, especially for FC features.

5.7 Conclusions

In this chapter, combined EEG-fMRI features were used to predict age using the ML framework introduced in **Chapter 4**. Two sets of functional features were extracted from fMRI data, namely FC and ALFF. Then, the ML framework was trained independently on the two sets of features. From there, the unbiased prediction of age values was estimated. A final predicted age was constructed from fMRI features and EEG features extracted from work completed in **Chapter 4**. The analysis revealed that EEG and fMRI features share significant information about age, although each modality has its own

fingerprint about age. Moreover, prediction fusion has shown the benefit of using simultaneous EEG-fMRI for enhancing the accuracy of the predicted age and, potentially, other outcomes.

Chapter 6 : Studying Brain Based Biomarkers of Mood and Anxiety Disorders: An EEG-ms Informed fMRI Analysis

6.1 Introduction

In **Chapter 1**, we relied on the literature to explain the benefits of integrating simultaneous resting state EEG and fMRI data to maximize both temporal and spatial resolution. Work detailed in **Chapter 2** and **Chapter 3** extracted two sets of EEG features that were used from characterizing MA subjects and building BrainAGE predictor, respectively. Using EEG features extracted from work reported in **Chapter 4**, the benefit of using simultaneous EEG-fMRI features were shown for studying shared information about the age between EEG and fMRI. Moreover, this work has shown how combining those modalities could improve the accuracy of age prediction. This chapter focuses on using EEG-ms features to localize the brain regions associated with EEG-ms in the fMRI side and, more importantly, how the identified changes in EEG-ms features are manifested in the brain. The relationship between EEG-ms and the BOLD signal has been investigated in [25], which revealed that EEG-ms possess a scale-free property related to changes in BOLD oscillations.

Furthermore, other works have correlated BOLD signal with EEG-ms time courses using the GLM analysis to localize brain regions associated with EEG. For

instance, using the canonical EEG-ms analysis described in **Chapter 2**, authors in [24] demonstrated that: 1) MS-A is negatively correlated with BOLD signal in the bilateral superior and middle temporal lobe; 2) MS-B is negatively correlated with BOLD signal in the bilateral occipital cortex; 3) MS-C is positively correlated with BOLD signal in the right insular cortex, bilateral inferior frontal cortices, and the dorsal anterior cingulate cortex; and 4) MS-D was negatively associated with the BOLD signal within frontoparietal regions. Authors in [58] extracted 10 EEG-ms, revealing a significant association between the spatial maps of EEG-ms and BOLD signal.

Additionally, investigations have related EEG-ms with the BOLD signal, using non-conventional EEG-ms analysis. For instance, authors in [23] extracted EEG-ms using ICA and associated EEG-ms with the ICA time course of fMRI RSNs. Identifying the source of EEG-ms from high-density EEG recordings has been explored in [66], revealing that EEG-ms sources are located in cingulate cortices, precuneus, superior frontal cortex, supramarginal gyrus, dorsal superior prefrontal cortex, and insular cortex. It should be noted that the results have shown to be relatively similar to the GLM-yielded brain regions reported by [65]. From a clinical point of view, combining EEG-fMRI may provide more insight into understanding the ramifications of adverse health conditions. For example, EEG-fMRI analysis has been applied to the study of both PTSD [22] and more notably, epilepsy [48, 162-164].

In this chapter, the effort of combing EEG-ms with fMRI was extended by identifying brain templates associated with MSs. Templates were used to study the FC between those brain regions for the same MA subjects used to obtain results in **Chapter 3**.

6.2 EEG-ms inform fMRI

There is a wide range of information that can be extracted from EEG; however, this work focused on EEG-ms features for the following reasons: 1) EEG-ms are broadband (i.e., multifrequency), and 2) EEG-ms represents topographic representation from all electrodes used to collect EEG measurements of brain activity. Thus, the burden of providing a systematic selection of the frequency of interest from EEG is avoided, and the challenges of selecting spatial information from EEG data are eliminated. In addition, EEG-ms are well characterized, and the classes of EEG-ms are well replicated across many works [56, 89]. Therefore, the foundation of supporting findings from EEG-ms regressors is well justified, since EEG-ms reflect large coherent in time and space neuronal brain activity. Finally, EEG-ms metrics have been used widely in the literature to study various mental disorders. If EEG-ms can reveal various mental disorders' specific alterations of brain functionality while revealing proper spatial localization, a more nuanced understanding of psychopathology of different mental illnesses, including depression and anxiety, can be obtained.

The traditional approach for data fusion of EEG-informed fMRI is GLM, which associates EEG-ms features with fMRI BOLD signal. Besides the time course of EEG-ms classes, additional second-level features (e.g., average duration, occurrence, or transition probabilities) of EEG-ms can also be harnessed to inform fMRI data analysis. However, using second-level features EEG-ms as regressors may complicate the interpretation of such results. Thus, this work relies on using the time course of EEG-ms to inform fMRI analysis, which may offer valuable information about potential biomarkers for mental disorders.

6.3 Methods

6.3.1 Participants

We used the same participants included in the study detailed in **Chapter 3** (See **Chapter 3**, **Section 3.2.1**). Excluding some subjects was necessary due to the noise in fMRI data. The final dataset used was comprised of 43 subjects for the HC group and 59 subjects for the MA group. Each subject had useable EEG and fMRI data. Furthermore, the MA group was divided into subgroups based on the comorbidity of symptoms, as Anxious-only subjects (Anx), Depressed-only subjects (Dep), subjects with Depression and Anxiety (Dep+Anx), and subjects with depression and anxiety who are substance users (Substance+). **Table 6-1** and **Table 6-2** presents the demographics of the participants based on the subgroups of MA subjects and again after lumping MA subgroups together, respectively.

Table 6-1: Demographics of EEG-ms Informed fMRI analysis dataset. The MA subjects were divided into four subgroups based on the comorbidity of symptoms.

Group	**HC**	**MA**			
Subgroup		**Dep**	**Dep+Anx**	**Anx**	**Substance+**
n	43(23Females)	16(9Females)	33(23Females)	4(4Females)	6(1Females)
PHQ	0.6(1.03)	13.25(3.02)	14.42(5.37)	7.75(2.99)	13.5(6.32)
OASIS	1.05(1.34)	8.19(3.35)	10.15(2.91)	9.25(0.96)	7.67(5.05)
STAI_State	25.74(6)	44.81(11.84)	49.45(10.01)	42.5(10.25)	41(15.58)
STAI_Trait	27.37(5.8)	53.75(11.62)	56.64(10.84)	44.25(12.04)	45.5(12.85)
Education	6.49(1.58)	6.5(1.51)	5.94(1.85)	6.25(1.71)	6(1.41)
Age	30 (11)	35 (12)	33(11)	30(12)	28(6)

Table 6-2: Demographics of EEG-ms Informed fMRI analysis dataset with combined MA subgroups.

	HC	MA
n	44(23 females)	59 (37 females)
PHQ	0.6 (1.03)	13.56(5)
OASIS	1.05(1.34)	9.31(3.29)
STAI_State	25.47(6)	46.86(11.3)
STAI_Trait	27.37(5.80)	53.88(11.81)
Education	6.49(1.58)	6.12(1.69)

6.3.2 EEG-fMRI Data Acquisition

Please refer to EEG-fMRI data acquisition protocol used in **Chapter 1**, **Section 1.8**.

6.3.3 EEG Data Preprocessing

Please refer to EEG processing procedure used in **Chapter 3, Section 3.2.3**.

6.3.4 fMRI Data Preprocessing

The same preprocessing steps used in **Chapter 5, Section 5.3.4** were used without noise reduction. All noise reduction was applied during GLM modeling (See **Section 6.3.5.3**).

6.3.5 Multimodal Analysis

6.3.5.1 Summary of EEG-ms extraction

First, the four canonical EEG-ms classes—A through D—were extracted for each group—HC and MA. To do so, the EEG data from individual subjects were average-referenced, and then filtered between 2 and 20Hz. Next, the EEG points corresponding to the peaks of the GFP [165] were selected for the subsequent segmentation step. The AAHC algorithm was used to segment the selected EEG point into the four clusters corresponding to the four canonical EEG-ms classes. After that, the group means of EEG-ms was extracted by first sorting individual EEG-ms based on the similarity between classes, and then finding the common topography across all subjects. Finally, individual subject EEG was fit-back using the group mean topographies.

6.3.5.2 EEG-ms based Regressors for fMRI Analysis

As aforementioned, the time course of each MS was used as a regressor in the GLM model. It should be noted that the term *time course* here implies a different meaning from other methods that involve time course extraction, like ICA. EEG-ms time course is the spatial similarity between each MS template and topographical representation of EEG points. Another difference that arises with the definition of EEG-ms time course is the polarity consideration of EEG-ms, where different interpretations can be drawn if polarity was considered.

To provide a better understanding of the time course of EEG-ms, the following section describes the mathematical representation of EEG-ms regressors. First, let's consider $\boldsymbol{x_t}$ electrodes value at time t. EEG-ms analysis assumes that each EEG point can be presented as:

$$x_t = \sum_{i=1}^{K} a_{it} T_i + \epsilon_t \tag{6.1}$$

where $\boldsymbol{x_t}$ is electrodes value vector at time t; a_{it} is a factor related to each MS at each time point; and ϵ_t is the error term associated with assigning that time point to one of the MSs (i.e., noise due to the lack of explained topographical representation of that point by the assigned MSs template K is the number of the assumed MSs). T_i is the template of MS i. The time course of EEG-ms is the goodness of fit for each EEG point, with respect to the MS template, and can be given as follows:

$$f = \mathrm{x}^T \times T \tag{6.2}$$

The result is a vector $n \times K$ corresponding to the fit of each MS across n EEG data points. When assigning EEG-ms classes, the following equation is applied:

$$L_i = \underset{k}{\operatorname{argmax}}(abs(f_i)) \tag{6.3}$$

The absolute term in the equation accounts for the polarity invariant property of EEG-ms analysis. In this work, goodness of fit was used as regressors for GLM analysis with and without considering the polarity, denoting them as f_p moreover, f, respectively.

$$f_p = \mathrm{x}^T \times T \tag{6.4}$$

$$f = abs(\mathrm{x}^T \times T) \tag{6.5}$$

Further smoothing was applied using a Gaussian kernel and 10-point window length for each regressor. **Figure 6-1** shows an example of the resulting regressors. Finally, each regressor was convolved with double-gamma HRF [166], and then down-sampled to TR, resulting in EEG-ms-informed regressors.

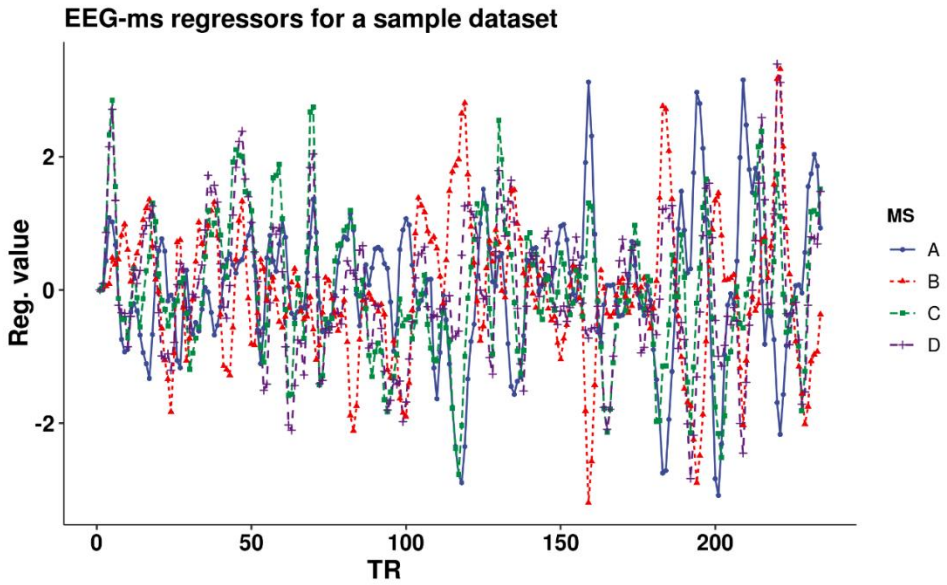


Figure 6-1: A sample of EEG-ms regressors to inform fMRI. Each regressor is used by the GLM to estimate Beta coefficients.

6.3.5.3 GLM Analysis

fMRI BOLD signal analysis was performed using the standard GLM approach with the AFNI 3dDeconvolve function [167]. The design matrix included one EEG-ms regressor corresponding to one EEG-ms class and a set of nuisance covariates: 1) low-frequency fluctuation from the signal time course (i.e., 3rd-order polynomial model); 2) 12 motion parameters (i.e., three shift and three rotation parameters with their temporal derivatives); 3) local WM average signal (ANATICOR) [152], and 4) three PCs of the Ventricle signal from the signal time course. GLM β coefficients were computed for each voxel, and then a t-test was applied for the HC group to extract the templates of EEG-ms. To control for potential false positives in BOLD signal [168], 1) the non-Gaussian spatial autocorrelation function (ACF) was estimated for the dataset; 2) AFNI's 3dClustSim was applied to the statistical map ([169]; 3) a permutation test (n=10000) was performed using the Smith procedure [170], showing that an ACF-corrected cluster requires a minimum

of 136 voxels to be deemed significant at $p < 0.05$—using an uncorrected voxel-wise threshold of $p < 0.005$.

Moreover, the GLM model excluded TR with server motion (RMS>0.2) or with severe EEG artifact (i.e., if the TR contains 50% bad intervals of EEG).

In addition to the previous steps, further exclusion was applied for the fMRI datasets given that the number of censored volumes was more than one-third of the whole number of volumes in the data. This was necessary to ensure that the GLM model had enough time to estimate beta coefficients.

6.3.5.4 Extracting Network Based Measures and Functional Connectivity

To study overall FC between different EEG-ms regions, the functional allocation index ratio (FAIR) was introduced. FAIR looks at the overall functional load for each MS when compared with others. If an MS is functionally active, then one would expect an elevation in FAIR value.

$$FAIR_L = FC_L^{in}/(FC_L^{in} + FC_L^{out}) \quad (6.5)$$

- L: EEG-ms label (A, B, C, or D).
- FC: Pearson's correlation between two time series. It is also possible to use the coherence between two time courses instead of the Pearson's correlation.
- FC_L^{in}: the average of all FC values from all pairs of brain regions connected to MS L.
- FC_L^{out}: the average of overall FC among all clusters without connections to MS L.

6.3.5.5 Graph Theory Analysis

Graph theory offers another rigorous approach for assessing functional connectivity within EEG-ms brain templates. The method investigates several characteristics of complex network connections by forming a set of nodes and edges. Each node represents one of the significant clusters in the EEG-ms templates, while edges are functional connectivity measures between nodes. Typically, the edges are formed by Pearson's correlation between the average time series from each pair of significant clusters [171-173]. Graph types are divided based on the directionality of connections into a directed or undirected graph (i.e., whether edge directions are taken into consideration or not). Also, graph types can be divided into weighted and unweighted — binary—graphs (i.e., whether edges have values or not). While choosing the graph type is up to the researcher, binary undirected graphs are the most straightforward architecture to interpret [174]. To conduct graph analysis, the FC between each pair of significant clusters in the EEG-ms brain templates was calculated. Then, an undirected binary graph was constructed from each subject.

- Small-Worldness (SM) Index: measures the balance between functional integration and separation (i.e., the balance between short distances and long distances in the graph [175]). SM has been used in several works to study clinical groups [176-178].
- Node Centrality: assesses the importance of each node based on the number of paths that go through that node. To find the global centrality for a graph, the average of nodes centrality is divided by the theoretical max [179].

- Vertex Betweenness: measures the presence of each node in the shortest path between all pair in the graph. For global graph betweenness, the average of all nodal betweenness in the graph is calculated [180].
- Clustering Coefficients (transitivity): measures the number of triangles in the graph against the total number of connected triples in the graph [172, 181].
- Path Length: measures mean length of all shortest paths that pass through each node [181].
- Global Efficiency: acts as the inverse of the shortest paths between all pairs of nodes in the graph after normalizing by the number of links in the graph.

It should be noted that there are variations in calculating graph metrics mentioned above, especially in normalizing some metrics over the number of nodes or adjusting for the disconnected graphs. All graph analyses were carried out using igraph [182] and qgraph [183] packages.

Figure 6-2 shows the pipeline of using EEG-ms features to inform fMRI analysis, including the post-hoc analysis.

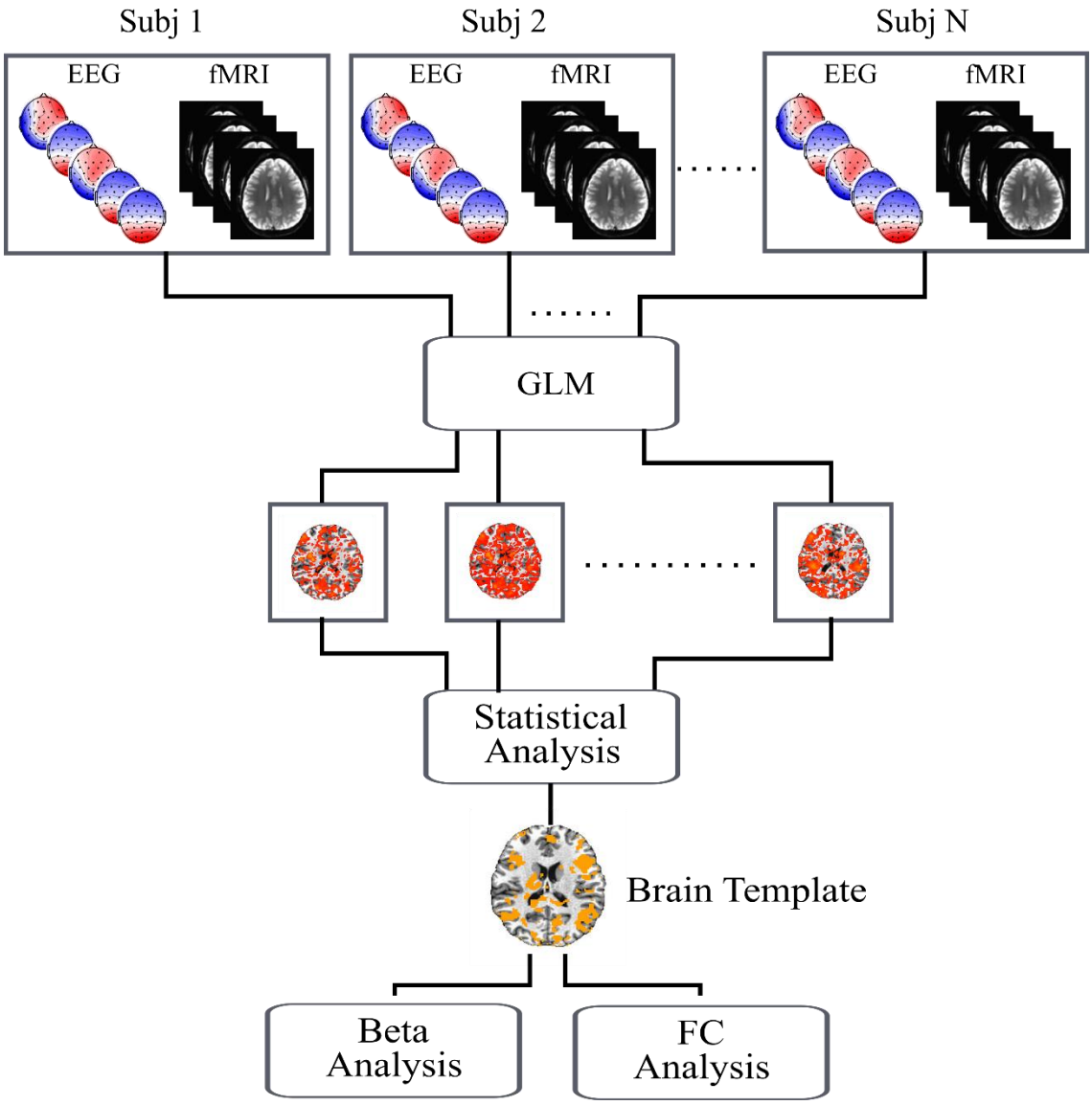


Figure 6-2: EEG-ms inform fMRI analysis framework for N subjects (Subj). The Beta coefficients of GLM are estimated for individual subjects. The statistical analysis of Beta coefficients reveals the brain regions that are active with respect to EEG-ms features. Later, those brain regions can be used as brain templates representation for the corresponding EEG-ms features. Several post-hoc analyses can be conducted based on the obtained brain templates; Beta analysis can be conducted to estimate the variation in the linear relationship between EEG-ms feature and BOLD signal. On the other hand, FC Analysis may reveals any changes in the connectivity between those brain regions.

6.4 **Results**

EEG-ms templates for both groups are shown in **Figure 6-3**.

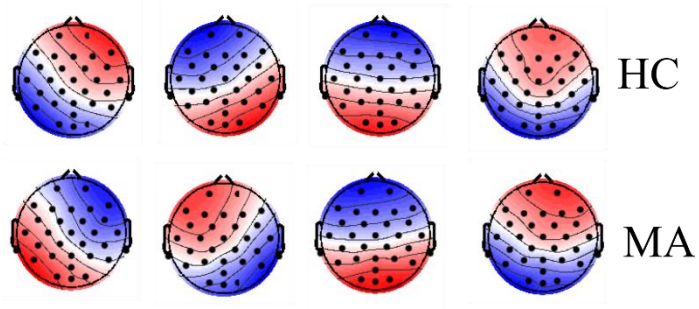


Figure 6-3: EEG-ms templates for HC and MA.

Significant clusters from HC were used as a template representation for the EEG-ms. The intention was to use HC as a functional localization dataset, and then compare the FC between those brain regions with the MA group. Similarly, β coefficients were extracted for both groups to analyze the linear relationship between BOLD and EEG-ms time courses.

The following figures unravel the significant clusters for MS-A (**Figure 6-4**), MS-B (**Figure 6-5**), MS-C (**Figure 6-6**), and MS-D (**Figure 6-7**). Detailed information about each cluster and the corresponding brain region are presented in **Table 6-3**.

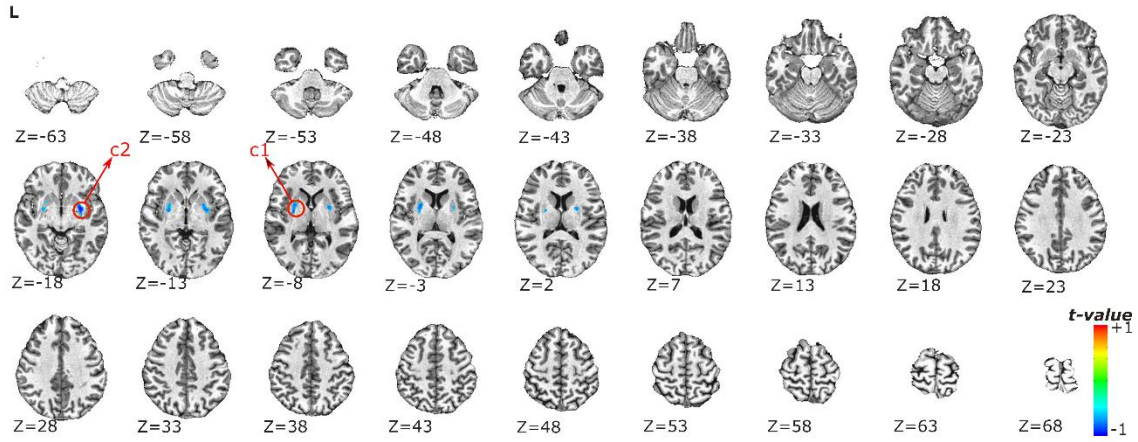


Figure 6-4: Significant clusters for MS-A. Clustering was performed at p<0 .005 and corrected at p<0.05.

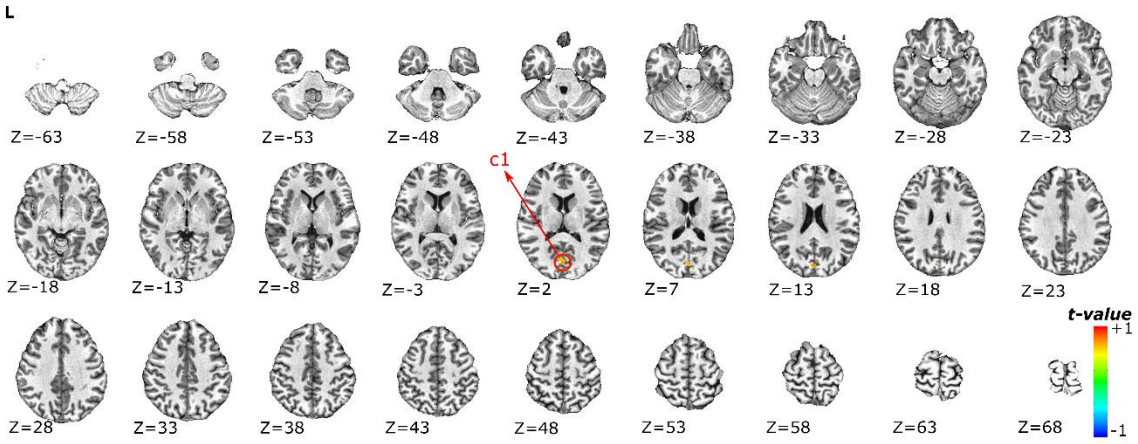


Figure 6-5: Significant clusters for MS-B. Clustering was performed at p<0.005 and corrected at p<0.05.

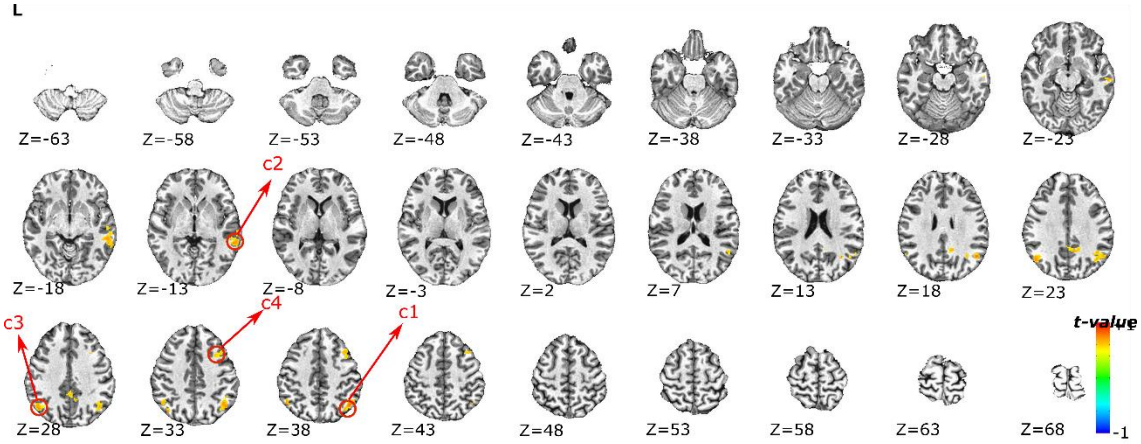


Figure 6-6: Significant clusters for MS-C. Clustering was performed at p<0.005 and corrected at p<0.05.

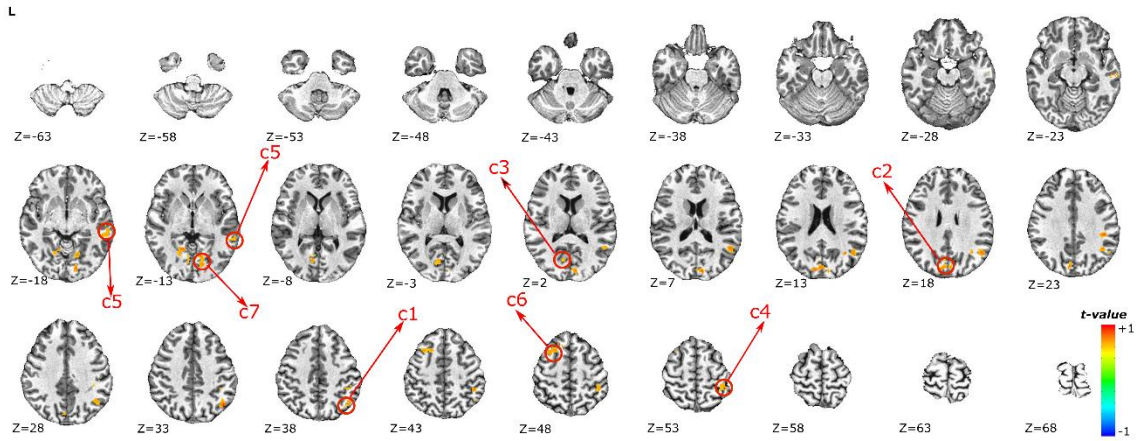


Figure 6-7: Significant clusters for MS-D. Clustering was performed at p<0.005 and corrected at p<0.05.

Table 6-3: Significant clusters from the healthy control group after applying one-sample t-test on the GLM coefficients.

MS	Name	Region	x	y	z
A	C1	Right Lentiform Nucleus	-26	-1	2
A	C2	Left Lentiform Nucleus	28	0	-2
B	C1	Right Cuneus	-2	82	16
C	C1	Left Angular gyrus	47	62	37
C	C2	Left Middle Temporal Gyrus	61	32	-7
C	C3	Right Inferior Parietal Gyrus	-48	65	38
C	C4	Left Middle Frontal Gyrus	38	-17	46
D	C1	Left Angular Gyrus	48	61	31
D	C2	Right Cuneus	-2	85	24
D	C3	Right Lingual Gyrus	-12	70	2
D	C4	Left Postcentral Gyrus	43	39	54
D	C5	Left Middle Temporal Gyrus	60	30	8
D	C6	Right Superior Frontal Gyrus	-27	-18	57
D	C7	Left Lingual Gyrus	14	73	-4

The t-test of FAIR values between HC and the lumped MA subjects is shown in **Figure 6-8** and among subgroups in **Figure 6-9**.

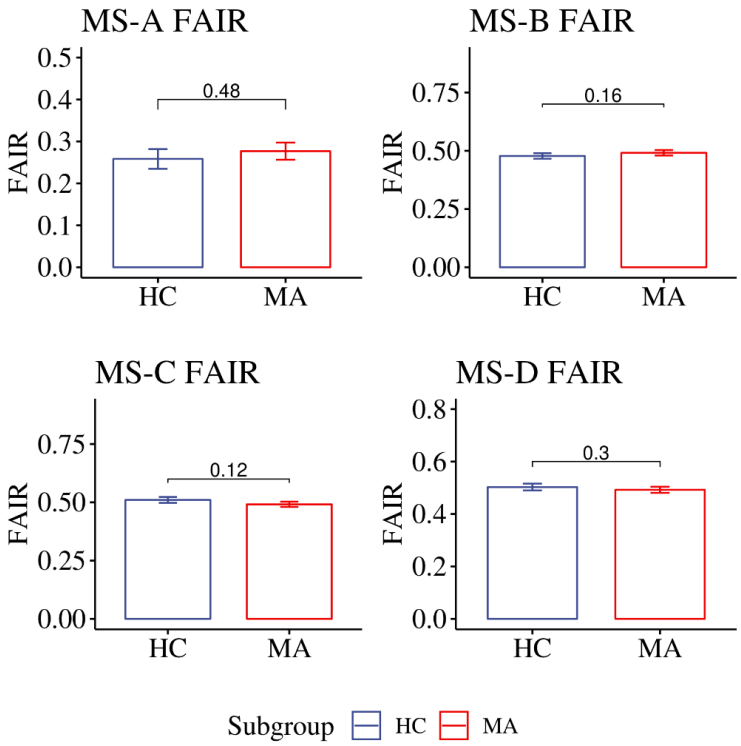


Figure 6-8: Statistical analysis for FAIR metrics between HC and MA subjects. Error bars represent the standard error. The p-value of the t-test is shown at the top of each bar pairs.

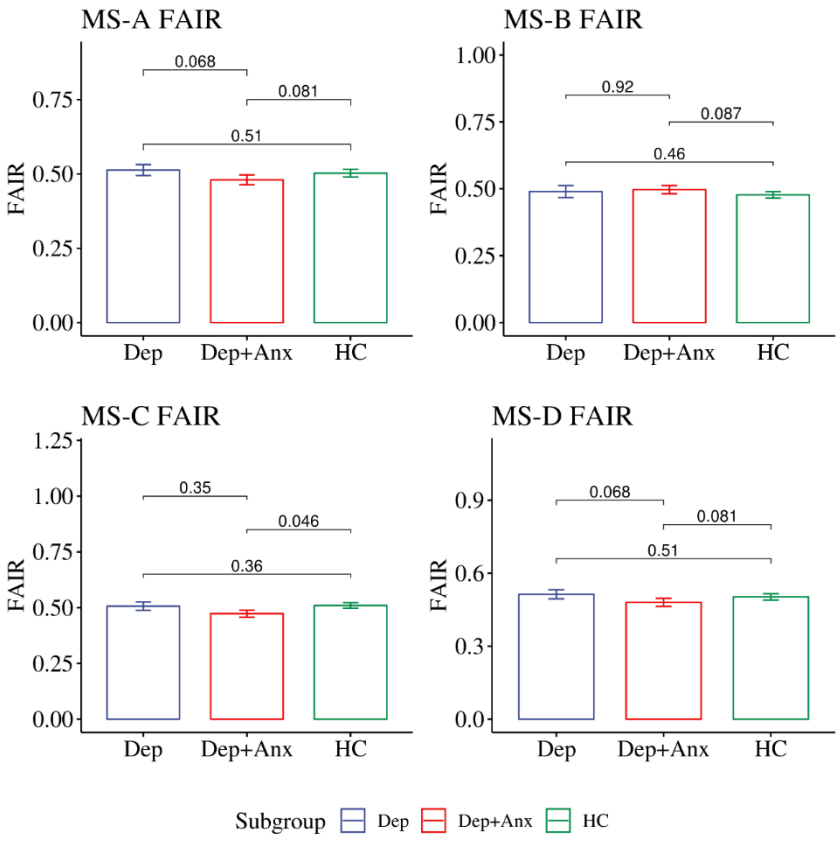


Figure 6-9: Statistical analysis for FAIR metrics between HC and subgroups of MA subjects. Error bars represent the standard error. The p-value of the t-test is shown at the top of each bar pairs.

The t-test of coherence-based FAIR values between HC vs. MA and HC vs. subgroups of MA is shown in **Figure 6-10** and **Figure 6-11**, respectively.

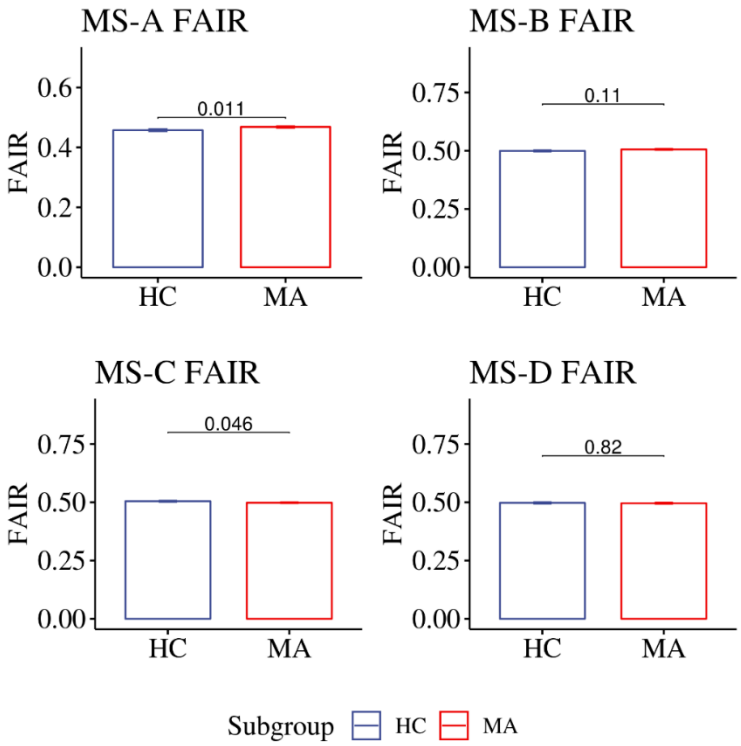


Figure 6-10: Statistical analysis for Coherence-based FAIR metrics between HC and MA subjects. Error bars represent the standard error. The p-value of the t-test is shown at the top of each bar pairs.

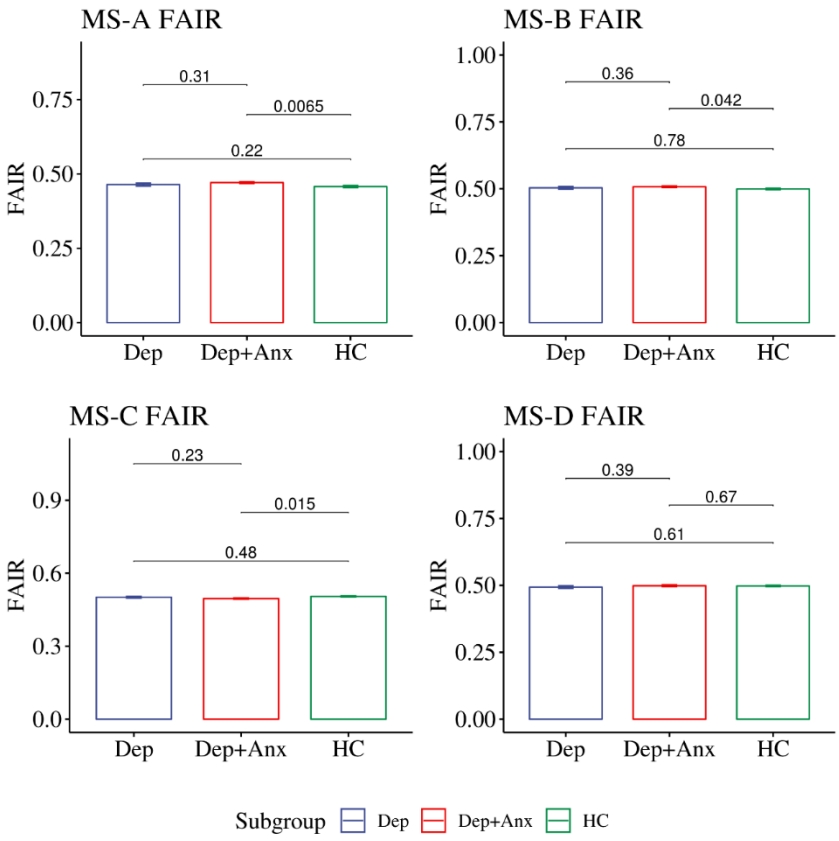


Figure 6-11: Statistical analysis for Coherence-based FAIR metrics between HC and subgroups of MA subjects. Error bars represent the standard error. The p-value of the t-test is shown at the top of each bar pairs.

Similarly, the complex network analysis using graph theory was investigated at different edge densities (i.e., proportional thresholding). **Figure 6-12** reveals graph analysis for HC vs. MA. Besides, **Figure 6-13**, **Figure 6-14** and **Figure 6-15** depict graph analysis results for HC vs. Dep, HC vs. Dep+Anx, and Dep vs. Dep+Anx, respectively.

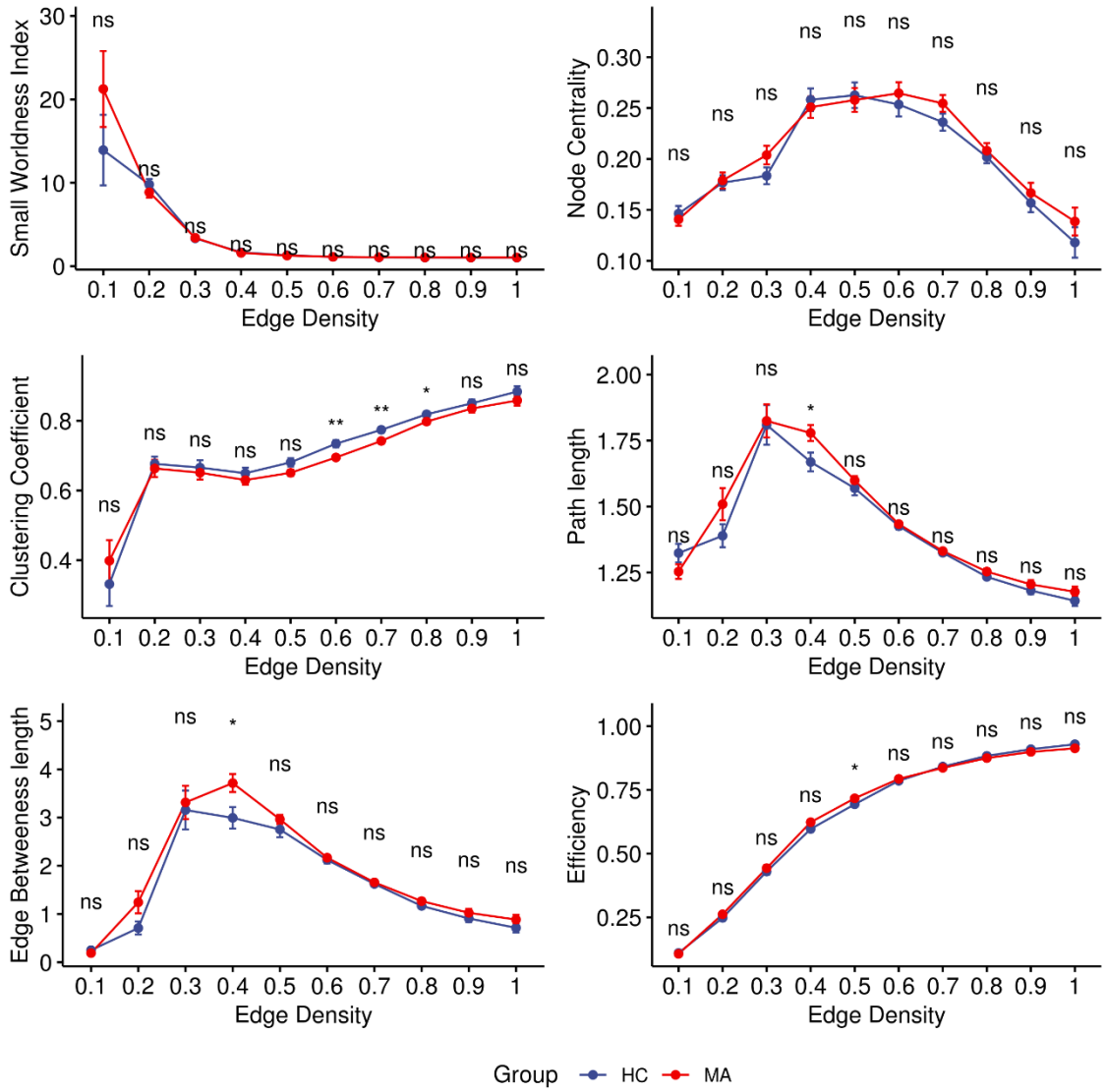


Figure 6-12: Graph analysis for HC vs. MA subjects estimated at different edge densities. The analysis shows the small-worldness index, clustering coefficient, path length, node betweenness, and efficiency (ns: not significant difference, *: $p<0.05$ and **: $p<0.01$).

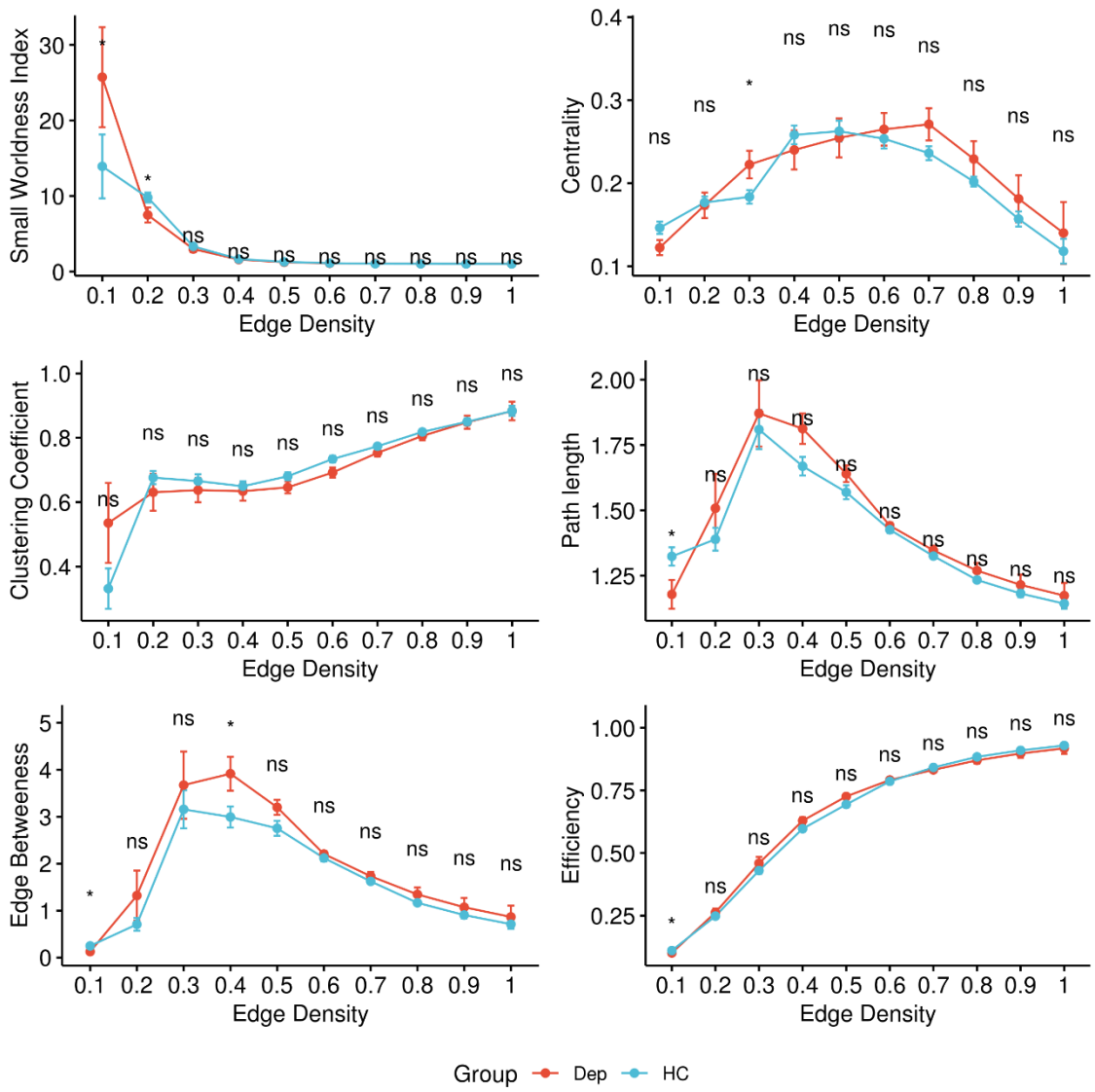


Figure 6-13: Graph analysis for HC vs. Dep subgroups estimated at different edge densities. The analysis shows the small-worldness index, clustering coefficient, path length, node betweenness, and efficiency (ns: not a significant difference, *: $p<0.05$ and **: $p<0.01$).

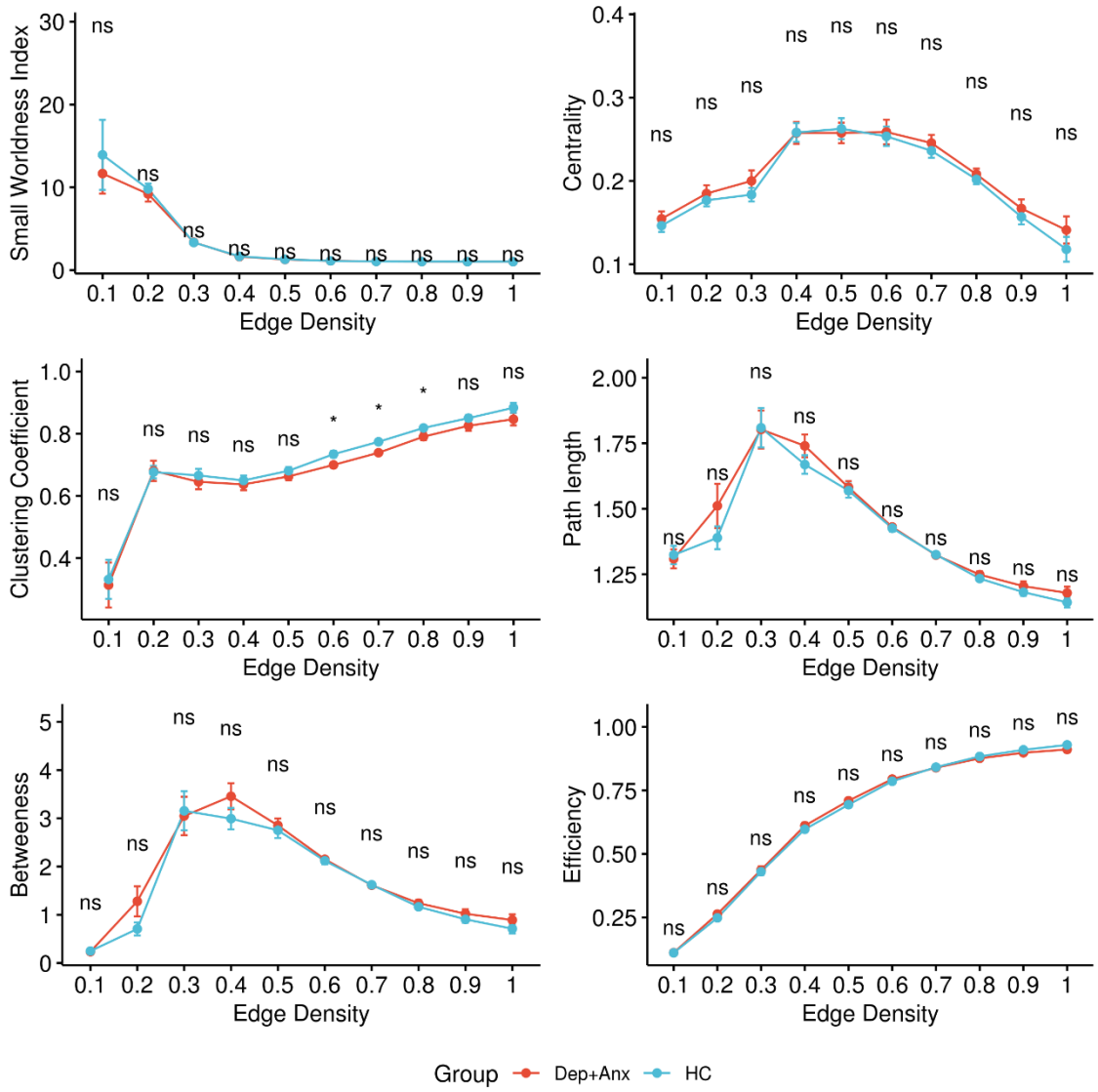


Figure 6-14: Graph analysis for HC vs. Dep+Anx subgroups estimated at different edge densities. The analysis shows the small-worldness index, clustering coefficient, path length, node betweenness, and efficiency (ns: not significant difference, *: $p<0.05$ and **: $p<0.01$).

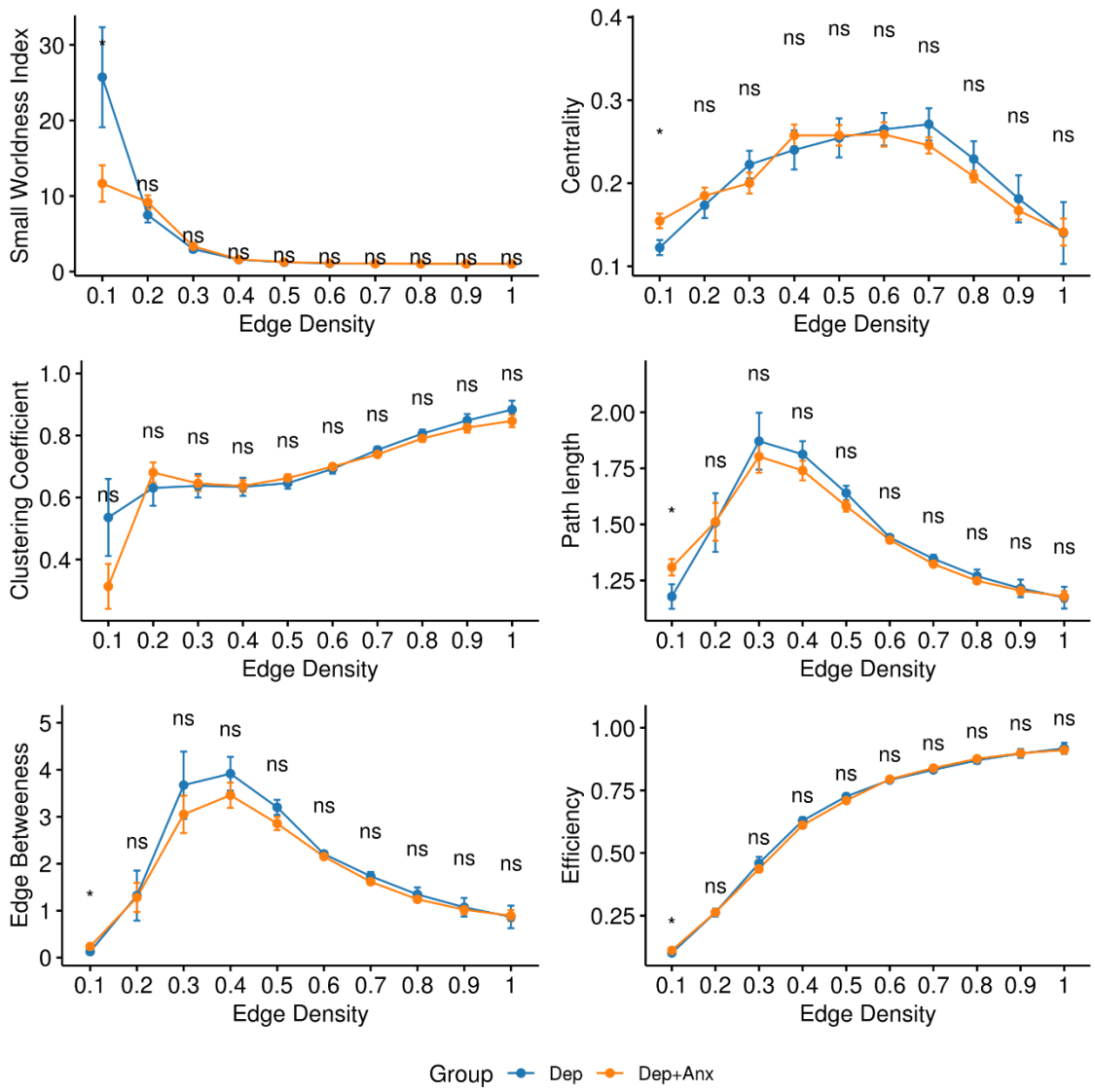


Figure 6-15: Graph analysis for Dep+Anx vs. Dep subgroups estimated at different edge densities. The analysis shows the small-worldness index, clustering coefficient, path length, node betweenness, and efficiency (ns: not significant difference, *: $p<0.05$ and **: $p<0.01$).

6.4.1 Correlation Analysis between EEG-ms Brain Regions Functional Connectivity and Clinical Assessment Measures

FC was propped between brain regions associated with significant connections obtained from results reported in **Chapter 3** (e.g., MS-B to MS-D, MS-B to MS-C, and MS-A-to MS-D) and PHQ measure. Please refer for **Table 6-1** for detailed information about the demographics of the dataset. **Figure 6-16** reveals the correlation between FC of brain regions associated with each significant connection and PHQ. **Figure 6-17** shows the correlation between the coherence measure of brain regions associated with significant connections and PHQ.

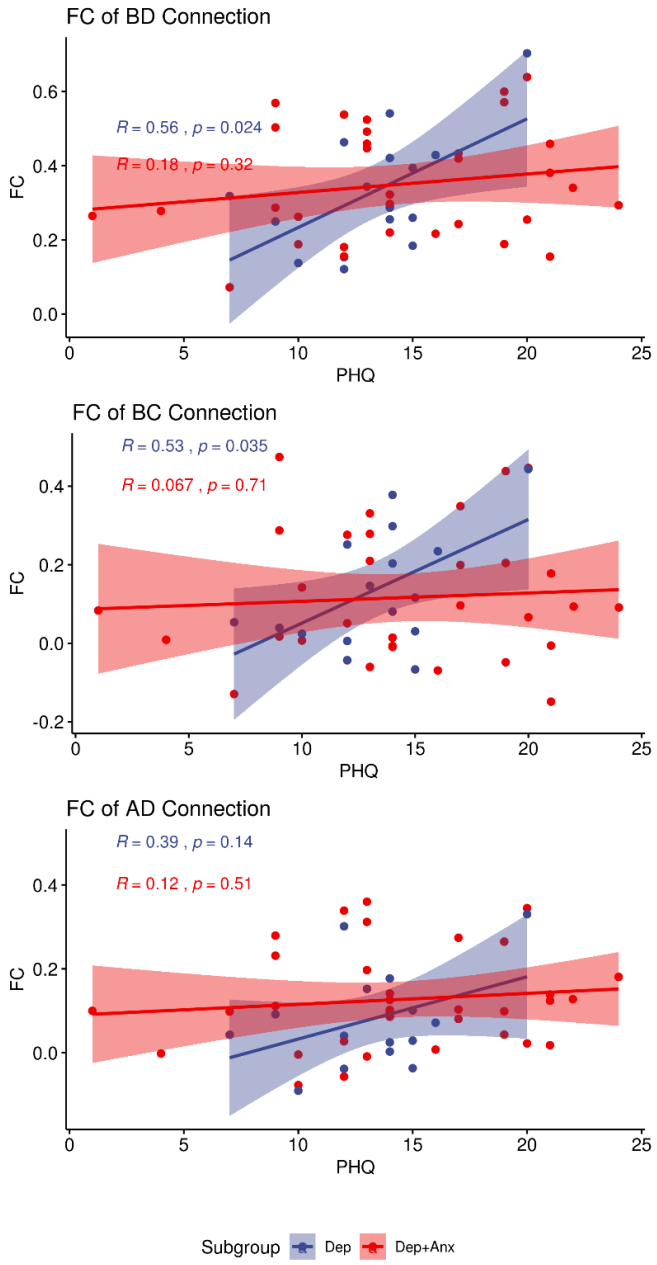


Figure 6-16: Correlation analysis between FC of the brain regions associated with significant connections obtained from Chapter 3 and PHQ.

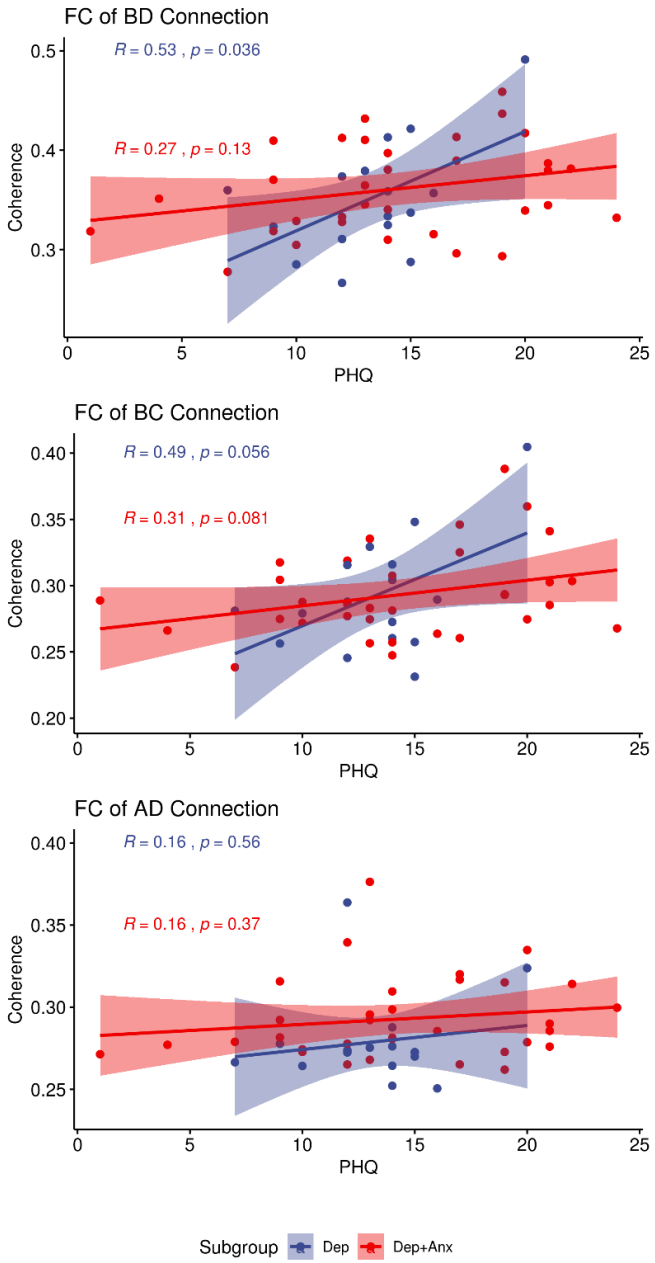


Figure 6-17: Correlation analysis between Coherence of the brain regions associated with significant connections obtained from Chapter 3 and PHQ.

6.5 Discussion

This chapter investigated the use of EEG-ms to inform fMRI analysis and relies on the findings reported in **Chapter 3**, where subjects with MA exhibit alterations in the transition dynamics between EEG-ms when compared with HC. This chapter explores whether brain regions associated with EEG-ms from HC showed any FC alteration. Thus, EEG-ms brain templates from 43 HC subjects were extracted, as follows. First, the GLM model was adopted to associate the time course of each MS with the BOLD signal from each voxel in the brain. Second, significant clusters were identified—after controlling for false positive—from each EEG-ms for HC subjects only and were treated as brain templates. Each MS spanned different brain regions, as shown in **Table 6-3**. Later, the brain regions were used to study FC between MSs using several strategies.

First, the FAIR measure—a global FC measure that quantifies the functional load for each MS—was introduced. One would expect group differences for such a measure; however, significant differences in coherence-based FAIR values of MS-A and MS-C were found when comparing the MA group to the HC group (**Figure 6-10**). Then, an investigation determined whether MA subjects behave differently due to the heterogeneity within the depression cohort, in addition to anxiety symptom comorbidity. MA subjects were further sub-grouped into those with depression (Dep) only and others with depression and anxiety (Dep+Anx). Due to the limited number of subjects with anxiety only (Anx) and Substance+, subgroups were excluded from further analysis. The FAIR values for subgroups were calculated and presented in **Figure 6-9** for FC-FAIR and in **Figure 6-11** for Coherence-based FAIR. The figures demonstrate subgroup differences at HC vs. Dep+Anx for FC-FAIR of MS-C and Coherence-FAIR for HC vs. Dep+Anx in

MS-A, MS-B, and MS-C. It was concluded that comorbidity of symptoms affects the FAIR.

Second, a complex network analysis was conducted using graph theory between EEG-ms brain regions. The analysis investigated several graph theory properties, including SM index, clustering coefficients, path length, node betweenness, and efficiency at different edge densities configurations. The following datasets were assessed: HC vs. MA (**Figure 6-12**), HC vs. Dep (**Figure 6-13**), HC vs. Dep+Anx (**Figure 6-14**), and Dep vs. Dep+Anx. The analysis revealed nothing significant, except for the presence of some edge densities.

Finally, the work in this chapter investigated whether FCs among brain regions associated with connections of the significant difference between MA and HC (**Chapter 3**) was correlated with the PHQ scale (**Figure 6-16** and **Figure 6-17**). The analysis revealed a significant correlation between FC of MS-B and MS-D brain regions and between FC of MS-B and MS-C brain regions.

6.6 Limitations

This chapter detailed EEG-ms information to inform the fMRI analysis. Several strategies were utilized to analyze the data. One of the main challenges is that the brain region associated with EEG-ms are very limited in size and number due to the strict fMRI preprocessing pipeline, which otherwise would question the validity of the results. On the other hand, the association between EEG-ms time course and BOLD might not be linear, as is the assumption of deploying the GLM model.

Nevertheless, 14 brain regions associated with EEG-ms were identified and passed strict preprocessing pipeline. Three brain regions of MS-D were shared with MS-B and MS-C. Moreover, the analysis relied on the fact that there is a group of difference between HC and MA from results detailed in **Chapter 3**; however, those differences were not very pronounced in the fMRI side. This could be due to the limited number of subjects in the MA group, besides the heterogeneity of the population of MA subjects. Thus, increasing the number of samples in both HC and MA might improve the results reported in this chapter.

Furthermore, using additional information from EEG-ms might provide a better approximation for the relationship between EEG and fMRI.

6.7 Conclusions

This chapter deployed EEG-ms features to inform fMRI analysis based on the findings reported in **Chapter 3**. More specifically, EEG-ms time courses were used to localize brain templates of EEG-ms from HC subjects. Then, those brain regions were utilized to study the brain FC of HC and MA subjects. By using the global FC and graph theory analyses, evidence of changes was found in the FC at the level of subgroups of MA subjects. Moreover, Beta coefficients of GLM from the same extracted brain templates were analyzed, and a correlation between PHQ scores and Beta coefficients was found for subgroups of MA subjects.

Chapter 7 : Proposal of a New Approach to Analyze EEG Microstates Data

7.1 Introduction

Replicating findings from previous EEG and fMRI studies has been one of the main challenges in neuroscience and many other fields. This gap is becoming a significant concern for many aspects of research and a necessity for sustaining and building up knowledge from data, especially for human research. There is a consensus about prioritizing the reproducibility of research. Some researchers have gone further to declare a crisis in the reproducibility of results for some domains that include human subjects [184]. Some issues with replicating previous findings are attributed to the gap between the theoretical aspects and practical implementation, in addition to other challenges, such as the presence of noise in data. EEG-ms is not only prone to reproducibility issues; it also suffers from a couple of the practical issues that could significantly affect the reproducibility of results. This can be noticed from the variation in the reported EEG-ms features, even for healthy subjects [56].

Chapter 3 harnessed EEG-ms to differentiate HC subjects from individuals with MA diagnoses. To impact replicability in future studies, this chapter addresses practical issues with conducting EEG-ms analysis and provides suggestions for conducting robust analysis.

Chapter 2 focused on the theoretical foundations of deriving EEG-ms, offering a solid foundation for EEG-ms and, more importantly, pointing out several practical points that were missing from the literature.

This chapter addresses several critical aspects of extracting EEG-ms, including the effect of GFP peak selection and EEG-ms template noise susceptibility, which may impact the reproducibility of EEG-ms results. Based on the presented results in this chapter, several recommendations and guidelines are offered at the end of this chapter.

7.2 Methods

7.2.1 Participants

Please refer to **Chapter 3, Section 3.2.1**. Work reported in this chapter used only HC participants.

7.2.2 EEG Data Acquisition

Please refer to EEG-fMRI data acquisition protocol was explained in **Chapter 1, Section 1.8.**

7.2.3 EEG Data Preprocessing

Please refer to EEG processing procedure used in **Chapter 3, Section 3.2.3.**

7.3 GFP Peaks and Labeling EEG

Labeling EEG points relies on goodness of fit (i.e., similarity) between each EEG point and the corresponding EEG-ms template. As explained in **Chapter 3**, the following equation can be used to assign labels to EEG data:

$$L_i = \underset{k}{\text{argmax}}(abs(f_i)) \tag{7.1}$$

One fundamental assumption about EEG-ms is that assigning EEG-ms depends on the stability of GFP peaks. More specifically, GFP peaks are used as markers to label EEG data points by fixing EEG-ms labels between these peaks. This factor has been used—with or without paying attention to this point as a result of using some software as black boxes—to assign EEG-ms labels without evaluating assignment reliability. The main advantage of using GFP peaks for assigning labels is the high SNR at these data points. However, this approach is challenged with the inter-peak duration of GFP. That is, because EEG-ms average duration is about 50 ms, there might be uncertainty about EEG labels when the inter-peak duration is more than 50 ms. The following figure plots a GFP signal from a sample dataset. Peaks with 50 ms gap or more were marked with orange flipped triangles.

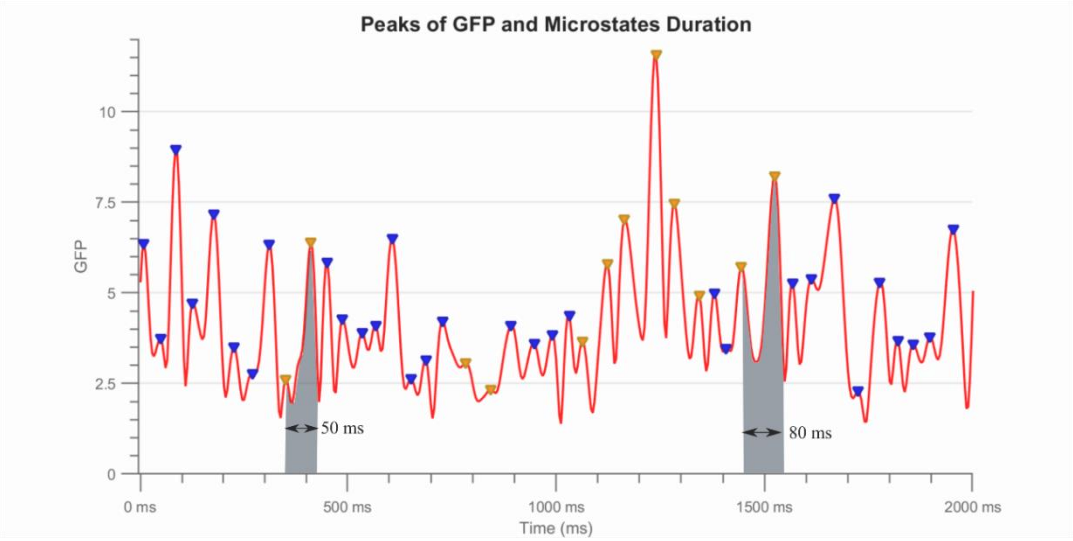


Figure 7-1: An illustrative example of GFP peaks and the gap between peaks.

In order to have a general informed view about the inter-peak duration, **Figure 7-2** shows the distribution of the inter-peak duration for an exemplar EEG signals recording (duration: 8 minutes).

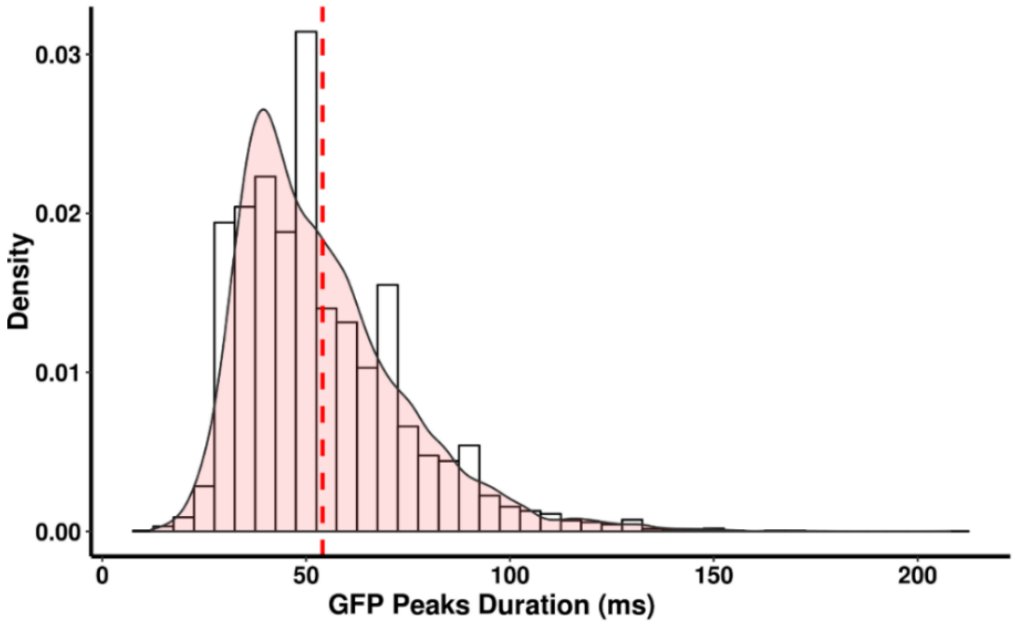


Figure 7-2: Inter-peak distribution from an exemplar dataset.

Similar results were obtained when examining the inter-peak duration from 52 HC subjects used for the study reported in **Chapter 6.** The overall distribution of inter-peak duration from all subjects is depicted in **Figure 7-3**.

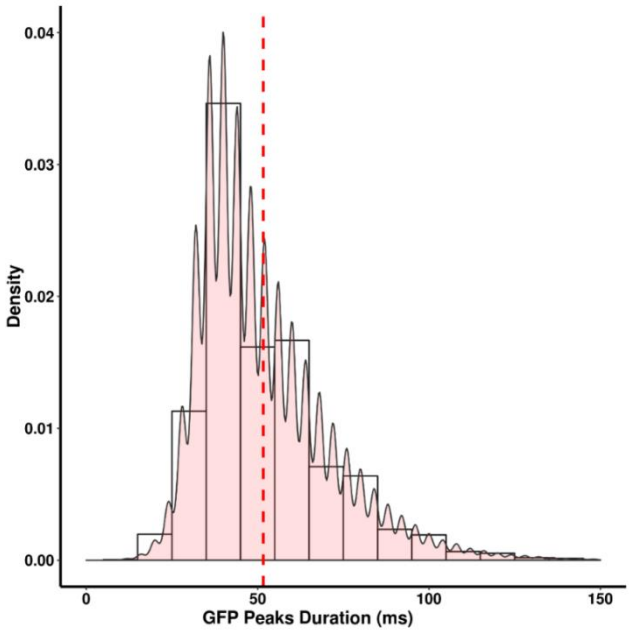


Figure 7-3: Inter-peak distribution taken from 43 HC subjects.

The average inter-peak duration from 43 HC subjects was **51.65 (±19.18**) ms. Thus, there is a significant number of peaks that consist of more than a 50 ms gap, which may result in an overestimation of the average duration of EEG-ms. This can be evidenced by the discrepancies in the reported average duration of EEG-ms classes—also applied to other EEG-ms features—from the literature [54, 165].

7.4 Noise Effects on EEG-ms Templates Similarity and Sensitivity

Another issue with labeling EEG datapoints as EEG-ms is the high similarity among EEG-ms templates, especially between EEG-ms C and D. **Figure 7-4** depicts the correlation among EEG-ms templates extracted from 43 HC subjects—the same EEG-ms

dataset used in **Chapter 6**. Given the high similarity between EEG-ms templates, some EEG points may be assigned to the wrong label when noise is partially contaminating EEG topography at a given point.

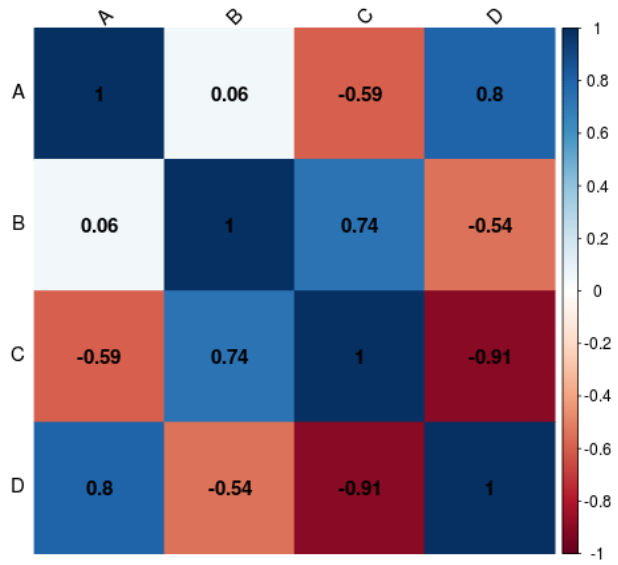


Figure 7-4: EEG-ms templates correlation matrix.

Notably, minor changes in the template might later impact reliable and valid extraction of EEG-ms features. To emphasize this further, different random noise levels were introduced to the EEG-ms templates while relatively reserving their shapes. The noise was drawn randomly from the range [0,1], while controlling for intensity using a noise level factor, which was set between 0 and 0.4, with 0 indicating no added noise. **Figure 7-5** and **Figure 7-6** show the effect of adding noise on the calculated average duration and occurrence of MS-D. Also, the transition probability between MS-C and MS-D was depicted at different noise levels (**Figure 7-7**).

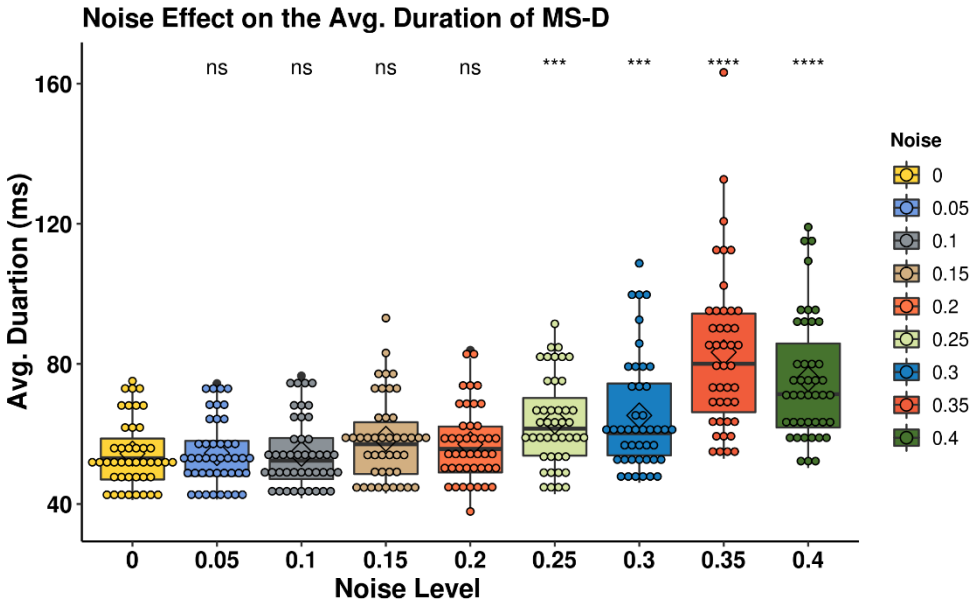


Figure 7-5: Boxplot of noise level effects on the average duration of MS-D (ns: not a significant difference, *: p<0.05, **: p<0.01 and ***:p<0.005).

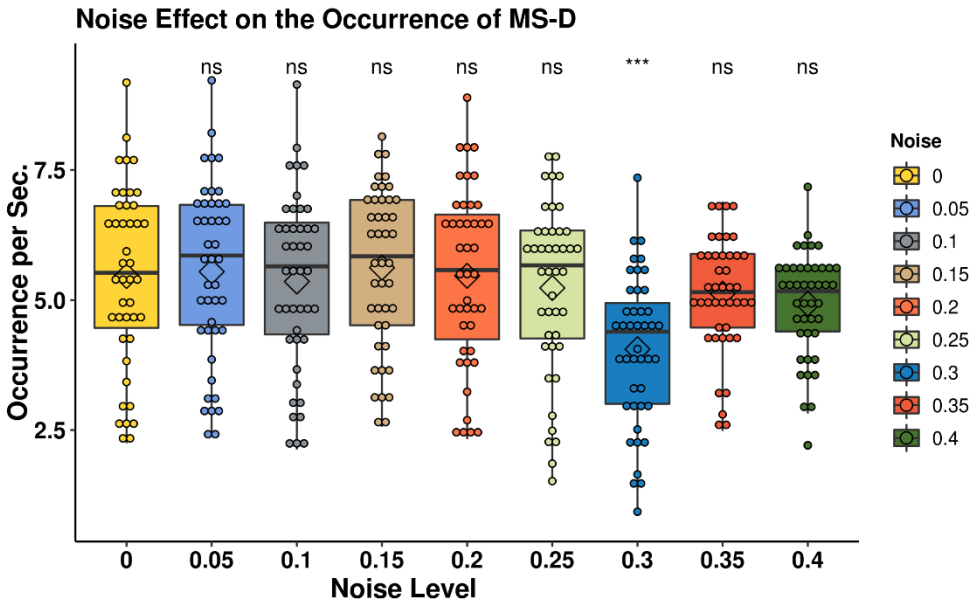


Figure 7-6: Boxplot of noise level effect on the occurrence of MS-D (ns: not a significant difference, *: p<0.05, **: p<0.01 and ***:p<0.005).

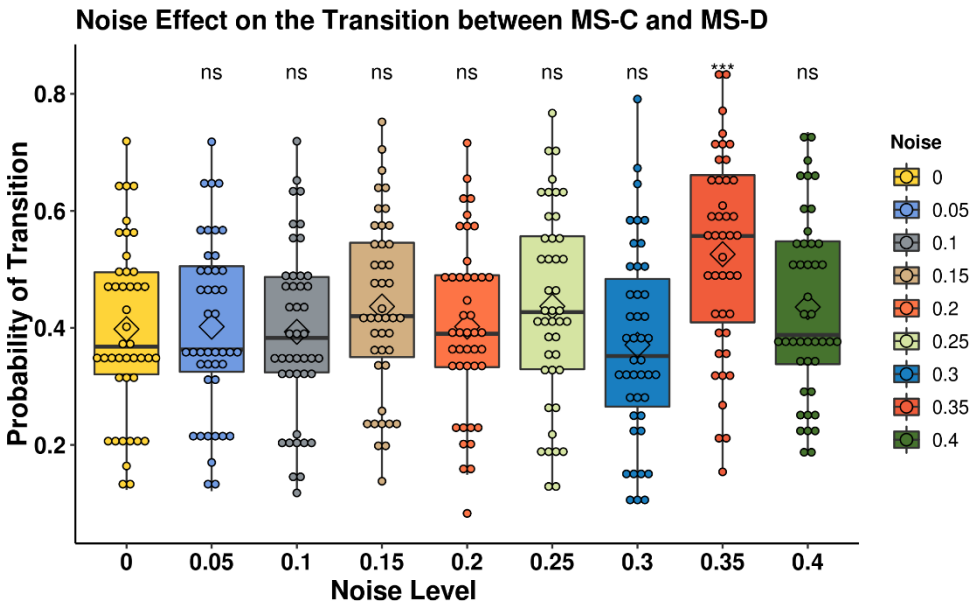


Figure 7-7: The effect of noise level on the transition probability between MS-C and MS-D (ns: not a significant difference, *: p<0.05, **: p<0.01 and ***:p<0.005).

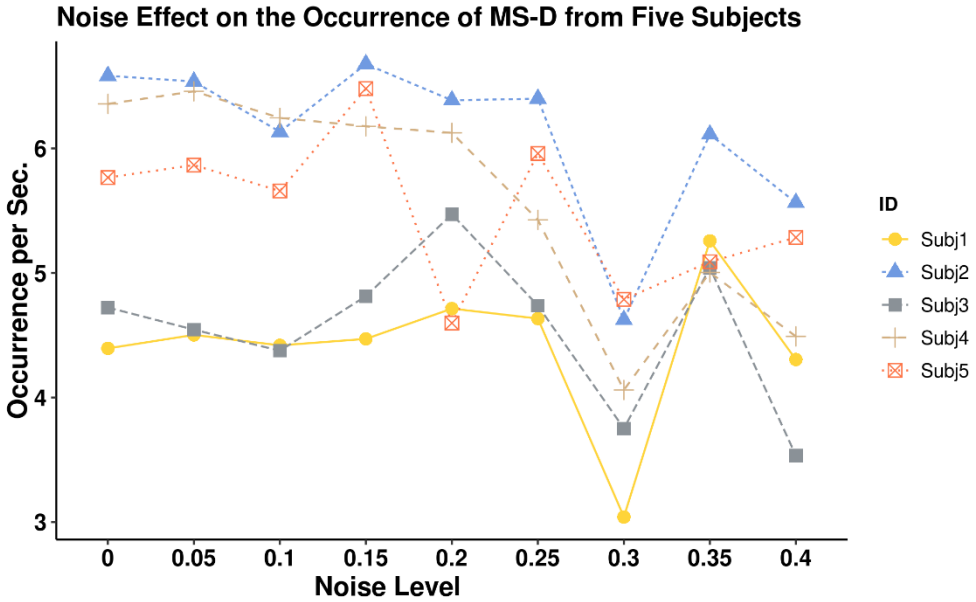


Figure 7-8: An example of the noise effect on MS-D occurrence taken from five randomly selected subjects.

The previous results suggest that the noise level may play a significant factor in altering EEG-ms characteristics. While the EEG-ms templates look similar to the canonical EEG-ms templates, the EEG-ms features were changed. Thus, reproducing EEG-ms templates does not necessarily mean that EEG-ms features are accurately reflecting the data. Moreover, the previous analysis was done within only the HC group. Results may change significantly when comparing two or multiple groups. Inter- and intra-subject noise level may lead to a significant influence on the findings. Nevertheless, EEG-ms showed consistency in EEG-ms characteristics with the level of noise < 0.25.

Another experiment was conducted to show the significant difference between EEG-ms characteristics before and after adding noise. To do so, adding noise was tested with 100 repetitions. The p-value of t-test between the real EEG-ms characteristics (with no noise) and after adding noise was visualized using a Manhattan plot, which demonstrated occurrence of MS-A and MS-D only as examples. For these plots, the level of significance was set to $p<0.05$. **Figure 7-9** and **Figure 7-10** show a significant difference between obtained EEG-ms features when noise is added to the templates. As noted before, MS-C and MS-D might exhibit the most considerable effect due to the similarity between their templates.

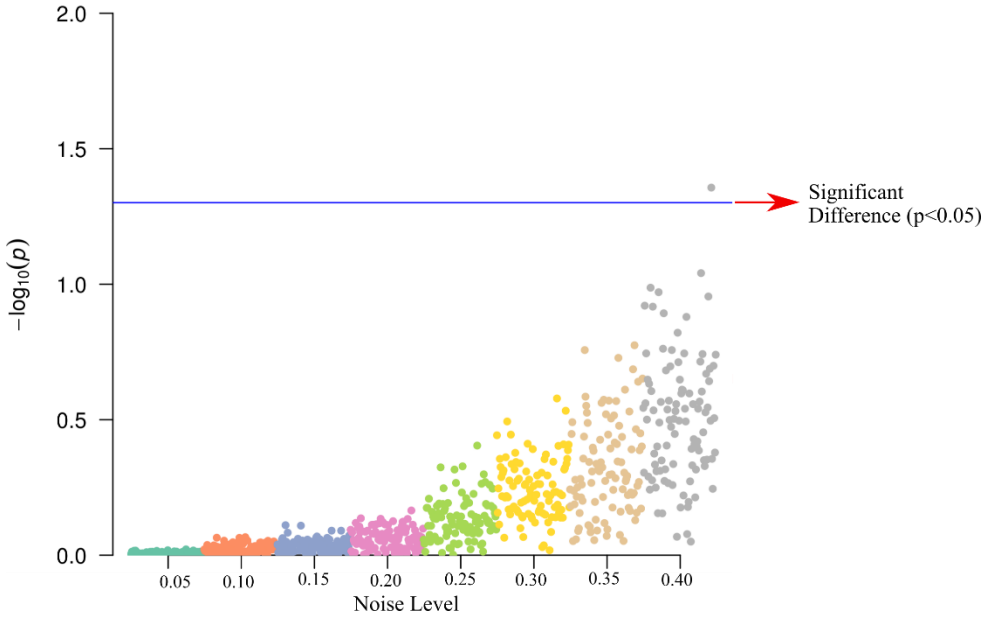


Figure 7-9: The Manhattan plot for the t-test of MS-A occurrence before and after adding noise with 100 repetitions.

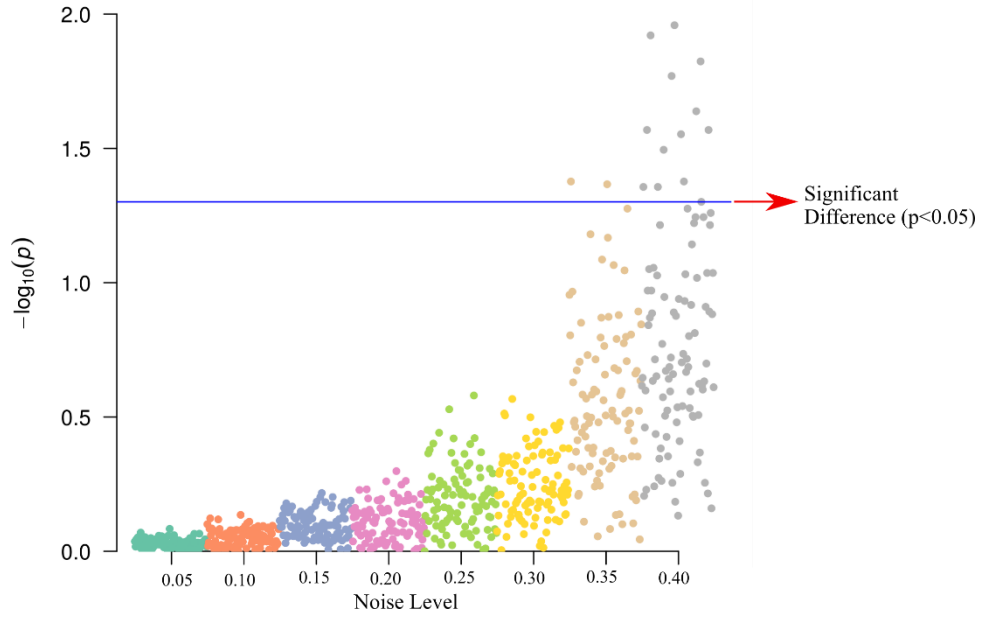


Figure 7-10: The Manhattan plot for the t-test of MS-D occurrence before and after adding noise with 100 repetitions.

7.5 Towards Reproducible EEG-ms Results

In this chapter, the effect of the GFP peak selection was evaluated. From **Figure 7-3**, the average duration of inter-peaks was 53 ms, although larger values of inter-peak duration were observed from the dataset. This could be problematic since labeling EEG data relies on the fact that EEG-ms are stable between peaks. That is, if there is a switch between one MS to another within peaks of GFP, then labeling would never account for the incidence. Hence, EEG-ms characteristics might not correctly represent the entire dataset.

One solution is to use extra points between GFP peaks, given that the duration of inter-peaks is greater than the average duration of EEG-ms classes (i.e., greater than 40 ms). Such a solution might alleviate the effect of the large inter-peak duration. Choosing these extra points can be done based on a distance factor from GFP peaks or can be chosen as points with high SNR.

This chapter also explored the issue of noise presence within EEG-ms template. Results have shown that noise actually affects the estimated EEG-ms features. Although adding noise to the templates did not significantly alter the shape of EEG-ms templates, the EEG-ms features were greatly affected by the presence of noise. Thus, noise inspection is needed even if the EEG-ms template looks similar to the canonical EEG-ms templates.

The previously mentioned problem may suggest using a weighted average of templates from different repetitions of templates extraction. This can be further extended to use ensemble weighted templates from different algorithms to calculate EEG-ms

templates, and then average over all templates. Using modified-k-mean and AAHC for this purpose is suggested.

Both investigated problems—inter-peak duration and EEG-ms features sensitivity to noise—could be alleviated by using a less rigid labeling approach for EEG-ms. Such an approach may use the direct time course of EEG-ms instead of rigid labeling for the data. For example, one may use probabilistic EEG-ms labeling instead of assigning EEG points to only one label at a time (See **Figure 7-11**). Each EEG point is assigned to the four EEG-ms classes with certain probabilities so that overall statistics can be conducted, as in the Bayesian statistics.

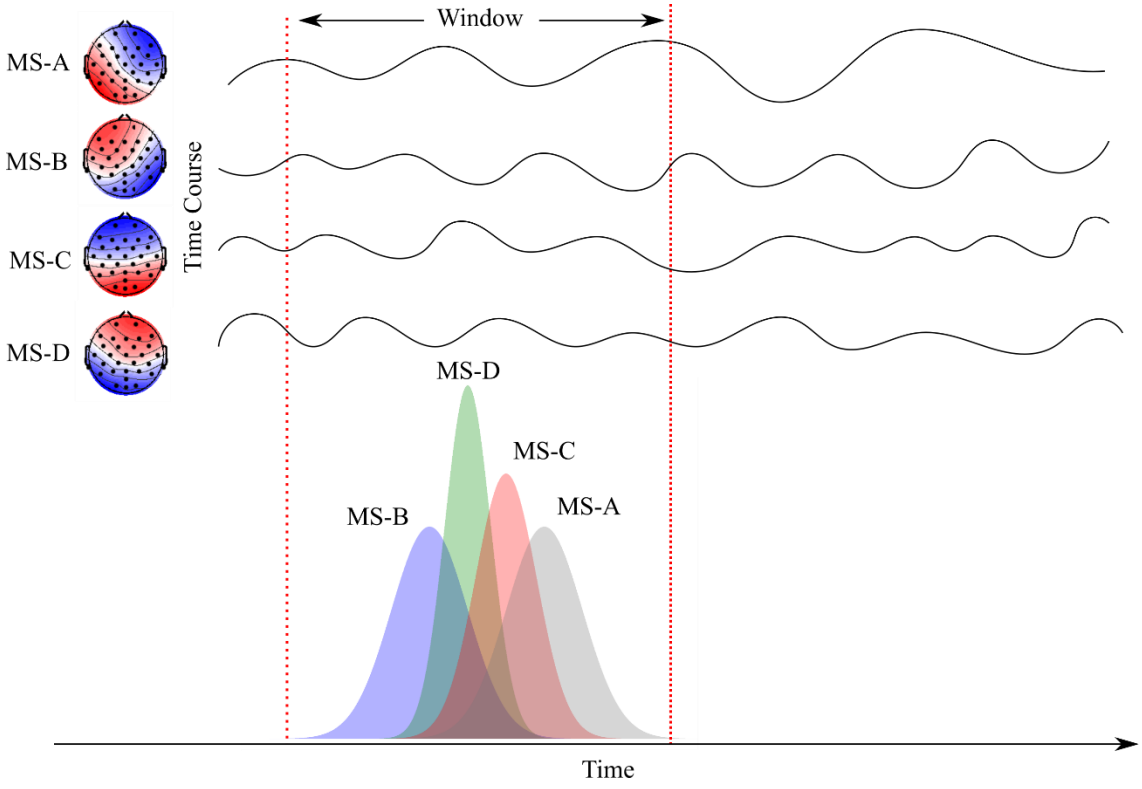


Figure 7-11: An example of the suggested probabilistic EEG-ms assignment.

7.6 Limitations

The carried-out analyses were based on data collected using simultaneous EEG-fMRI recording. Although EEG preprocessing steps were carefully followed to reduce noise and artifacts, there is a chance that some residual imaging and BCG artifacts would remain. Further analysis is required on data collected outside MR scanners. Various levels of added noise was tested, and noise was driven independently from the data. Thus, using data-driven noise factor in addition to studying other types of noise might be needed to offer a comprehensive view about the noise effect.

7.7 Conclusion

This chapter analyzed two main problems for conducting EEG-ms analysis, including oversight in the literature. The effect of both problems on the derived EEG-ms characteristics was shown using several experiments. Based on the studied problems, several suggestions were provided to conduct robust and reproducible EEG-ms analysis.

Chapter 8 : Conclusions and Future Work

This dissertation presented a practical overview and theoretical analysis for the extraction of multiple potential biomarkers of mental disorders from EEG and fMRI data. First, this work elaborated on the practical and theoretical aspects of extracting EEG microstates (EEG-ms) features. Second, the work extracted and tested a set of dynamic EEG-ms features and static EEG features for different purposes. Using these EEG-ms features, the results revealed that the features are potential biomarkers for subjects with mood and anxiety disorders (MA). Specifically, MA subjects have exhibited a systematic alteration in EEG-ms transition probabilities besides an elevation in the temporal dependencies among microstates (MSs). Thus, EEG-ms might be a potential diagnostic approach and basis of evaluating intervention methods.

Third, static features were used to build a general-purpose prediction framework, which was successfully tested for estimating age from EEG (i.e., BrainAGE). This discovery offered a functional biomarker for aging and a potential approach for investigating how mental disorders can affect brain aging. Extracted EEG features were then used to inform fMRI analysis in two projects. The dynamic EEG features were used to inform fMRI analysis for MA subjects, and the results revealed that temporal EEG-ms properties can guide fMRI analysis to show potential fMRI biomarkers for MA subjects. Additionally, the static features were harnessed along with fMRI features to build heterogeneous EEG-fMRI BrainAGE predictors.

This study demonstrated that EEG and fMRI share significant information about aging, but that each modality has its own fingerprint about aging. Finally, this dissertation addressed some concerns about the reproducibility of EEG-ms found to be overlooked in the literature, and then provided guidelines to offer more robust EEG-ms feature extraction.

While the dissertation focused on predicting age from EEG and fMRI, predicting other clinical assessment measures like PHQ, STAI measures, and PROMIS scales was tested. The results (not reported in this dissertation) have shown a low predictability power as compared to predicting age. This is may be attributed to the variability of how mental disorders affect the brain and due to other intra-subject variability factors. Thus, predicting other clinical assessment scales from neuroimaging data is still a challenge and requires more careful optimistic view of using ML to predict those scales.

In summary, extracting and reconciling informative features from EEG and fMRI are an essential step in building clinically translatable biomarkers for characterizing different mental illnesses. With the advent of novel Machine Learning (ML) and computational methods, robust biomedical features pave the way to leverage knowledge about the underlying mechanisms behind mental illnesses.

8.1 Future work

This dissertation provided a general overview of potential EEG features for differentiating HC individuals from those diagnosed with MA. Applying the same procedure to other clinical populations might help to identify and characterize different mental disorders, in turn enhancing specificity and sensitivity to predict symptom severity

and differentiate treatment outcomes. Moreover, this work used EEG features to build BrainAGE predictors with a focus on methodological issues while providing a neuroscience-friendly scheme. The framework can be extended to study how mental disorders affect BrainAGE. Also, the same framework can be used to predict other responses, such as some clinical assessment scales of mental disorders, if there is enough information in the feature space. Although we found low predictability power of clinical assessment scales (not reported in this dissertation), this should not prevent any attempts to predict clinical assessment scales with more extensive feature extraction methods.

Furthermore, this work showed how EEG-ms could inform fMRI patterns within depressed individuals with and without comorbid anxiety. The narrative elaborated on the technical and practical issues of using EEG-ms to inform fMRI. The same procedure applied here can be extended and applied to other clinical groups. Information unraveled in the multimodal EEG-fMRI BrainAGE demonstrates the benefit of combining both modalities to understand shared content about BrainAGE. Extending the framework to other responses (e.g., clinical assessment scales) might offer valuable information about how responses are manifested in EEG and fMRI. The narrative in **Chapter 7** provided several suggested guidelines for conducting robust EEG-ms analysis. Further analysis and testing are required to benefit from the offered suggestions. Finally, using combined EEG and fMRI analysis can be used to model the relationship between EEG and fMRI; hence, substitute expensive fMRI features with portable, cheap, and robust EEG features.

.

Appendix A

Instruments for Clinical Symptoms Assessments

- The PHQ-9 [185] is a nine-question instrument with a two-week time frame (based on diagnostic criteria of depression from DSM-IV), given to patients in a primary care setting to screen, diagnose, and measure the severity of depression. Each item on the measure is rated on a four-point scale (e.g., "0" =Not at all to "3" =nearly every day). Total score can range from 0 to 27, wherein a higher score indicates greater severity of depression.
- The Rumination Response Scale (RRS) [186] is a 22-question assessment of depressive thoughts and responses, which focuses on the self, symptoms, and possible causes/consequence of associated mood. Each question consists of scale ranging from 1 (rarely) to 4 (almost always). The RRS has been shown to be a reliable and valid measure with an internal consistency of ($\alpha = 0.93$).
- The State-Trait Anxiety Inventory (STAI) has 20 items for assessing state anxiety and 20 items for assessing trait anxiety [187]. The State Anxiety Scale (S-Anxiety) screens and measures the current state of anxiety, asking how respondents feel "right now," using questions that measure subjective feelings of apprehension, nervousness, tension, worry, and activation/arousal of the autonomic nervous system. The Trait Anxiety Scale (T-Anxiety) evaluates relatively stable aspects of

"anxiety proneness," consisting of general states of calmness, confidence, and security. A higher score indicates more considerable anxiety.

- The Patient-Reported Outcomes Measurement Information System Anxiety (PROMIS_Anxiety) questionnaire includes 29 items with a seven-day time frame and a five-point scale (e.g., "1"=Never; "5" = Always) [188, 189]. Comprehensive mixed methods were used for developing the item bank [190] by focusing on fear, anxious misery, hyperarousal, and some somatic symptoms related to arousal.
- The PROMIS_Depression scale consists of four items and asked participants how often in the last seven days they had experienced depression, including feeling hopeless, worthless, helpless, or depressed [188]. These items are scored the same way as PROMIS Anxiety on a five-point Likert scale ranging from 1 to 5.

Generalized Linear Model Analysis

Model Description

*Transition probability ~ Group * Symptom + Age + Gender*

GLM was run for each connection (transition probability or y in the model) and symptom independently using the "lme4" package from R [191]. Estimated coefficient and p-values were reported. Results are presented in supplementary **Table A4**.

Supplemental Tables

Demographics

Table A1. Demographic information of Chapter 3.

	HC	MA
Gender		
Female	28	38
Male	24	23
Age (yr)		
Range	32(11)	34 (12)
Education (level)*		
Levels of Studying	6.73 (1.67)	6.27 (1.62)
PHQ_9		
Score	0.73 (1.08)	13.26 (5.05)
STAI_State		
Score	26.34 (6.10)	46.11 (11.01)
STAI_Trait		
Score	28.65 (7.13)	52.7 (11.51)
PROMIS_Anxiety		
Total Score	46.55 (7.68)	61.96 (6.64)
PROMIS_Depress		
Total Score	44.54 (6.48)	61.06 (7.41)

Note: PHQ-9 = Patient Health Questionnaire-9; STAI = State-Trait Anxiety Inventory; PROMIS = Patient-Reported Outcomes Measurement Information System. Values outside parentheses are means and values in parentheses are standard deviations.

*Levels of Studying are assigned as follows:

- No schooling completed -> 1
- Nursery school -> 1
- Kindergarten -> 1
- Grade 1 through 11 -> 2
- 12th grade (no diploma) -> 3
- Regular high school diploma -> 4
- GED or alternative credential -> 5
- Some college credit, but less than 1 year of college credit -> 6
- 1 or more years of college credit, no degree -> 6

- Associate's degree (for example: AA, AS) -> 7
- Bachelor's degree (for example: BA, BS) -> 8
- Master's degree (for example: MA, MS, MEng, MEd, MSW, MBA) -> 9
- Professional degree beyond a bachelor's degree (for example: MD, DDS, DVM, LLB, JD) -> 10
- Doctorate degree (for example: PhD, EdD) -> 11

Studies reporting EEG -ms association with BOLD resting state brain networks

Table A2: MS- A and MS-B with the related RSNs reported by previous studies.

MS	**A**	**B**
[24]	RSN 1	RSN 2
[1]	RSN 4	RSN 3
[2]	RSN 'G'	RSN 'E'
Brain Regions Involved	Best matches regions in auditory-phonological system processing network	Primarily involves Visual Network (VN)

Table A3: MS- C and MS- D with the related RSNs reported by previous studies.

MS	**C**	**D**
[24]	RSN 3	RSN 4
[1]	RSN 6 (Partially)	RSN 2
[2]	-	RSN 'C'
Brain Regions Involved	A network that involves medial-ventral prefrontal cortex, the pregenual anterior cingulate, the hypothalamus, and the cerebellum self-referential mental activity.	The dorsal attention network mediating (DAN)

Note: RSN = BOLD resting state network.

Results of GLM analysis modeling group and symptom interactions accounting for age and gender

Table A4. The GLM analysis for the interaction between group and symptoms.

Connection	Scale measuring symptom	Group	Symptom	Age	Gender	Interaction (Group and Symptom)
TP (B → D)	PHQ-9	-0.099	-0.034	-0.002	0.014	0.036
	p-value	***0.037***	***0.046***	*.113*	*.534*	***0.040***
TP (B → D)	STAI_State	-0.295	-0.008	-0.001	0.015	0.009
	p-value	***0.003***	***.004***	*.204*	*.495*	***0.005***
TP (B → D)	STAI_Trait	-0.258	-0.004	-0.001	0.010	0.006
	p-value	***0.014***	*0.100*	*.149*	*.664*	***0.047***
TP (B → D)	PROMIS_Anxiety	-0.017	0.002	-0.001	0.006	-0.001
	p-value	*.924*	*0.297*	*.154*	*.797*	*0.698*
TP (D → B)	PHQ-9	-0.114	-0.018	0.001	0.025	0.019
	p-value	***0.022***	*0.308*	*.159*	*.311*	*0.284*
TP (D → B)	STAI_State	-0.331	-0.010	0.002	0.030	0.010
	p-value	***0.001***	***0.001***	*.073*	*.191*	***0.003***
TP (D → B)	STAI_Trait	-0.314	-0.007	0.002	0.025	0.008
	p-value	***0.004***	***0.006***	*.143*	*.290*	***0.010***
TP (D → B)	PROMIS_Anxiety	-0.388	-0.007	0.002	0.030	0.007
	p-value	***0.033***	***0.004***	*.073*	*.200*	***0.045***

Note: PHQ-9 = Patient Health Questionnaire-9; STAI = State-Trait Anxiety Inventory; PROMIS = Patient-Reported Outcomes Measurement Information System. TP stands for the transition probabilities between two MSs. Numbers in the upper row indicate the beta coefficient of the GLM model, and bold numbers in a lower row indicate significant *p*-values.

Appendix B

This appendix contains information to support findings in **Chapter 4**.

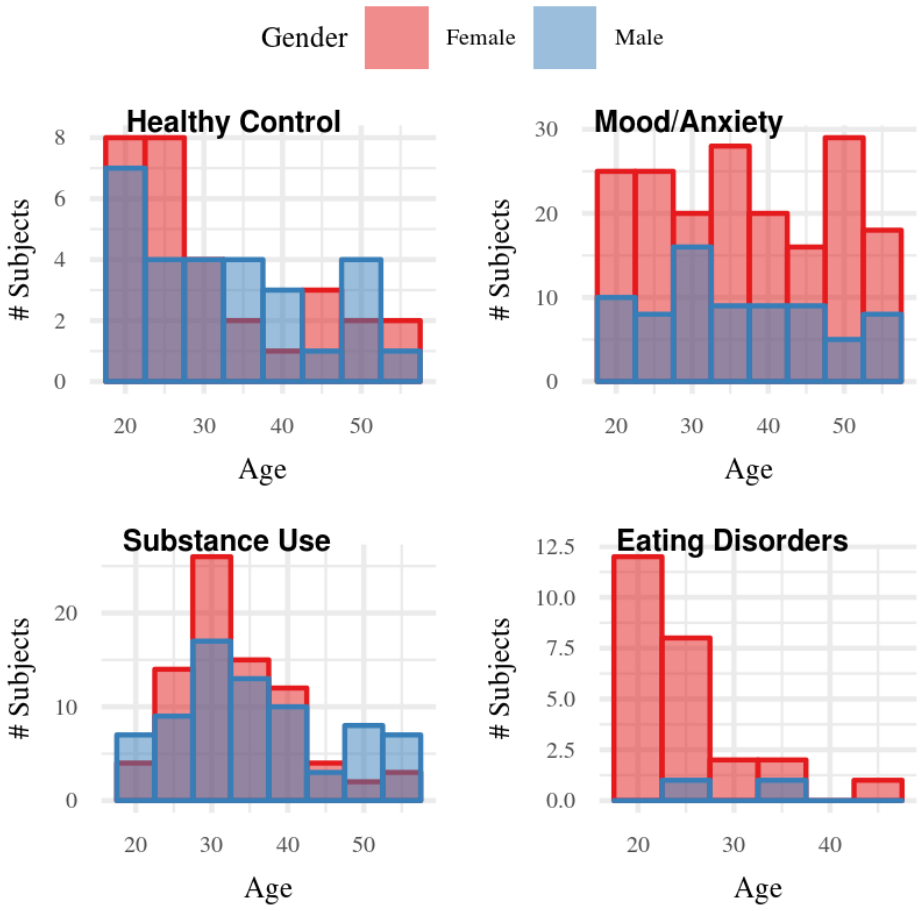


Figure B1: Histogram for the dataset divided based on groups and gender.

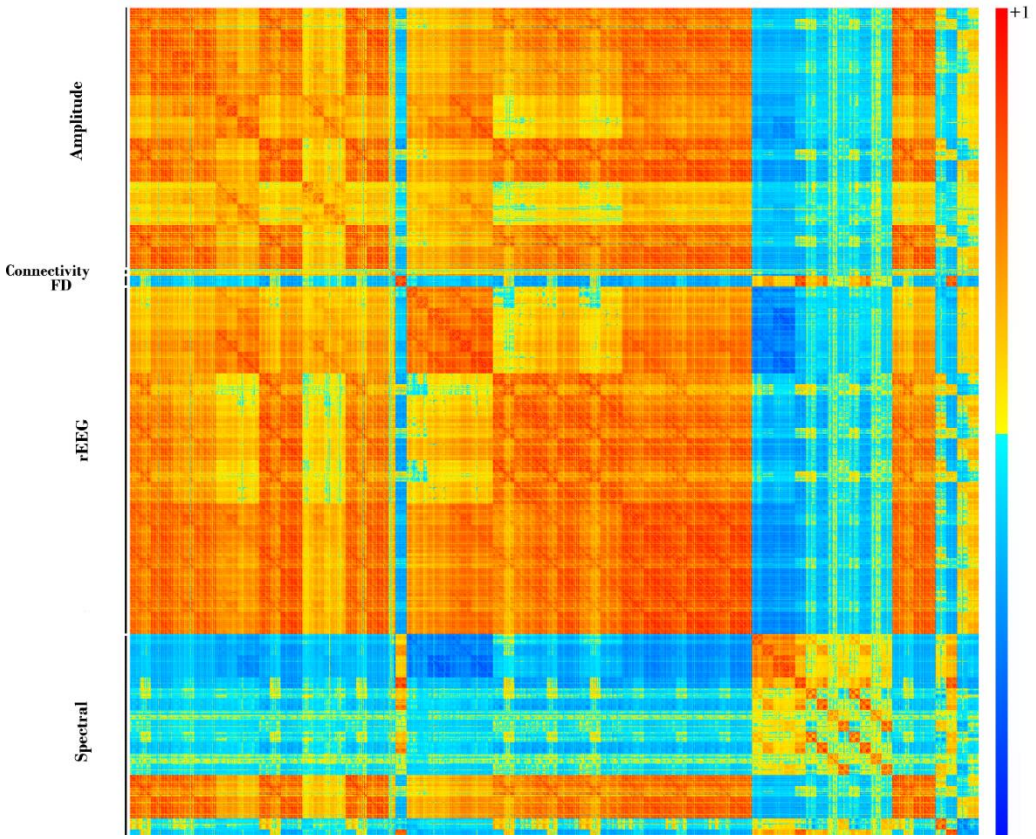


Figure B2: Correlation matrix for all features (before removing correlated features) arranged by feature type.

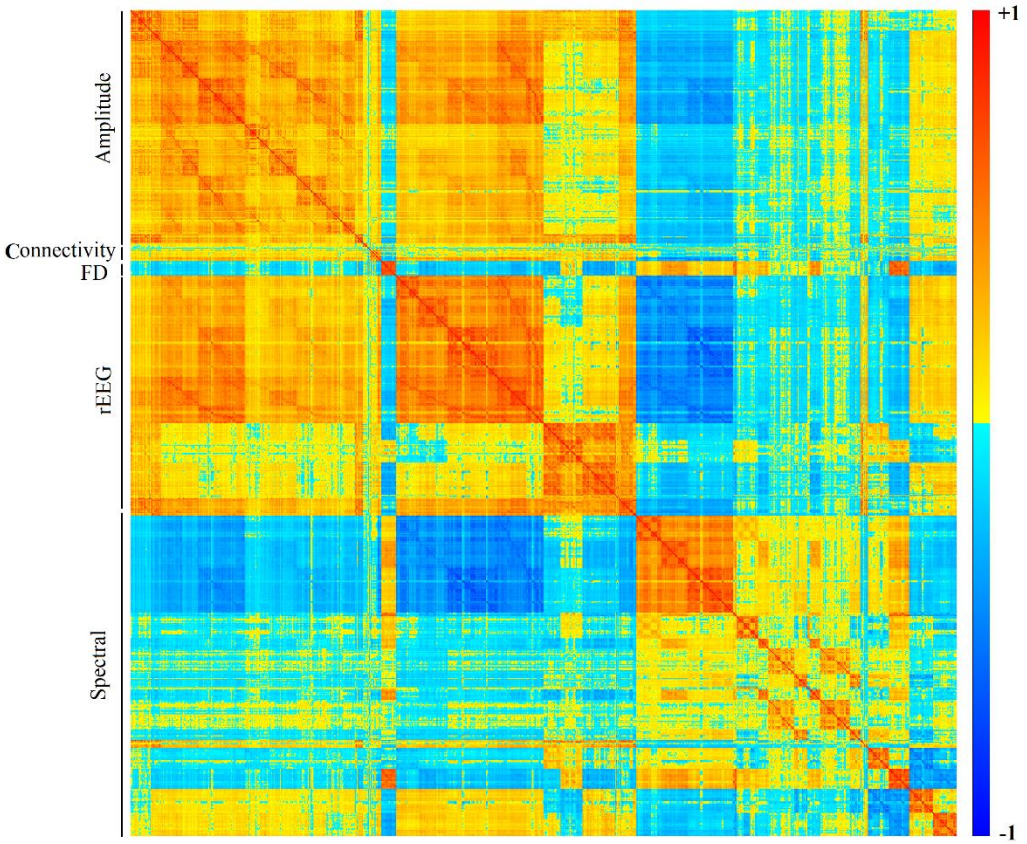


Figure B3: Correlation matrix for features (after removing correlated features: Thr=0.9) arranged by feature type.

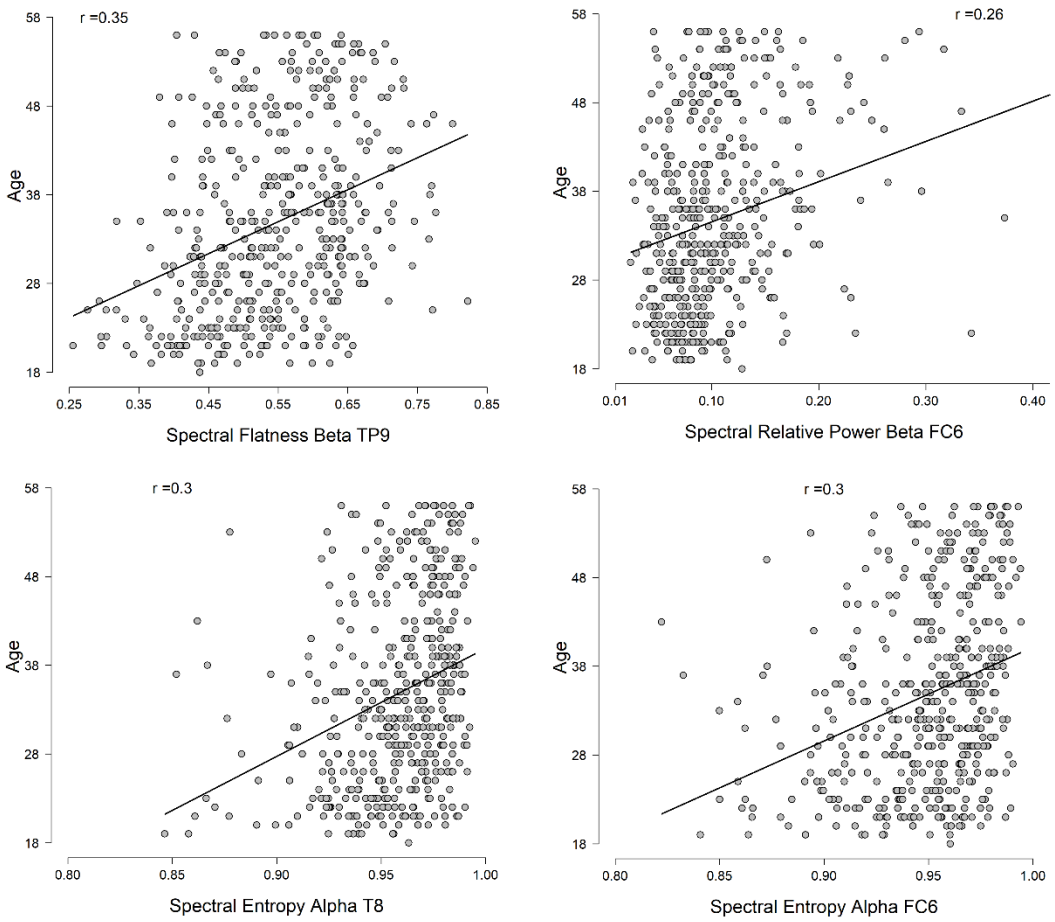


Figure B4: Top features correlation with age.

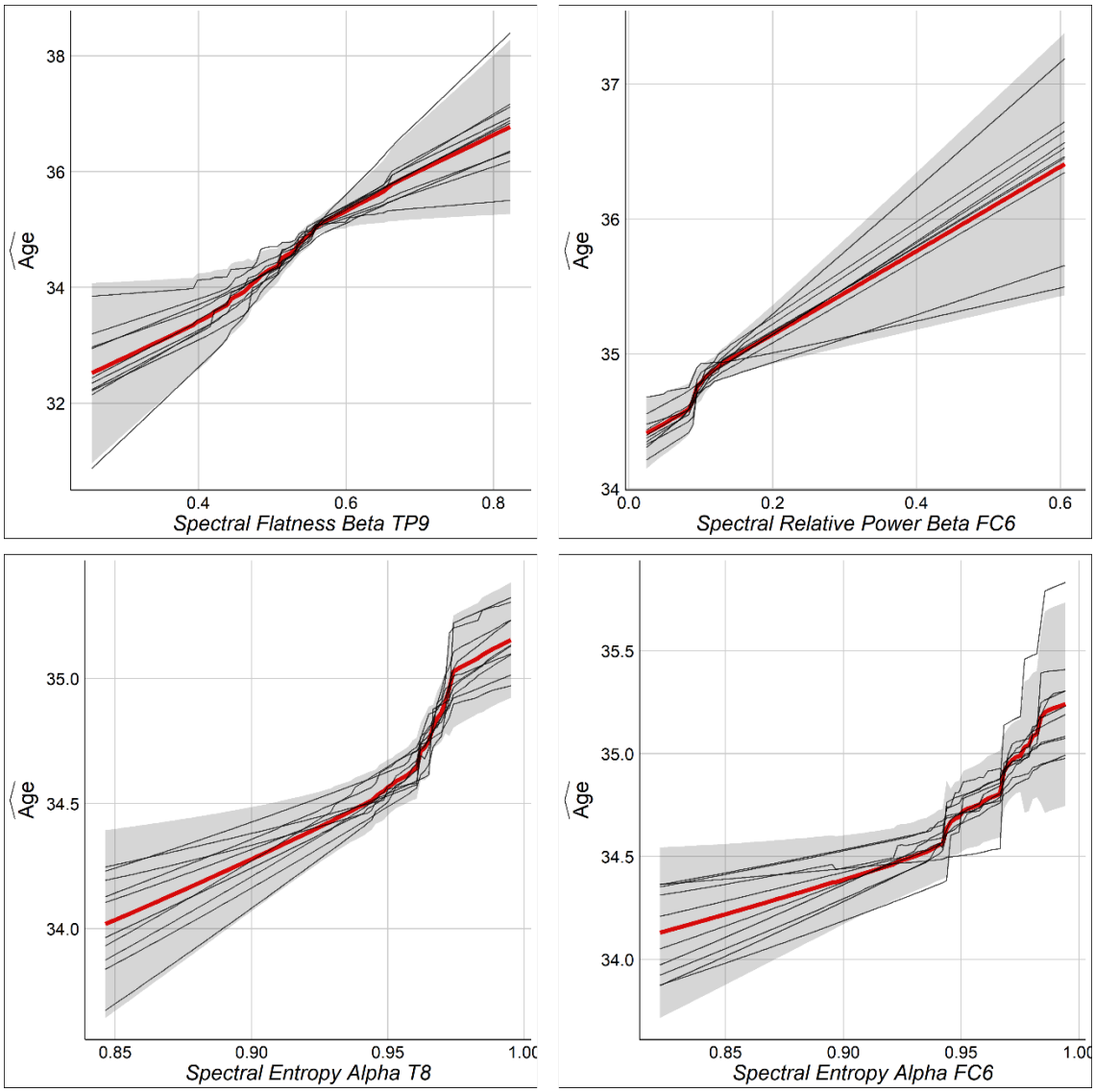


Figure B5: The PDPs from Stack-Ensemble model for the top features. The red line represents the average values over the folds of NCV, while the thin lines are the individual PDPs for each fold.

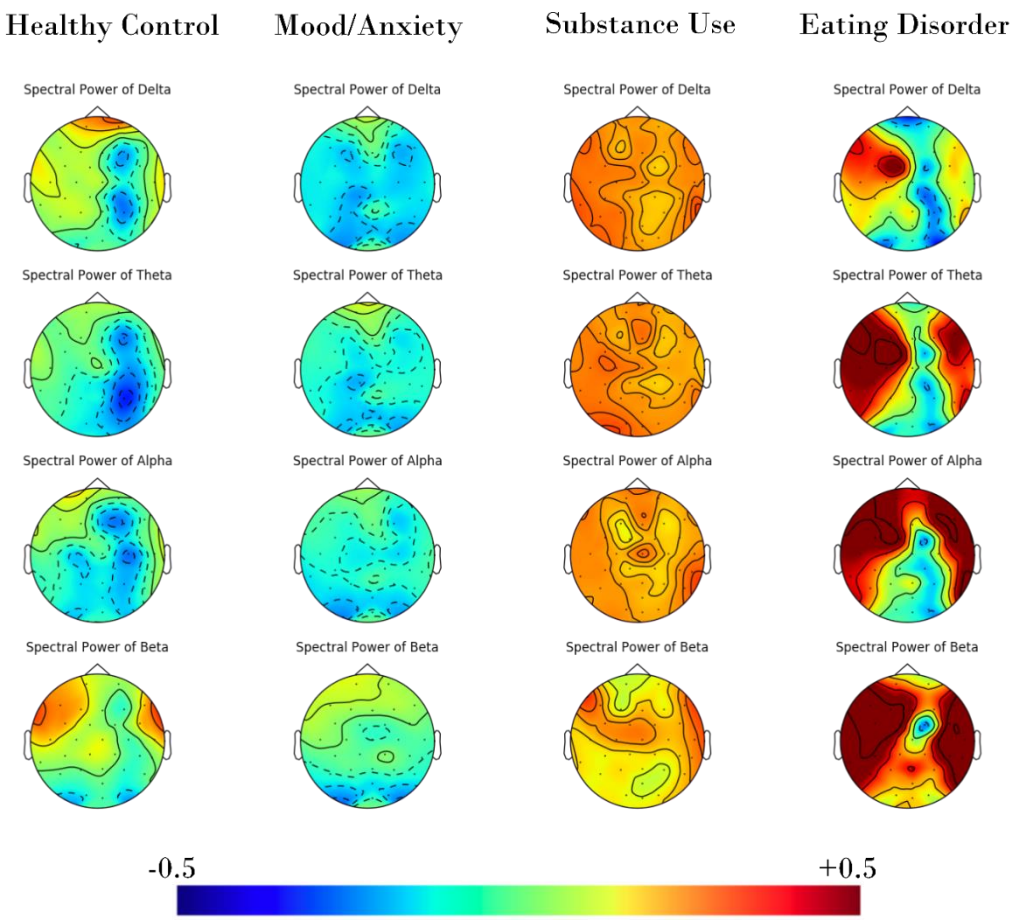


Figure B6: The correlation between spectral power feature and chronic age across different frequency bands and groups.

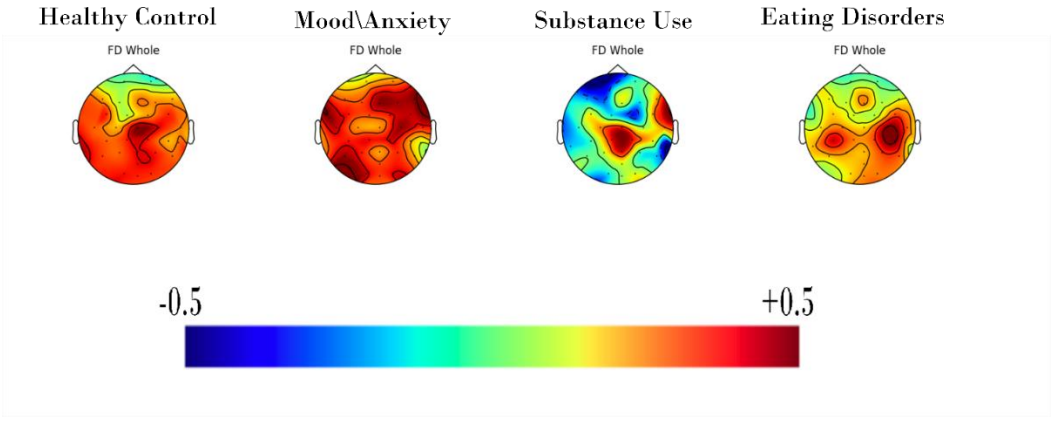


Figure B7: The correlation between FD feature and chronic age across groups for the entire EEG frequency.

Glossary of Terms

Term	Description
AAHC	Agglomerative Hierarchical Clustering
AFNI	Analysis of Functional NeuroImages
AIF	Autoinformation
ALFF	The amplitude of low-frequency fluctuation
Anx	Anxiety
Dep+Anx	Depression+ Anxiety
BCG	Ballistocardiogram
BOLD	Blood-oxygen-level-dependent
BrainAGE	Brain Age
Dep	Depression
DMN	Default Mode Network
DSM	Diagnostic and Statistical Manual of Mental Disorders
DTI	Diffusion Tensor Imaging
EEG	Electroencephalography
EEG-ms	EEG Microstates
ENET	Elastic Net
FC	Functional Connectivity
FD	Fractal Dimension
fMRI	functional Magnetic Resonance Imaging
gaussprPoly	The Gaussian process with polynomial kernel
GFP	Global Field Power
GLM	General Linear Model
HC	Healthy Control subjects/group
HRF	Hemodynamic Response Function
ICA	Independent Component Analysis

MA	Mood and Anxiety Disorder
MAE	Mean Absolute Error
ML	Machine Learning
MRI	Magnetic Resonance Imaging
MS	Microstate
NCV	Nested-cross-validation
OASIS	Overall Anxiety Severity and Impairment Scale
PDP	Partial Dependence Plot
PHQ	Patient Health Questionnaire
RDoc	Research Domain Criteria
RF	Random Forest
RMSE	Root Mean Square Error
ROI	Region of Interest
RSN	Resting State Network
SM	Small-Worldness
SNR	Signal to Noise Ratio
SVM	Support Vector Regression
T-1000	Tulsa 1000 Study
TP	Transition Probability between microstates
TR	Repetition Time
XgbTree	Extreme Gradient Boosting Tree
ACF	Autocorrelation Function

References

[1] D. Mantini, M. G. Perrucci, C. Del Gratta, G. L. Romani, and M. Corbetta, "Electrophysiological signatures of resting state networks in the human brain," *Proceedings of the National Academy of Sciences,* vol. 104, no. 32, pp. 13170-13175, 2007.

[2] J. Damoiseaux, S. Rombouts, F. Barkhof, P. Scheltens, C. Stam, S. M. Smith, and C. Beckmann, "Consistent resting-state networks across healthy subjects," *Proceedings of the national academy of sciences,* vol. 103, no. 37, pp. 13848-13853, 2006.

[3] L. Pauling and C. D. Coryell, "The magnetic properties and structure of hemoglobin, oxyhemoglobin and carbonmonoxyhemoglobin," *Proceedings of the National Academy of Sciences,* vol. 22, no. 4, pp. 210-216, 1936.

[4] D. Malonek and A. Grinvald, "Interactions between electrical activity and cortical microcirculation revealed by imaging spectroscopy: implications for functional brain mapping," *Science,* vol. 272, no. 5261, pp. 551-554, 1996.

[5] M. E. Raichle, R. L. Grubb, M. H. Gado, J. O. Eichling, and M. M. Ter-Pogossian, "Correlation between regional cerebral blood flow and oxidative metabolism: in vivo studies in man," *Archives of neurology,* vol. 33, no. 8, pp. 523-526, 1976.

[6] L. Sokoloff, M. Reivich, C. Kennedy, M. D. Rosiers, C. Patlak, K. Pettigrew, et al., O. Sakurada, and M. Shinohara, "The [14C] deoxyglucose method for the measurement of local cerebral glucose utilization: theory, procedure, and normal values in the conscious and anesthetized albino rat 1," *Journal of neurochemistry,* vol. 28, no. 5, pp. 897-916, 1977.

[7] P. T. Fox, M. E. Raichle, M. A. Mintun, and C. Dence, "Nonoxidative glucose consumption during focal physiologic neural activity," *Science,* vol. 241, no. 4864, pp. 462-464, 1988.

[8] R. Grech, T. Cassar, J. Muscat, K. P. Camilleri, S. G. Fabri, M. Zervakis, P. Xanthopoulos, V. Sakkalis, and B. Vanrumste, "Review on solving the inverse

problem in EEG source analysis," *Journal of neuroengineering and rehabilitation,* vol. 5, no. 1, p. 25, 2008.

[9] A. Ekstrom, "How and when the fMRI BOLD signal relates to underlying neural activity: the danger in dissociation," *Brain research reviews,* vol. 62, no. 2, pp. 233-244, 2010.

[10] T. Murta, U. J. Chaudhary, T. M. Tierney, A. Dias, M. Leite, D. W. Carmichael, P. Figueiredo, and L. Lemieux, "Phase–amplitude coupling and the BOLD signal: a simultaneous intracranial EEG (icEEG)-fMRI study in humans performing a finger-tapping task," *NeuroImage,* vol. 146, pp. 438-451, 2017.

[11] S.-G. Kim and S. Ogawa, "Biophysical and physiological origins of blood oxygenation level-dependent fMRI signals," *Journal of Cerebral Blood Flow & Metabolism,* vol. 32, no. 7, pp. 1188-1206, 2012.

[12] B. Cauli and E. Hamel, "Revisiting the role of neurons in neurovascular coupling," *Frontiers in neuroenergetics,* vol. 2, p. 9, 2010.

[13] M. Rosa, J. Daunizeau, and K. J. Friston, "EEG-fMRI integration: a critical review of biophysical modeling and data analysis approaches," *Journal of integrative neuroscience,* vol. 9, no. 04, pp. 453-476, 2010.

[14] C. Bledowski, D. Prvulovic, R. Goebel, F. E. Zanella, and D. E. Linden, "Attentional systems in target and distractor processing: a combined ERP and fMRI study," *Neuroimage,* vol. 22, no. 2, pp. 530-540, 2004.

[15] S. Crottaz-Herbette and V. Menon, "Where and when the anterior cingulate cortex modulates attentional response: combined fMRI and ERP evidence," *Journal of cognitive neuroscience,* vol. 18, no. 5, pp. 766-780, 2006.

[16] M. Sabri, E. Liebenthal, E. Waldron, D. A. Medler, and J. R. Binder, "Attentional modulation in the detection of irrelevant deviance: a simultaneous ERP/fMRI study," *Journal of Cognitive Neuroscience,* vol. 18, no. 5, pp. 689-700, 2006.

[17] M. Hoppstädter, C. Baeuchl, C. Diener, H. Flor, and P. Meyer, "Simultaneous EEG–fMRI reveals brain networks underlying recognition memory ERP old/new effects," *NeuroImage,* vol. 116, pp. 112-122, 2015.

[18] B. Sadeh, I. Podlipsky, A. Zhdanov, and G. Yovel, "Event‐related potential and functional MRI measures of face‐selectivity are highly correlated: a simultaneous ERP‐fMRI investigation," *Human brain mapping,* vol. 31, no. 10, pp. 1490-1501, 2010.

[19] C. G. Bénar, D. Schön, S. Grimault, B. Nazarian, B. Burle, M. Roth, J. M. Badier, P. Marquis, C. Liegeois‐Chauvel, and J. L. Anton, "Single‐trial analysis of oddball event‐related potentials in simultaneous EEG‐fMRI," *Human brain mapping,* vol. 28, no. 7, pp. 602-613, 2007.

[20] S. I. Gonçalves, J. C. De Munck, P. Pouwels, R. Schoonhoven, J. Kuijer, N. Maurits, J. Hoogduin, E. Van Someren, R. Heethaar, and F. L. Da Silva, "Correlating the alpha rhythm to BOLD using simultaneous EEG/fMRI: inter-subject variability," *Neuroimage,* vol. 30, no. 1, pp. 203-213, 2006.

[21] H. Laufs, A. Kleinschmidt, A. Beyerle, E. Eger, A. Salek-Haddadi, C. Preibisch, and K. Krakow, "EEG-correlated fMRI of human alpha activity," *Neuroimage,* vol. 19, no. 4, pp. 1463-1476, 2003.

[22] H. Yuan, R. Phillips, C. K. Wong, V. Zotev, M. Misaki, B. Wurfel, F. Krueger, M. Feldner, and J. Bodurka, "Tracking resting state connectivity dynamics in veterans with PTSD," *NeuroImage: Clinical,* vol. 19, pp. 260-270, 2018.

[23] H. Yuan, V. Zotev, R. Phillips, W. C. Drevets, and J. Bodurka, "Spatiotemporal dynamics of the brain at rest—exploring EEG microstates as electrophysiological signatures of BOLD resting state networks," *Neuroimage,* vol. 60, no. 4, pp. 2062-2072, 2012.

[24] J. Britz, D. Van De Ville, and C. M. Michel, "BOLD correlates of EEG topography reveal rapid resting-state network dynamics," *Neuroimage,* vol. 52, no. 4, pp. 1162-1170, 2010.

[25] D. Van de Ville, J. Britz, and C. M. Michel, "EEG microstate sequences in healthy humans at rest reveal scale-free dynamics," *Proceedings of the National Academy of Sciences,* vol. 107, no. 42, pp. 18179-18184, 2010.

[26] M. M. Monti, "Statistical analysis of fMRI time-series: a critical review of the GLM approach," *Frontiers in human neuroscience,* vol. 5, p. 28, 2011.

[27] T. Larsen and J. P. O'Doherty, "Uncovering the spatio-temporal dynamics of value-based decision-making in the human brain: a combined fMRI–EEG study,"

Philosophical Transactions of the Royal Society B: Biological Sciences, vol. 369, no. 1655, p. 20130473, 2014.

[28] W. Ou, A. Nummenmaa, J. Ahveninen, J. W. Belliveau, M. S. Hämäläinen, and P. Golland, "Multimodal functional imaging using fMRI-informed regional EEG/MEG source estimation," *Neuroimage,* vol. 52, no. 1, pp. 97-108, 2010.

[29] R. L. Silton, W. Heller, D. N. Towers, A. S. Engels, J. M. Spielberg, J. C. Edgar, S. M. Sass, J. L. Stewart, B. P. Sutton, and M. T. Banich, "The time course of activity in dorsolateral prefrontal cortex and anterior cingulate cortex during top-down attentional control," *Neuroimage,* vol. 50, no. 3, pp. 1292-1302, 2010.

[30] T. Deneux and O. Faugeras, "EEG-fMRI fusion of paradigm-free activity using Kalman filtering," *Neural computation,* vol. 22, no. 4, pp. 906-948, 2010.

[31] X. Lei, D. Ostwald, J. Hu, C. Qiu, C. Porcaro, A. P. Bagshaw, and D. Yao, "Multimodal functional network connectivity: an EEG-fMRI fusion in network space," *PloS one,* vol. 6, no. 9, p. e24642, 2011.

[32] M. Luessi, S. D. Babacan, R. Molina, J. R. Booth, and A. K. Katsaggelos, "Bayesian symmetrical EEG/fMRI fusion with spatially adaptive priors," *Neuroimage,* vol. 55, no. 1, pp. 113-132, 2011.

[33] P. A. Valdes‐Sosa, J. M. Sanchez‐Bornot, R. C. Sotero, Y. Iturria‐Medina, Y. Aleman‐Gomez, J. Bosch‐Bayard, F. Carbonell, and T. Ozaki, "Model driven EEG/fMRI fusion of brain oscillations," *Human brain mapping,* vol. 30, no. 9, pp. 2701-2721, 2009.

[34] V. D. Calhoun, J. Liu, and T. Adalı, "A review of group ICA for fMRI data and ICA for joint inference of imaging, genetic, and ERP data," *Neuroimage,* vol. 45, no. 1, pp. S163-S172, 2009.

[35] K. J. Friston, "Functional and effective connectivity: a review," *Brain connectivity,* vol. 1, no. 1, pp. 13-36, 2011.

[36] A. T. Drysdale, L. Grosenick, J. Downar, K. Dunlop, F. Mansouri, Y. Meng, R. N. Fetcho, B. Zebley, D. J. Oathes, and A. Etkin, "Resting-state connectivity biomarkers define neurophysiological subtypes of depression," *Nature medicine,* vol. 23, no. 1, p. 28, 2017.

[37] H. Cui, J. Zhang, Y. Liu, Q. Li, H. Li, L. Zhang, Q. Hu, W. Cheng, Q. Luo, and J. Li, "Differential alterations of resting‐state functional connectivity in generalized anxiety disorder and panic disorder," *Human brain mapping,* vol. 37, no. 4, pp. 1459-1473, 2016.

[38] D.-E. Meskaldji, M. G. Preti, T. A. Bolton, M.-L. Montandon, C. Rodriguez, S. Morgenthaler, P. Giannakopoulos, S. Haller, and D. Van De Ville, "Prediction of long-term memory scores in MCI based on resting-state fMRI," *NeuroImage: Clinical,* vol. 12, pp. 785-795, 2016.

[39] D. S. Bassett, B. G. Nelson, B. A. Mueller, J. Camchong, and K. O. Lim, "Altered resting state complexity in schizophrenia," *Neuroimage,* vol. 59, no. 3, pp. 2196-2207, 2012.

[40] J. S. Anderson, J. A. Nielsen, A. L. Froehlich, M. B. DuBray, T. J. Druzgal, A. N. Cariello, J. R. Cooperrider, B. A. Zielinski, C. Ravichandran, and P. T. Fletcher, "Functional connectivity magnetic resonance imaging classification of autism," *Brain,* vol. 134, no. 12, pp. 3742-3754, 2011.

[41] C. A. Lima, A. L. Coelho, and S. Chagas, "Automatic EEG signal classification for epilepsy diagnosis with Relevance Vector Machines," *Expert Systems with Applications,* vol. 36, no. 6, pp. 10054-10059, 2009.

[42] A. F. Leuchter, I. A. Cook, W. S. Gilmer, L. B. Marangell, K. S. Burgoyne, R. H. Howland, M. H. Trivedi, S. Zisook, R. Jain, and M. Fava, "Effectiveness of a quantitative electroencephalographic biomarker for predicting differential response or remission with escitalopram and bupropion in major depressive disorder," *Psychiatry research,* vol. 169, no. 2, pp. 132-138, 2009.

[43] A. E. Whitton, S. Deccy, M. L. Ironside, P. Kumar, M. Beltzer, and D. A. Pizzagalli, "Electroencephalography source functional connectivity reveals abnormal high-frequency communication among large-scale functional networks in depression," *Biological Psychiatry: Cognitive Neuroscience and Neuroimaging,* vol. 3, no. 1, pp. 50-58, 2018.

[44] O. Al Zoubi, A. Mayeli, A. Tsuchiyagaito, M. Misaki, V. Zotev, H. Refai, M. P. Paulus, and J. Bodurka, "EEG Microstates Temporal Dynamics Differentiate Individuals with Mood and Anxiety Disorders from Healthy Subjects," *Frontiers in human neuroscience,* vol. 13, p. 56, 2019.

[45] M. J. Gandal, J. C. Edgar, K. Klook, and S. J. Siegel, "Gamma synchrony: towards a translational biomarker for the treatment-resistant symptoms of schizophrenia," *Neuropharmacology,* vol. 62, no. 3, pp. 1504-1518, 2012.

[46] H. Hampel, R. Frank, K. Broich, S. J. Teipel, R. G. Katz, J. Hardy, K. Herholz, A. L. Bokde, F. Jessen, and Y. C. Hoessler, "Biomarkers for Alzheimer's disease: academic, industry and regulatory perspectives," *Nature reviews Drug discovery,* vol. 9, no. 7, p. 560, 2010.

[47] V. Zotev, H. Yuan, M. Misaki, R. Phillips, K. D. Young, M. T. Feldner, and J. Bodurka, "Correlation between amygdala BOLD activity and frontal EEG asymmetry during real-time fMRI neurofeedback training in patients with depression," *NeuroImage: Clinical,* vol. 11, pp. 224-238, 2016.

[48] A. Omidvarnia, M. A. Kowalczyk, M. Pedersen, and G. D. Jackson, "Towards fast and reliable simultaneous EEG-fMRI analysis of epilepsy with automatic spike detection," *Clinical Neurophysiology,* vol. 130, no. 3, pp. 368-378, 2019.

[49] T. A. Victor, S. S. Khalsa, W. K. Simmons, J. S. Feinstein, J. Savitz, R. L. Aupperle, H.-W. Yeh, J. Bodurka, and M. P. Paulus, "Tulsa 1000: a naturalistic study protocol for multilevel assessment and outcome prediction in a large psychiatric sample," *BMJ open,* vol. 8, no. 1, p. e016620, 2018.

[50] O. Al Zoubi, C. Ki Wong, R. T. Kuplicki, H.-w. Yeh, A. Mayeli, H. Refai, M. Paulus, and J. Bodurka, "Predicting age from brain EEG signals–a machine learning approach," *Frontiers in aging neuroscience,* vol. 10, p. 184, 2018.

[51] J. J. Allen and S. J. Reznik, "Frontal EEG asymmetry as a promising marker of depression vulnerability: Summary and methodological considerations," *Current opinion in psychology,* vol. 4, pp. 93-97, 2015.

[52] E. Niedermeyer and F. L. da Silva, *Electroencephalography: basic principles, clinical applications, and related fields*. Lippincott Williams & Wilkins, 2005.

[53] A. Horvath, A. Szucs, G. Csukly, A. Sakovics, G. Stefanics, and A. Kamondi, "EEG and ERP biomarkers of Alzheimer's disease: a critical review," *Front Biosci (Landmark Ed),* vol. 23, pp. 183-220, 2018.

[54] A. Khanna, A. Pascual-Leone, C. M. Michel, and F. Farzan, "Microstates in resting-state EEG: current status and future directions," *Neuroscience & Biobehavioral Reviews,* vol. 49, pp. 105-113, 2015.

[55] D. Lehmann, H. Ozaki, and I. Pal, "EEG alpha map series: brain micro-states by space-oriented adaptive segmentation," *Electroencephalography and clinical neurophysiology,* vol. 67, no. 3, pp. 271-288, 1987.

[56] C. M. Michel and T. Koenig, "EEG microstates as a tool for studying the temporal dynamics of whole-brain neuronal networks: a review," *Neuroimage,* vol. 180, pp. 577-593, 2018.

[57] H. G. Vaughan Jr, "The neural origins of human event‐related potentials," *Annals of the New York Academy of Sciences,* vol. 338, no. 1, pp. 125-138, 1980.

[58] F. Musso, J. Brinkmeyer, A. Mobascher, T. Warbrick, and G. Winterer, "Spontaneous brain activity and EEG microstates. A novel EEG/fMRI analysis approach to explore resting-state networks," *Neuroimage,* vol. 52, no. 4, pp. 1149-1161, 2010.

[59] D. Brandeis and D. Lehmann, "Segments of event-related potential map series reveal landscape changes with visual attention and subjective contours," *Electroencephalography and clinical neurophysiology,* vol. 73, no. 6, pp. 507-519, 1989.

[60] D. Brandeis, D. Lehmann, C. M. Michel, and W. Mingrone, "Mapping event-related brain potential microstates to sentence endings," *Brain topography,* vol. 8, no. 2, pp. 145-159, 1995.

[61] T. Koenig and D. Lehmann, "Microstates in language-related brain potential maps show noun-verb differences," *Brain and Language,* vol. 53, no. 2, pp. 169-182, 1996.

[62] D. Pizzagalli, D. Lehmann, T. König, M. Regard, and R. D. Pascual-Marqui, "Face-elicited ERPs and affective attitude: brain electric microstate and tomography analyses," *Clinical Neurophysiology,* vol. 111, no. 3, pp. 521-531, 2000.

[63] C. M. Michel, G. Thut, S. Morand, A. Khateb, A. J. Pegna, R. G. de Peralta, S. Gonzalez, M. Seeck, and T. Landis, "Electric source imaging of human brain functions," *Brain Research Reviews,* vol. 36, no. 2-3, pp. 108-118, 2001.

[64] J. Britz, L. Díaz Hernàndez, T. Ro, and C. M. Michel, "EEG-microstate dependent emergence of perceptual awareness," *Frontiers in behavioral neuroscience,* vol. 8, p. 163, 2014.

[65] J. Britz and C. M. Michel, "Errors can be related to pre-stimulus differences in ERP topography and their concomitant sources," *Neuroimage,* vol. 49, no. 3, pp. 2774-2782, 2010.

[66] A. Custo, D. Van De Ville, W. M. Wells, M. I. Tomescu, D. Brunet, and C. M. Michel, "Electroencephalographic Resting-State Networks: Source Localization of Microstates," *Brain connectivity,* vol. 7, no. 10, pp. 671-682, 2017.

[67] C. Andreou, P. L. Faber, G. Leicht, D. Schoettle, N. Polomac, I. L. Hanganu-Opatz, D. Lehmann, and C. Mulert, "Resting-state connectivity in the prodromal phase of schizophrenia: insights from EEG microstates," *Schizophrenia research,* vol. 152, no. 2-3, pp. 513-520, 2014.

[68] M. I. Tomescu, T. A. Rihs, R. Becker, J. Britz, A. Custo, F. Grouiller, M. Schneider, M. Debbané, S. Eliez, and C. M. Michel, "Deviant dynamics of EEG resting state pattern in 22q11. 2 deletion syndrome adolescents: A vulnerability marker of schizophrenia?," *Schizophrenia research,* vol. 157, no. 1-3, pp. 175-181, 2014.

[69] D. Lehmann, P. L. Faber, S. Galderisi, W. M. Herrmann, T. Kinoshita, M. Koukkou, A. Mucci, R. D. Pascual-Marqui, N. Saito, and J. Wackermann, "EEG microstate duration and syntax in acute, medication-naive, first-episode schizophrenia: a multi-center study," *Psychiatry Research: Neuroimaging,* vol. 138, no. 2, pp. 141-156, 2005.

[70] K. Nishida, Y. Morishima, M. Yoshimura, T. Isotani, S. Irisawa, K. Jann, T. Dierks, W. Strik, T. Kinoshita, and T. Koenig, "EEG microstates associated with salience and frontoparietal networks in frontotemporal dementia, schizophrenia and Alzheimer's disease," *Clinical Neurophysiology,* vol. 124, no. 6, pp. 1106-1114, 2013.

[71] W. Strik, T. Dierks, T. Becker, and D. Lehmann, "Larger topographical variance and decreased duration of brain electric microstates in depression," *Journal of Neural Transmission/General Section JNT,* vol. 99, no. 1-3, pp. 213-222, 1995.

[72] T. Dierks, V. Jelic, P. Julin, K. Maurer, L. Wahlund, O. Almkvist, W. Strik, and B. Winblad, "EEG-microstates in mild memory impairment and Alzheimer's disease:

possible association with disturbed information processing," *Journal of neural transmission,* vol. 104, no. 4-5, pp. 483-495, 1997.

[73] W. K. Strik, R. Chiaramonti, G. C. Muscas, M. Paganini, T. J. Mueller, A. J. Fallgatter, A. Versari, and R. Zappoli, "Decreased EEG microstate duration and anteriorisation of the brain electrical fields in mild and moderate dementia of the Alzheimer type," *Psychiatry Research: Neuroimaging,* vol. 75, no. 3, pp. 183-191, 1997.

[74] A. Stevens and T. Kircher, "Cognitive decline unlike normal aging is associated with alterations of EEG temporo-spatial characteristics," *European archives of psychiatry and clinical neuroscience,* vol. 248, no. 5, pp. 259-266, 1998.

[75] M. Kikuchi, T. Koenig, T. Munesue, A. Hanaoka, W. Strik, T. Dierks, Y. Koshino, and Y. Minabe, "EEG microstate analysis in drug-naive patients with panic disorder," *PLoS One,* vol. 6, no. 7, p. e22912, 2011.

[76] N. M. Drissi, A. Szakács, S. T. Witt, A. Wretman, M. Ulander, H. Ståhlbrandt, N. Darin, T. Hallböök, A.-M. Landtblom, and M. Engström, "Altered brain microstate dynamics in adolescents with narcolepsy," *Frontiers in human neuroscience,* vol. 10, p. 369, 2016.

[77] M. Gschwind, D. Van De Ville, M. Hardmeier, P. Fuhr, C. Michel, and M. Seeck, "ID 249–Corrupted fractal organization of EEG topographical fluctuations predict disease state in minimally disabled multiple sclerosis patients," *Clinical Neurophysiology,* vol. 127, no. 3, p. e72, 2016.

[78] A. Stevens, W. Günther, W. Lutzenberger, M. Bartels, and N. Müller, "Abnormal topography of EEG microstates in Gilles de la Tourette syndrome," *European archives of psychiatry and clinical neuroscience,* vol. 246, no. 6, pp. 310-316, 1996.

[79] M. M. Murray, D. Brunet, and C. M. Michel, "Topographic ERP analyses: a step-by-step tutorial review," *Brain topography,* vol. 20, no. 4, pp. 249-264, 2008.

[80] O. Maimon and L. Rokach, "Data mining and knowledge discovery handbook," 2005.

[81] K. J. Ressler and H. S. Mayberg, "Targeting abnormal neural circuits in mood and anxiety disorders: from the laboratory to the clinic," *Nature neuroscience,* vol. 10, no. 9, p. 1116, 2007.

[82] L. Campbell-Sills, S. L. Cohan, and M. B. Stein, "Relationship of resilience to personality, coping, and psychiatric symptoms in young adults," *Behaviour research and therapy,* vol. 44, no. 4, pp. 585-599, 2006.

[83] F. von Wegner, E. Tagliazucchi, and H. Laufs, "Information-theoretical analysis of resting state EEG microstate sequences-non-Markovianity, non-stationarity and periodicities," *Neuroimage,* vol. 158, pp. 99-111, 2017.

[84] A. Mayeli, V. Zotev, H. Refai, and J. Bodurka, "Real-Time EEG artifact correction during fMRI using ICA," *Journal of neuroscience methods,* vol. 274, pp. 27-37, 2016.

[85] P. J. Allen, O. Josephs, and R. Turner, "A method for removing imaging artifact from continuous EEG recorded during functional MRI," *Neuroimage,* vol. 12, no. 2, pp. 230-239, 2000.

[86] P. J. Allen, G. Polizzi, K. Krakow, D. R. Fish, and L. Lemieux, "Identification of EEG events in the MR scanner: the problem of pulse artifact and a method for its subtraction," *Neuroimage,* vol. 8, no. 3, pp. 229-239, 1998.

[87] A. J. Bell and T. J. Sejnowski, "An information-maximization approach to blind separation and blind deconvolution," *Neural computation,* vol. 7, no. 6, pp. 1129-1159, 1995.

[88] A. Delorme and S. Makeig, "EEGLAB: an open source toolbox for analysis of single-trial EEG dynamics including independent component analysis," *Journal of neuroscience methods,* vol. 134, no. 1, pp. 9-21, 2004.

[89] A. Khanna, A. Pascual-Leone, and F. Farzan, "Reliability of resting-state microstate features in electroencephalography," *PLoS One,* vol. 9, no. 12, p. e114163, 2014.

[90] A. Ghasemi and S. Zahediasl, "Normality tests for statistical analysis: a guide for non-statisticians," *International journal of endocrinology and metabolism,* vol. 10, no. 2, p. 486, 2012.

[91] S. Goodman, "A dirty dozen: twelve p-value misconceptions," in *Seminars in hematology*, 2008, vol. 45, no. 3, pp. 135-140: Elsevier.

[92] H. S. Mayberg, "Modulating dysfunctional limbic-cortical circuits in depression: towards development of brain-based algorithms for diagnosis and optimised treatment," *British medical bulletin,* vol. 65, no. 1, pp. 193-207, 2003.

[93] A. C. Waters and H. S. Mayberg, "Brain-Based Biomarkers for the Treatment of Depression: Evolution of an Idea," *Journal of the International Neuropsychological Society,* vol. 23, no. 9-10, pp. 870-880, 2017.

[94] W. C. Drevets and M. E. Raichle, "Neuroanatomical circuits in depression: implications for treatment mechanisms," *Psychopharmacology bulletin,* 1992.

[95] S. Vossel, J. J. Geng, and G. R. Fink, "Dorsal and ventral attention systems: distinct neural circuits but collaborative roles," *The Neuroscientist,* vol. 20, no. 2, pp. 150-159, 2014.

[96] Y. Yin, C. Jin, L. T. Eyler, H. Jin, X. Hu, L. Duan, H. Zheng, B. Feng, X. Huang, and B. Shan, "Altered regional homogeneity in post-traumatic stress disorder: a restingstate functional magnetic resonance imaging study," *Neuroscience bulletin,* vol. 28, no. 5, pp. 541-549, 2012.

[97] Q. Gong, L. Li, M. Du, W. Pettersson-Yeo, N. Crossley, X. Yang, J. Li, X. Huang, and A. Mechelli, "Quantitative prediction of individual psychopathology in trauma survivors using resting-state FMRI," *Neuropsychopharmacology,* vol. 39, no. 3, p. 681, 2014.

[98] M. Kennis, S. Van Rooij, M. Van Den Heuvel, R. Kahn, and E. Geuze, "Functional network topology associated with posttraumatic stress disorder in veterans," *NeuroImage: Clinical,* vol. 10, pp. 302-309, 2016.

[99] Y. Zhang, B. Xie, H. Chen, M. Li, F. Liu, and H. Chen, "Abnormal functional connectivity density in post-traumatic stress disorder," *Brain topography,* vol. 29, no. 3, pp. 405-411, 2016.

[100] J. M. Soares, A. Sampaio, L. M. Ferreira, N. C. Santos, P. Marques, F. Marques, J. A. Palha, J. J. Cerqueira, and N. Sousa, "Stress impact on resting state brain networks," *PLoS One,* vol. 8, no. 6, p. e66500, 2013.

[101] Y. He, T. Xu, W. Zhang, and X. N. Zuo, "Lifespan anxiety is reflected in human amygdala cortical connectivity," *Human brain mapping,* vol. 37, no. 3, pp. 1178-1193, 2016.

[102] W. Liao, H. Chen, Y. Feng, D. Mantini, C. Gentili, Z. Pan, J. Ding, X. Duan, C. Qiu, and S. Lui, "Selective aberrant functional connectivity of resting state networks in social anxiety disorder," *Neuroimage,* vol. 52, no. 4, pp. 1549-1558, 2010.

[103] L. Wang, D. Hermens, I. Hickie, and J. Lagopoulos, "A systematic review of resting-state functional-MRI studies in major depression," *Journal of affective disorders,* vol. 142, no. 1-3, pp. 6-12, 2012.

[104] B. Sundermann, M. Olde lütke Beverborg, and B. Pfleiderer, "Toward literature-based feature selection for diagnostic classification: a meta-analysis of resting-state fMRI in depression," *Frontiers in human neuroscience,* vol. 8, p. 692, 2014.

[105] R. H. Kaiser, J. R. Andrews-Hanna, T. D. Wager, and D. A. Pizzagalli, "Large-scale network dysfunction in major depressive disorder: a meta-analysis of resting-state functional connectivity," *JAMA psychiatry,* vol. 72, no. 6, pp. 603-611, 2015.

[106] F. Sambataro, E. Visintin, N. Doerig, J. Brakowski, M. G. Holtforth, E. Seifritz, and S. Spinelli, "Altered dynamics of brain connectivity in major depressive disorder at-rest and during task performance," *Psychiatry Research: Neuroimaging,* vol. 259, pp. 1-9, 2017.

[107] Y. I. Sheline, D. M. Barch, J. L. Price, M. M. Rundle, S. N. Vaishnavi, A. Z. Snyder, M. A. Mintun, S. Wang, R. S. Coalson, and M. E. Raichle, "The default mode network and self-referential processes in depression," *Proceedings of the National Academy of Sciences,* vol. 106, no. 6, pp. 1942-1947, 2009.

[108] C. Lemogne, G. le Bastard, H. Mayberg, E. Volle, L. Bergouignan, S. Lehéricy, J.-F. Allilaire, and P. Fossati, "In search of the depressive self: extended medial prefrontal network during self-referential processing in major depression," *Social cognitive and affective neuroscience,* vol. 4, no. 3, pp. 305-312, 2009.

[109] T. Harmony, E. Marosi, A. E. D. de León, J. Becker, and T. Fernández, "Effect of sex, psychosocial disadvantages and biological risk factors on EEG maturation," *Electroencephalography and clinical Neurophysiology,* vol. 75, no. 6, pp. 482-491, 1990.

[110] Z. Lao, D. Shen, Z. Xue, B. Karacali, S. M. Resnick, and C. Davatzikos, "Morphological classification of brains via high-dimensional shape transformations and machine learning methods," *Neuroimage,* vol. 21, no. 1, pp. 46-57, 2004.

[111] D. B. Lindsley, "A longitudinal study of the occipital alpha rhythm in normal children: Frequency and amplitude standards," *The Pedagogical Seminary and Journal of Genetic Psychology,* vol. 55, no. 1, pp. 197-213, 1939.

[112] A. T. Lu, E. Hannon, M. E. Levine, E. M. Crimmins, K. Lunnon, J. Mill, D. H. Geschwind, and S. Horvath, "Genetic architecture of epigenetic and neuronal ageing rates in human brain regions," *Nature communications,* vol. 8, p. 15353, 2017.

[113] K. Franke, G. Ziegler, S. Klöppel, C. Gaser, and A. s. D. N. Initiative, "Estimating the age of healthy subjects from T 1-weighted MRI scans using kernel methods: Exploring the influence of various parameters," *Neuroimage,* vol. 50, no. 3, pp. 883-892, 2010.

[114] H. R. Pardoe, J. H. Cole, K. Blackmon, T. Thesen, R. Kuzniecky, and H. E. P. Investigators, "Structural brain changes in medically refractory focal epilepsy resemble premature brain aging," *Epilepsy research,* vol. 133, pp. 28-32, 2017.

[115] S. Valizadeh, J. Hänggi, S. Mérillat, and L. Jäncke, "Age prediction on the basis of brain anatomical measures," *Human brain mapping,* vol. 38, no. 2, pp. 997-1008, 2017.

[116] E. Càmara, N. Bodammer, A. Rodríguez-Fornells, and C. Tempelmann, "Age-related water diffusion changes in human brain: a voxel-based approach," *Neuroimage,* vol. 34, no. 4, pp. 1588-1599, 2007.

[117] N. U. Dosenbach, B. Nardos, A. L. Cohen, D. A. Fair, J. D. Power, J. A. Church, S. M. Nelson, G. S. Wig, A. C. Vogel, and C. N. Lessov-Schlaggar, "Prediction of individual brain maturity using fMRI," *Science,* vol. 329, no. 5997, pp. 1358-1361, 2010.

[118] J. Qin, S.-G. Chen, D. Hu, L.-L. Zeng, Y.-M. Fan, X.-P. Chen, and H. Shen, "Predicting individual brain maturity using dynamic functional connectivity," *Frontiers in human neuroscience,* vol. 9, 2015.

[119] F. Liem, G. Varoquaux, J. Kynast, F. Beyer, S. K. Masouleh, J. M. Huntenburg, L. Lampe, M. Rahim, A. Abraham, and R. C. Craddock, "Predicting brain-age from multimodal imaging data captures cognitive impairment," *NeuroImage,* vol. 148, pp. 179-188, 2017.

[120] I. Nenadić, M. Dietzek, K. Langbein, H. Sauer, and C. Gaser, "BrainAGE score indicates accelerated brain aging in schizophrenia, but not bipolar disorder," *Psychiatry Research: Neuroimaging,* vol. 266, pp. 86-89, 2017.

[121] J. Ashburner, "A fast diffeomorphic image registration algorithm," *Neuroimage,* vol. 38, no. 1, pp. 95-113, 2007.

[122] A. R. Clarke, R. J. Barry, R. McCarthy, and M. Selikowitz, "Age and sex effects in the EEG: development of the normal child," *Clinical neurophysiology,* vol. 112, no. 5, pp. 806-814, 2001.

[123] L. Cragg, N. Kovacevic, A. R. McIntosh, C. Poulsen, K. Martinu, G. Leonard, and T. Paus, "Maturation of EEG power spectra in early adolescence: a longitudinal study," *Developmental science,* vol. 14, no. 5, pp. 935-943, 2011.

[124] P. J. Marshall, Y. Bar-Haim, and N. A. Fox, "Development of the EEG from 5 months to 4 years of age," *Clinical Neurophysiology,* vol. 113, no. 8, pp. 1199-1208, 2002.

[125] P. Matthis, D. Scheffner, C. Benninger, C. Lipinski, and L. Stolzis, "Changes in the background activity of the electroencephalogram according to age," *Electroencephalography and clinical neurophysiology,* vol. 49, no. 5, pp. 626-635, 1980.

[126] C. Benninger, P. Matthis, and D. Scheffner, "EEG development of healthy boys and girls. Results of a longitudinal study," *Electroencephalography and clinical neurophysiology,* vol. 57, no. 1, pp. 1-12, 1984.

[127] M. Kikuchi, Y. Wada, Y. Koshino, Y. Nanbu, and T. Hashimoto, "Effect of normal aging upon interhemispheric EEG coherence: analysis during rest and photic stimulation," *Clinical Electroencephalography,* vol. 31, no. 4, pp. 170-174, 2000.

[128] M. G. Marciani, M. Maschio, F. Spanedda, C. Caltagirone, G. Gigli, and G. Bernardi, "Quantitative EEG evaluation in normal elderly subjects during mental processes: age-related changes," *International Journal of Neuroscience,* vol. 76, no. 1-2, pp. 131-140, 1994.

[129] M. Widagdo, J. Pierson, and R. Helme, "Age-related changes in qEEG during cognitive tasks," *International journal of neuroscience,* vol. 95, no. 1-2, pp. 63-75, 1998.

[130] A. Hashemi, L. J. Pino, G. Moffat, K. J. Mathewson, C. Aimone, P. J. Bennett, L. A. Schmidt, and A. B. Sekuler, "Characterizing population EEG dynamics throughout adulthood," *eNeuro,* vol. 3, no. 6, pp. ENEURO. 0275-16.2016, 2016.

[131] C. Babiloni, G. Binetti, A. Cassarino, G. Dal Forno, C. Del Percio, F. Ferreri, R. Ferri, G. Frisoni, S. Galderisi, and K. Hirata, "Sources of cortical rhythms in adults during physiological aging: a multicentric EEG study," *Human brain mapping,* vol. 27, no. 2, pp. 162-172, 2006.

[132] S. I. Dimitriadis and C. I. Salis, "Mining Time-Resolved Functional Brain Graphs to an EEG-Based Chronnectomic Brain Aged Index (CBAI)," *Frontiers in human neuroscience,* vol. 11, p. 423, 2017.

[133] B. Saletu, E. Paulus, L. Linzmayer, P. Anderer, H. V. Semlitsch, J. Grünberger, L. Wicke, A. Neuhold, and I. Podreka, "Nicergoline in senile dementia of Alzheimer type and multi-infarct dementia: a double-blind, placebo-controlled, clinical and EEG/ERP mapping study," *Psychopharmacology,* vol. 117, no. 4, pp. 385-395, 1995.

[134] C. Babiloni, A. I. Triggiani, R. Lizio, S. Cordone, G. Tattoli, V. Bevilacqua, A. Soricelli, R. Ferri, F. Nobili, and L. Gesualdo, "Classification of single normal and Alzheimer's disease individuals from cortical sources of resting state EEG rhythms," *Frontiers in neuroscience,* vol. 10, p. 47, 2016.

[135] A. I. Triggiani, V. Bevilacqua, A. Brunetti, R. Lizio, G. Tattoli, F. Cassano, A. Soricelli, R. Ferri, F. Nobili, and L. Gesualdo, "Classification of healthy subjects and Alzheimer's disease patients with dementia from cortical sources of resting state EEG rhythms: A study using artificial neural networks," *Frontiers in neuroscience,* vol. 10, p. 604, 2017.

[136] J. M. Toole and G. B. Boylan, "NEURAL: quantitative features for newborn EEG using Matlab," *arXiv preprint arXiv:1704.05694,* 2017.

[137] C.-K. Wong, V. Zotev, M. Misaki, R. Phillips, Q. Luo, and J. Bodurka, "Automatic EEG-assisted retrospective motion correction for fMRI (aE-REMCOR)," *Neuroimage,* vol. 129, pp. 133-147, 2016.

[138] R. Niazy, C. Beckmann, G. Iannetti, J. Brady, and S. Smith, "Removal of FMRI environment artifacts from EEG data using optimal basis sets," *Neuroimage,* vol. 28, no. 3, pp. 720-737, 2005.

[139] C.-K. Wong, Q. Luo, V. Zotev, R. Phillips, C. Kam Wai Clifford, and J. Bodurka, "Automatic cardiac cycle determination directly from EEG-fMRI data by multi-scale peak detection method," *Accepted by J. Neurosci. Methods.,* 2018.

[140] R. Jenke, A. Peer, and M. Buss, "Feature extraction and selection for emotion recognition from EEG," *IEEE Transactions on Affective Computing,* vol. 5, no. 3, pp. 327-339, 2014.

[141] O. Al Zoubi, M. Awad, and N. K. Kasabov, "Anytime multipurpose emotion recognition from EEG data using a Liquid State Machine based framework," *Artificial intelligence in medicine,* 2018.

[142] M. Kuhn, "Caret: classification and regression training," *Astrophysics Source Code Library,* 2015.

[143] S. Varma and R. Simon, "Bias in error estimation when using cross-validation for model selection," *BMC bioinformatics,* vol. 7, no. 1, p. 91, 2006.

[144] J. Friedman, T. Hastie, and R. Tibshirani, *The elements of statistical learning*. Springer series in statistics New York, 2001.

[145] A. Gramfort, M. Luessi, E. Larson, D. A. Engemann, D. Strohmeier, C. Brodbeck, R. Goj, M. Jas, T. Brooks, and L. Parkkonen, "MEG and EEG data analysis with MNE-Python," *Frontiers in neuroscience,* vol. 7, 2013.

[146] T. Gasser, R. Verleger, P. Bächer, and L. Sroka, "Development of the EEG of school-age children and adolescents. I. Analysis of band power," *Electroencephalography and clinical neurophysiology,* vol. 69, no. 2, pp. 91-99, 1988.

[147] A. Chiang, C. Rennie, P. Robinson, S. Van Albada, and C. Kerr, "Age trends and sex differences of alpha rhythms including split alpha peaks," *Clinical Neurophysiology,* vol. 122, no. 8, pp. 1505-1517, 2011.

[148] F. Zappasodi, L. Marzetti, E. Olejarczyk, F. Tecchio, and V. Pizzella, "Age-related changes in electroencephalographic signal complexity," *PloS one,* vol. 10, no. 11, p. e0141995, 2015.

[149] J. D. Power, A. L. Cohen, S. M. Nelson, G. S. Wig, K. A. Barnes, J. A. Church, A. C. Vogel, T. O. Laumann, F. M. Miezin, and B. L. Schlaggar, "Functional

network organization of the human brain," *Neuron,* vol. 72, no. 4, pp. 665-678, 2011.

[150] G. H. Glover, T. Q. Li, and D. Ress, "Image‐based method for retrospective correction of physiological motion effects in fMRI: RETROICOR," *Magnetic Resonance in Medicine: An Official Journal of the International Society for Magnetic Resonance in Medicine,* vol. 44, no. 1, pp. 162-167, 2000.

[151] R. M. Birn, J. B. Diamond, M. A. Smith, and P. A. Bandettini, "Separating respiratory-variation-related fluctuations from neuronal-activity-related fluctuations in fMRI," *Neuroimage,* vol. 31, no. 4, pp. 1536-1548, 2006.

[152] H. J. Jo, Z. S. Saad, W. K. Simmons, L. A. Milbury, and R. W. Cox, "Mapping sources of correlation in resting state FMRI, with artifact detection and removal," *Neuroimage,* vol. 52, no. 2, pp. 571-582, 2010.

[153] J. D. Power, K. A. Barnes, A. Z. Snyder, B. L. Schlaggar, and S. E. Petersen, "Spurious but systematic correlations in functional connectivity MRI networks arise from subject motion," *Neuroimage,* vol. 59, no. 3, pp. 2142-2154, 2012.

[154] L. Wang, L. Su, H. Shen, and D. Hu, "Decoding lifespan changes of the human brain using resting-state functional connectivity MRI," *PloS one,* vol. 7, no. 8, p. e44530, 2012.

[155] T. B. Meier, A. S. Desphande, S. Vergun, V. A. Nair, J. Song, B. B. Biswal, M. E. Meyerand, R. M. Birn, and V. Prabhakaran, "Support vector machine classification and characterization of age-related reorganization of functional brain networks," *Neuroimage,* vol. 60, no. 1, pp. 601-613, 2012.

[156] Z. Yu-Feng, H. Yong, Z. Chao-Zhe, C. Qing-Jiu, S. Man-Qiu, L. Meng, T. Li-Xia, J. Tian-Zi, and W. Yu-Feng, "Altered baseline brain activity in children with ADHD revealed by resting-state functional MRI," *Brain and Development,* vol. 29, no. 2, pp. 83-91, 2007.

[157] X. Bu, X. Hu, L. Zhang, B. Li, M. Zhou, L. Lu, X. Hu, H. Li, Y. Yang, and W. Tang, "Investigating the predictive value of different resting-state functional MRI parameters in obsessive-compulsive disorder," *Translational psychiatry,* vol. 9, no. 1, p. 17, 2019.

[158] B. Liang, D. Zhang, X. Wen, P. Xu, X. Peng, X. Huang, M. Liu, and R. Huang, "Brain spontaneous fluctuations in sensorimotor regions were directly related to

eyes open and eyes closed: evidences from a machine learning approach," *Frontiers in human neuroscience,* vol. 8, p. 645, 2014.

[159] D. Long, J. Wang, M. Xuan, Q. Gu, X. Xu, D. Kong, and M. Zhang, "Automatic classification of early Parkinson's disease with multi-modal MR imaging," *PloS one,* vol. 7, no. 11, p. e47714, 2012.

[160] B. Thomas Yeo, F. M. Krienen, J. Sepulcre, M. R. Sabuncu, D. Lashkari, M. Hollinshead, J. L. Roffman, J. W. Smoller, L. Zöllei, and J. R. Polimeni, "The organization of the human cerebral cortex estimated by intrinsic functional connectivity," *Journal of neurophysiology,* vol. 106, no. 3, pp. 1125-1165, 2011.

[161] X. Shen, F. Tokoglu, X. Papademetris, and R. T. Constable, "Groupwise whole-brain parcellation from resting-state fMRI data for network node identification," *Neuroimage,* vol. 82, pp. 403-415, 2013.

[162] J. Gotman, E. Kobayashi, A. P. Bagshaw, C. G. Bénar, and F. Dubeau, "Combining EEG and fMRI: a multimodal tool for epilepsy research," *Journal of Magnetic Resonance Imaging: An Official Journal of the International Society for Magnetic Resonance in Medicine,* vol. 23, no. 6, pp. 906-920, 2006.

[163] F. Moeller, H. R. Siebner, S. Wolff, H. Muhle, O. Granert, O. Jansen, U. Stephani, and M. Siniatchkin, "Simultaneous EEG‐fMRI in drug‐naive children with newly diagnosed absence epilepsy," *Epilepsia,* vol. 49, no. 9, pp. 1510-1519, 2008.

[164] A. Salek-Haddadi, B. Diehl, K. Hamandi, M. Merschhemke, A. Liston, K. Friston, J. S. Duncan, D. R. Fish, and L. Lemieux, "Hemodynamic correlates of epileptiform discharges: an EEG-fMRI study of 63 patients with focal epilepsy," *Brain research,* vol. 1088, no. 1, pp. 148-166, 2006.

[165] C. M. Michel and T. Koenig, "EEG microstates as a tool for studying the temporal dynamics of whole-brain neuronal networks: A review," *NeuroImage,* 2017.

[166] K. J. Friston, P. Fletcher, O. Josephs, A. Holmes, M. Rugg, and R. Turner, "Event-related fMRI: characterizing differential responses," *Neuroimage,* vol. 7, no. 1, pp. 30-40, 1998.

[167] R. W. Cox, "AFNI: software for analysis and visualization of functional magnetic resonance neuroimages," *Computers and Biomedical research,* vol. 29, no. 3, pp. 162-173, 1996.

[168] A. Eklund, T. E. Nichols, and H. Knutsson, "Cluster failure: Why fMRI inferences for spatial extent have inflated false-positive rates," *Proceedings of the national academy of sciences,* vol. 113, no. 28, pp. 7900-7905, 2016.

[169] R. W. Cox, G. Chen, D. R. Glen, R. C. Reynolds, and P. A. Taylor, "FMRI clustering in AFNI: false-positive rates redux," *Brain connectivity,* vol. 7, no. 3, pp. 152-171, 2017.

[170] A. M. Winkler, G. R. Ridgway, M. A. Webster, S. M. Smith, and T. E. Nichols, "Permutation inference for the general linear model," *Neuroimage,* vol. 92, pp. 381-397, 2014.

[171] M. Cao, J.-H. Wang, Z.-J. Dai, X.-Y. Cao, L.-L. Jiang, F.-M. Fan, X.-W. Song, M.-R. Xia, N. Shu, and Q. Dong, "Topological organization of the human brain functional connectome across the lifespan," *Developmental cognitive neuroscience,* vol. 7, pp. 76-93, 2014.

[172] H. Onias, A. Viol, F. Palhano-Fontes, K. C. Andrade, M. Sturzbecher, G. Viswanathan, and D. B. de Araujo, "Brain complex network analysis by means of resting state fMRI and graph analysis: Will it be helpful in clinical epilepsy?," *Epilepsy & Behavior,* vol. 38, pp. 71-80, 2014.

[173] M. Termenon, A. Jaillard, C. Delon-Martin, and S. Achard, "Reliability of graph analysis of resting state fMRI using test-retest dataset from the Human Connectome Project," *NeuroImage,* vol. 142, pp. 172-187, 2016.

[174] M. P. van den Heuvel, S. C. de Lange, A. Zalesky, C. Seguin, B. T. Yeo, and R. Schmidt, "Proportional thresholding in resting-state fMRI functional connectivity networks and consequences for patient-control connectome studies: Issues and recommendations," *Neuroimage,* vol. 152, pp. 437-449, 2017.

[175] D. J. Watts and S. H. Strogatz, "Collective dynamics of 'small-world'networks," *nature,* vol. 393, no. 6684, p. 440, 1998.

[176] M. Mijalkov, E. Kakaei, J. B. Pereira, E. Westman, G. Volpe, and A. s. D. N. Initiative, "BRAPH: a graph theory software for the analysis of brain connectivity," *PloS one,* vol. 12, no. 8, p. e0178798, 2017.

[177] R. D. Bharath, R. Panda, V. R. Reddam, M. Bhaskar, S. Gohel, S. Bhardwaj, A. Prajapati, and P. K. Pal, "A Single Session of rTMS Enhances Small-Worldness

in Writer's Cramp: Evidence from Simultaneous EEG-fMRI Multi-Modal Brain Graph," *Frontiers in Human Neuroscience,* vol. 11, p. 443, 2017.

[178] X. Suo, D. Lei, K. Li, F. Chen, F. Li, L. Li, X. Huang, S. Lui, L. Li, and G. J. Kemp, "Disrupted brain network topology in pediatric posttraumatic stress disorder: a resting‐state fMRI study," *Human brain mapping,* vol. 36, no. 9, pp. 3677-3686, 2015.

[179] X.-N. Zuo, R. Ehmke, M. Mennes, D. Imperati, F. X. Castellanos, O. Sporns, and M. P. Milham, "Network centrality in the human functional connectome," *Cerebral cortex,* vol. 22, no. 8, pp. 1862-1875, 2011.

[180] J. Wang, X. Zuo, and Y. He, "Graph-based network analysis of resting-state functional MRI," *Frontiers in systems neuroscience,* vol. 4, p. 16, 2010.

[181] V. Latora and M. Marchiori, "Efficient behavior of small-world networks," *Physical review letters,* vol. 87, no. 19, p. 198701, 2001.

[182] G. Csardi and T. Nepusz, "The igraph software package for complex network research," *InterJournal, Complex Systems,* vol. 1695, no. 5, pp. 1-9, 2006.

[183] S. Epskamp, A. O. Cramer, L. J. Waldorp, V. D. Schmittmann, and D. Borsboom, "qgraph: Network visualizations of relationships in psychometric data," *Journal of Statistical Software,* vol. 48, no. 4, pp. 1-18, 2012.

[184] H. Pashler and E. J. Wagenmakers, "Editors' introduction to the special section on replicability in psychological science: A crisis of confidence?," *Perspectives on Psychological Science,* vol. 7, no. 6, pp. 528-530, 2012.

[185] K. Kroenke, R. L. Spitzer, and J. B. Williams, "The PHQ‐9: validity of a brief depression severity measure," *Journal of general internal medicine,* vol. 16, no. 9, pp. 606-613, 2001.

[186] W. Treynor, R. Gonzalez, and S. Nolen-Hoeksema, "Rumination reconsidered: A psychometric analysis," *Cognitive therapy and research,* vol. 27, no. 3, pp. 247-259, 2003.

[187] C. D. Spielberger, "Manual for the State-Trait Anxiety Inventory STAI (form Y)(" self-evaluation questionnaire")," 1983.

[188] D. Cella, W. Riley, A. Stone, N. Rothrock, B. Reeve, S. Yount, D. Amtmann, R. Bode, D. Buysse, and S. Choi, "The Patient-Reported Outcomes Measurement Information System (PROMIS) developed and tested its first wave of adult self-reported health outcome item banks: 2005–2008," *Journal of clinical epidemiology,* vol. 63, no. 11, pp. 1179-1194, 2010.

[189] P. A. Pilkonis, S. W. Choi, S. P. Reise, A. M. Stover, W. T. Riley, D. Cella, and P. C. Group, "Item banks for measuring emotional distress from the Patient-Reported Outcomes Measurement Information System (PROMIS®): depression, anxiety, and anger," *Assessment,* vol. 18, no. 3, pp. 263-283, 2011.

[190] D. A. DeWalt, N. Rothrock, S. Yount, and A. A. Stone, "Evaluation of item candidates: the PROMIS qualitative item review," *Medical care,* vol. 45, no. 5 Suppl 1, p. S12, 2007.

[191] D. Bates, M. Maechler, B. Bolker, and S. Walker, "lme4: Linear mixed-effects models using Eigen and S4," *R package version,* vol. 1, no. 7, pp. 1-23, 2014.